UNIVERSITA' DI PADOVA

SCUOLA DI DOTTORATO DI RICERCA IN INGEGNERIA INDUSTRIALE

INDIRIZZO IN INGEGNERIA ELETTROTECNICA

CICLO: XXV

STUDY OF INNOVATIVE ELECTRIC MACHINES FOR HIGH EFFICIENCY VEHICULAR TRACTION APPLICATIONS

DIRETTORE DELLA SCUOLA:
Prof. Paolo Colombo

COORDINATORE DI INDIRIZZO:
Prof. Giovanni Martinelli

SUPERVISORE:
Prof. Roberto Menis

DOTTORANDO:
Mario Mezzarobba

31 gennaio 2013

Sede Amministrativa: Università degli Studi di Padova

Sede Consorziata: Università degli Studi di Trieste

Dipartimento di Ingegneria Industriale

_____

SCUOLA DI DOTTORATO DI RICERCA IN : Ingegneria Industriale

INDIRIZZO: Ingegneria Elettrotecnica

CICLO XXV

STUDY OF

INNOVATIVE ELECTRIC MACHINES FOR HIGH EFFICIENCY

VEHICULAR TRACTION APPLICATIONS

Direttore della Scuola: Ch.mo Prof. Paolo Colombo

Coordinatore d'indirizzo: Ch.mo Prof.Giovanni Martinelli

Supervisore: Ch.mo Prof. Roberto Menis

Co-Tutor: Ch.mo Prof. Alberto Tessarolo

Dottorando : Mario Mezzarobba

Contents

Introduzione

Questa tesi contiene alcuni dei temi riguardanti le macchine elettriche per trazione veicolare che si sono affrontati durante i tre anni di dottorato di ricerca. Il lavoro è suddiviso in due parti. La prima parte si concentra su aspetti tecnologici e riguarda alcuni studi ed attività sperimentali che vanno a risolvere alcune problematiche comuni delle macchine elettriche per trazione, in particolare il deflussaggio e le pulsazioni di coppia. La seconda parte, invece risulta essere più teorica e si concentra su alcuni metodi matematici di modellizzazione ed analisi sviluppati per facilitare la progettazione e lo studio delle macchine elettriche che si è portato avanti durante il periodo di dottorato.

I capitoli della prima parte sono così suddivisi:

1. Sviluppo e sperimentazione di un motore a magneti permanenti prototipale; interamente concepito, progettato e realizzato presso l'Università degli Studi di Trieste; in cui un nuovo metodo di deflussagio per alte velocità e stato implementato. inoltre tale tecnologia è stata assoggettata a brevetto.

2. Ottimizzazione multi obiettivo di un motore sincrono a magneti permanenti a riluttanza assistita per applicazioni nell'industria automobilistica. L'ottimizzazione aveva lo scopo di supportare un progetto industrale portato avanti da un nostro partner ed ancora in atto, di conseguenza nessun prototipo è ancora stato realizzato.

3. Studio e ottimizzazione di una bietta magnetica per motori con statore a cave aperte, in grado di ridurre la pulsazione di coppia.

La seconda parte propone dei metodi di analisi numerica delle macchine elettriche sviluppati per modellizzare ed analizzare diversi tipi di macchine a magneti permanenti. La principale criticità alla quale questi capitoli tentano di dare soluzione è quello di trovare dei metodi di analisi delle macchine a magneti permanenti accurati, senza dover ricorrere a simulazioni transitorie agli elementi finiti, che come è noto sono molto dispendiose in termini di tempo.

Introduction

This thesis collects some of the work accomplished during the PhD research activity focused on the study of special electric machines for vehicle traction applications. The work is divided into due parts. The first part is mainly technological and covers some studies and experimental activities concerning new technical solutions to solve some common issues in operation of electric motors for automotive use, namely flux weakening and cogging torque. The second part has a more theoretical nature and focuses on some methods for electric machine modeling and analysis which has been developed to facilitate the study and design optimizations carried out during the PhD research work.

The chapters in the first part address the following topics:

1. Development and testing of an interior-permanent-magnet motor prototype fully conceived, designed and manufactured at the University of Trieste to implement a new concept of flux weakening system at high speeds. The concept has been also protected through a pending patent.

2. Multi-objective design optimization of an interior permanent magnet reluctance-assisted synchronous motor for the automotive industry. The design optimization was meant to support an industrial development project which is still in progress so no prototype has been built yet.

3. Study of a new optimized magnetic wedge design capable of reducing cogging torque in automotive propulsion motors having open stator slots.

The second part proposes some analytical and numerical results that have been worked out to approach the modeling and optimization of various kinds of permanent magnet synchronous motors. The main problem to which these chapters try to answer is to find sufficiently fast but accurate methods for permanent magnet analysis without time-consuming finite-element transient analysis. The proposed methods have been successfully integrated into design optimization programs used in the industrial environment in the

development of innovative electric machines not only for the automotive industry.

Part I

Chapter 1

A Survey of Mechanical and Electromagnetic Design Techniques for Permanent-Magnet Motor Flux-Weakening Enhancement

1.1 Introduction

Permanent-magnet motors, both in radial-flux and axial-flux configurations [1], are particularly suitable for being used in vehicular traction applications thanks to their high efficiency, high torque density and absence of excitation field windings [2]. A well-known disadvantage of permanent-magnet motors is the difficulty of flux weakening operation. This issue is particularly important in automotive applications where propulsion motors are generally required to operate over a wide speed range with large constant-power regions [3]. Flux weakening at high speeds is traditionally accomplished by injecting d-axis demagnetizing currents through the inverter, so that the armature reaction field tends to cancel the permanent-magnet flux [3]. This strategy can be critical for different reasons. Firstly, it often requires to oversize the inverter with respect to the capability needed to develop the rated torque at the rated speed [4]. Secondly, it leads to poor efficiency values at high speed due to large copper losses. Thirdly, it may lead to possible rotor demagnetization issues [3]. To mitigate the above mentioned problems, various approaches have been proposed in the literature to enhance permanent-magnet motor flux weakening performance by acting on

their mechanical and/or electromagnetic design. In this chapter, a survey is proposed of the most significant approaches found in the technical literature and in international patent databases. The survey is critical in the sense that the various strategies proposed are not only described but also commented on with respect to their supposed points of strength and weakness. In 1.2 an overall classification is proposed of the flux-weakening techniques for permanent-magnet motors. In the following Sections the different approaches are reviewed.

1.2 Classification

A possible classification of flux-weakening methods is proposed in fig.1.1. First of all, it distinguishes the purely-electric methods based on current injection by means of the inverter [4], [5], [6] or separate sources [7] and the methods which rely on motor mechanical and/or electromagnetic design. It should be observed that the two solutions are not mutually exclusive but often complementary. In particular, design modifications to the motor are meant to make it suitable for flux-weakening operation with smaller demagnetization currents from the inverter. The injection of a demagnetization current can be performed by the same inverter which provides the torque current, i.e. from stator phases [3], [4], [5], [6] or, more rarely, by means of a separated power source [7].
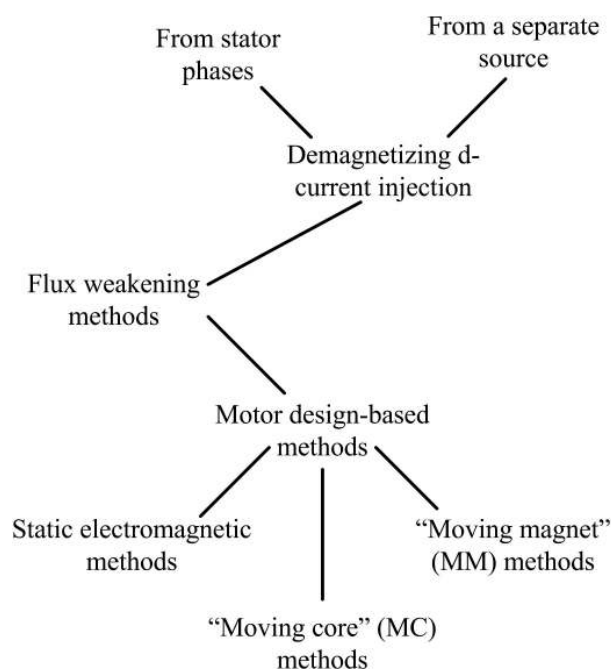
Figure 1.1: Proposed classification of flux-weakening methods.

The methods relying on motor design can in turn be divided into three main categories. The first category includes the approaches where the electromagnetic structure of the motor is modified with respect to the standard design but does not change during motor operation. For this reason such approaches are referred to as "static". The other two categories cover the cases when some motor part moves to perform or facilitate the flux weakening. The moving parts can be either the permanent magnet themselves, or some rotor core portions. The subdivision could be made even finer by distinguishing the origin of the movement, which can be produced either mechanically by appropriate transmission gears or simply by centrifugal force. The flux-weakening methods employing current injection [3]-[7] will not be reviewed hereinafter, while the attention will be focused on the techniques acting on the electromagnetic or mechanical motor design.

1.3   Static electromagnetic design methods

These methods are based on using particular motor topologies and/or materials which make the machine suitable for flux weakening, so that its flux can be reduced at high speed by a lower demagnetization current injection than would be required in case of standard construction. Examples in this sense involve the use of magnetic wedges to increase phase inductance [8], [9], [10]. The same effect is achieved by other authors by means of a fractional-slot stator winding design [11].

Some particular interior permanent magnet rotor topologies, such as those sketched in fig.1.2 and fig.1.3, have been proposed and claimed to be suitable for flux weakening [12], [13]. In particular, regarding the topology shown in fig.1.3, authors prove by finite element analysis that, when the machine is subjected to an even small demagnetization current fed from stator phases, rotor flux paths change with respect to their normal routing. Such a change is due to the modification of the local magnetic saturation state of the rotor core. The electromagnetic design of the motor is such that a d-axis current injection forces flux lines away from the air-gap, so as to reduce stator phase flux linkage, which is equivalent to achieving the desired flux weakening result. It is to be noticed that in all the design techniques mentioned above the motor geometry does not change during motor operation (this is why such methods have been indicated as "static"). At most, what may change is the routing of permanent magnet flux lines, as in case of the motor topology shown in fig.1.3.

1.4   "Moving core" methods

Under this category we have grouped the design techniques meant to weaken motor flux at high speeds by moving some parts of the rotor core. These

Figure 1.2: A)Rotor core; B)Non-magnetic annulus; C)Shaft; D)Permanent-magnet.
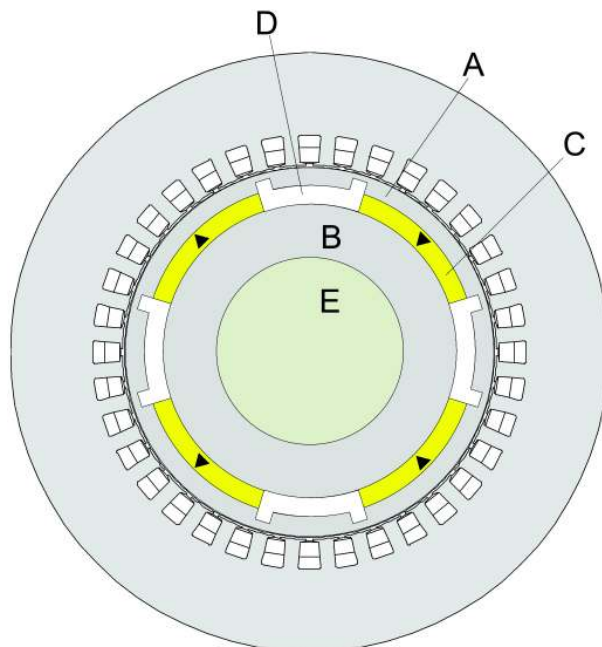
Figure 1.3: A,B)Rotor core; C)Permanent-magnet; D)Flux barrier; E)Shaft

methods therefore differ from those discussed in Section7.3 because the geometry of the motor changes during machine operation to achieve the flux weakening. The movement involves not the permanent magnets but some rotor core components. The purpose of the movement is to create a variation in the reluctance of permanent-magnet flux paths. The reluctance variation is such as to induce more flu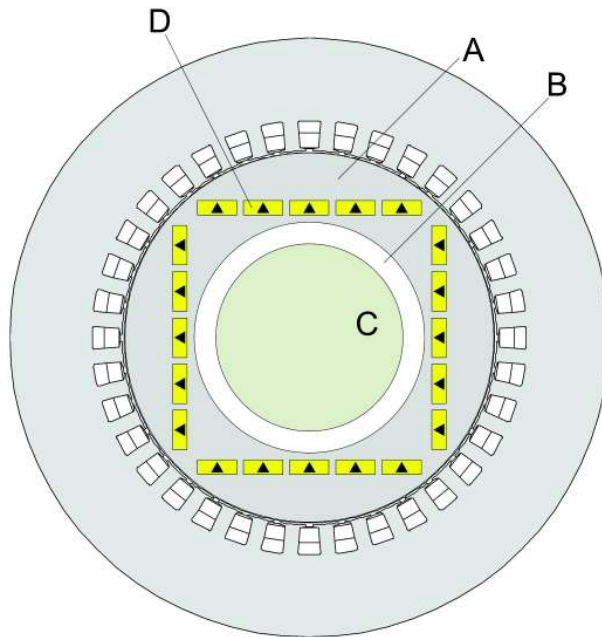x lines to circulate inside the rotor (around permanent magnets or between a permanent magnet and the adjacent ones) instead of crossing the air-gap. This obviously leads to a reduced phase flux linkage and to an overall motor flux weakening effect as a consequence. An example of the design with movable core parts is illustrated in fig.1.4 [14]. The movable core portions are the blue blocks marked by letter **B** in fig.1.4a, which are embedded in the flux barriers of a usual interior-permanent-magnet reluctance-assisted motor structure. Blocks **B** are normally kept in place by an elastic device (like a spring) placed inside each flux barrier. They are subject to the centrifugal force (red arrows in fig.1.4a) which grows with the square of the rotor speed. Above a certain rotor speed, the centrifugal force tends to push the movable blocks in the radial direction towards rotor periphery. The final configuration which the rotor assumes at high speed is represented in fig.1.4b: it can be seen that, when in their peripheral position, the movable blocks create relatively low reluctance paths (dashed close lines in fig.1.4b) through which part of permanent magnet flux can circulate without passing the air-gap, with a consequent flux weakening effect.

Another solution with movable rotor core portions is illustrated in fig.1.5 [15]. A normal interior-permanent-magnet rotor is equipped with two ferromagnetic end plates capable of axial movement (fig.1.5a). In normal conditions, the plates are detached from rotor ends. When the speed increases, the centrifugal force F is transformed into an axial thrust T acting on the plates by means of suitable transmission gears. Thrust T pushes the plates towards the rotor until the contact is reached (fig.1.5b). In this condition, the ferromagnetic plates create a low-reluctance path through which permanent-magnet flux can circulate without crossing the air-gap. One more solution for mechanical flux-weakening which involves the displacement of ferromagnetic parts is shown in fig.1.6 in its basic principle [16]. It employs an interior permanent magnet rotor with tangentially magnetized magnets ("*spoke*" topology). A ferromagnetic cylindrically-shaped part A is mechanically connected to the rotor by a spring (or set of springs). At low speeds, the moving part is retained detached from the inner rim of the rotor due to the spring force (fig.1.6a). As the centrifugal force grows, it causes the spring to extend and the moving part to displace radially until it adheres to the inner rotor rim (fig.1.6b). In this condition, part of the permanent magnet flux lines is deviated from the air-gap and flows through the moving part, thus achieving the desired flux weakening effect. Some mechanical details on a possible implementation of the mentioned system through a centrifugal
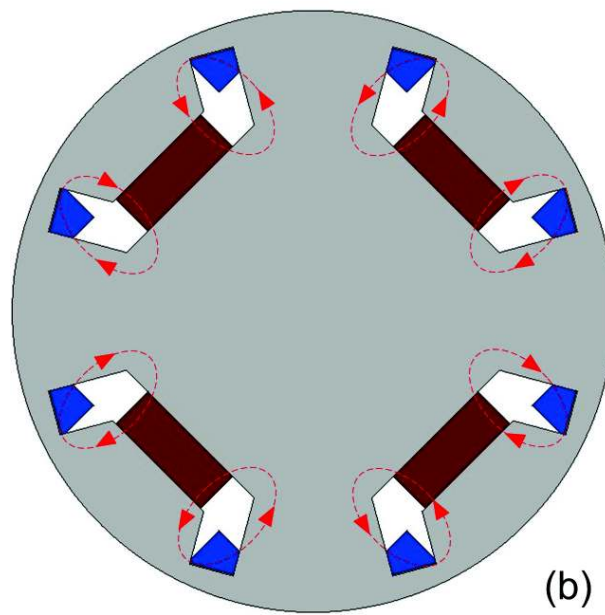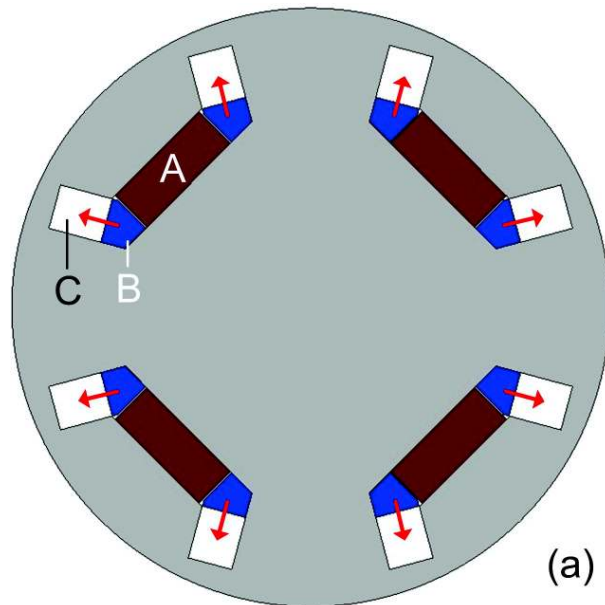
Figure 1.4: A)Permanent magnet; B)Moving part; C)Flux barrier.
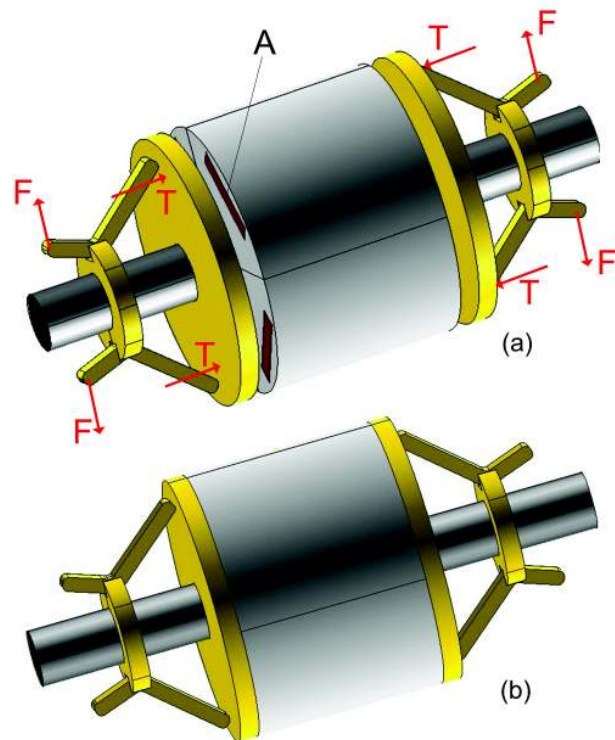
Figure 1.5: A)Permanent magnet; B)Moving part; C)Flux barrier.
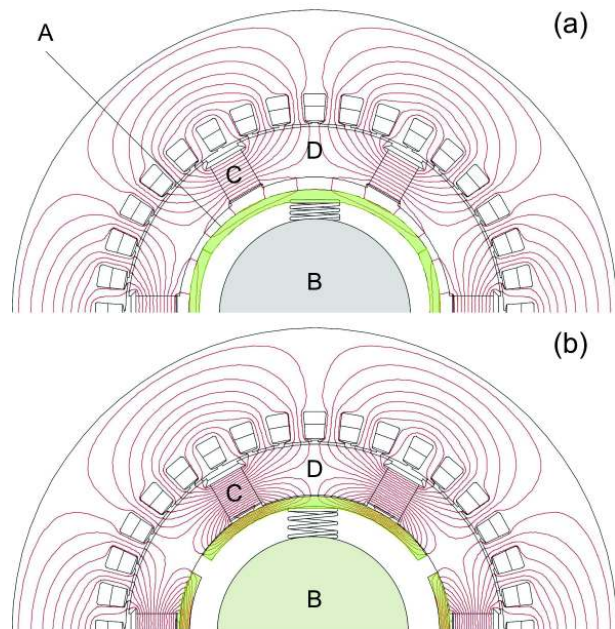
Figure 1.6: A)Ferromagnetic moving part; B)shaft; C)Permanent-magnet; D)Laminated rotor pole.

clutch are provided in [16]. A prototype is currently under realization to experimentally assess the effectiveness of the method. The approaches illustrated in fig.1.5 and fig.1.6 are relatively similar in the sense that they both exploit the centrifugal force to drive a ferromagnetic device towards rotor active parts so as to provide an alternative low-reluctance path for permanent magnet flux to circulate. However, the system shown in fig.1.5 requires the centrifugal force to be transformed into an axial thrust, which may imply some cumbersome transmission gears which are likely to increase machine length. The moving device in the system of fig.1.6, instead, is simpler and can be accommodated directly between the shaft and the rotor core. This does not imply a significant rotor size increase with respect the standard "*spoke*" design. In fact, in the space occupied by the flux weakening device (fig.1.6) a non-magnetic annulus should be placed in the standard topology to avoid magnetic short-circuit between permanent magnets. Furthermore, in the system shown in fig.1.5, the low-reluctance path created by the moving plates when in contact with the rotor (fig.1.5b) requires permanent magnet flux to partly flow axially through the rotor, which is not normal in presence of a laminated rotor core. In the magnetic short-circuited produced by the system shown in fig.1.6b, instead, all flux lines continue flowing in a plane orthogonal to the machine axis as usual.

1.5   "Moving magnets" methods

By "*moving magnet methods*" we address all those techniques in which the flux weakening is achieved by mechanical displacement of permanent magnets. An example is illustrated in fig.1.7 [17]. A surface-mounted permanent-magnet rotor is divided into two halves, mounted on a threaded shaft. One rotor half retains its original position, while the other one can rotate with respect to the shaft while axially displacing in the same way as a screw nut (fig.1.7b). Thus a rotor magnet skewing effect is achieved, which, as well known, reduces the total phase flux linkage. The reduction is also due to the fact that part of the axially-displaced rotor half protrudes out of the stator core. One more technique is shown in fig.1.8 [18], where permanent magnets are circularly-shaped and capable of rotating around their center. Each rotor pole encompasses two or more circular magnets (two in the example shown in fig.1.8), which rotate in opposite directions like engaging toothed wheels. For instance, magnets **A** and **B** in fig.1.8a form one rotor pole, while magnets **C** and **D** constitute the adjacent one. In normal conditions, all the magnets are oriented radially (fig.1.8a) so as to produce the maximum air-gap flux. At high speeds, the flux weakening is obtained by rotation of permanent magnets as illustrated in fig.1.8b. All the permanent magnets are rotated by the same angle, although in different directions, so that the fluxes produced by adjacent poles partly cancel each other out.

This obviously causes the resultant air-gap flux to reduce.
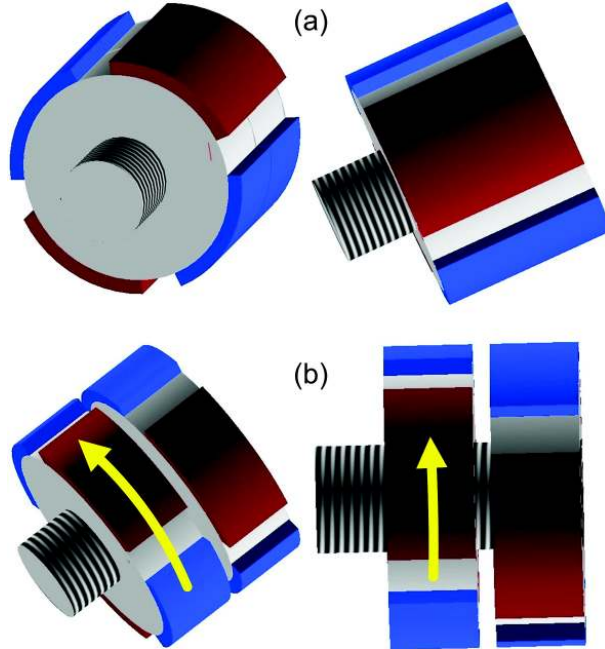
Figure 1.7: a) Rotor at low speed; b) Rotor at high speed.

Of course, both solutions shown in fig.1.7 and fig.1.8 require a non-trivial mechanical system to achieve the desired displacements. The complexity and size of such mechanical gears may constitute a problem for the practical implementation of the two solutions, also due to possible reliability or maintenance issues.

Finally, a mention is to be certainly made to the flux weakening method shown in fig.1.9 [19]. It features a "spoke" permanent-magnet rotor structure with tangential magnetization. It differs from the standard design because permanent magnets have lower height than the slots where they are embedded. In fact, during normal operation the permanent magnet is retained in the bottom part of the slot by a spring (fig.1.9a). At high speeds, the centrifugal force pushes the permanent magnets radially towards the rotor periphery so that the spring compresses and the magnets take a final position like that shown in fig.1.9b. In their new position (fig.1.9b), permanent magnets produce a lower flux than in their original position (fig.1.9a) thanks to a lower-reluctance core region surrounding the top of each rotor slot (fig.1.9). Thus an effective flux weakening is obtained at high speeds. A certain similarity can be observed between the solutions shown in fig.1.6 and fig.1.9 as they both employ a suitably-modified "spoke" permanent magnet rotor arrangement. A point of strength of the latter design is its simplicity. In fact, the further equipment required in addition to the standard design
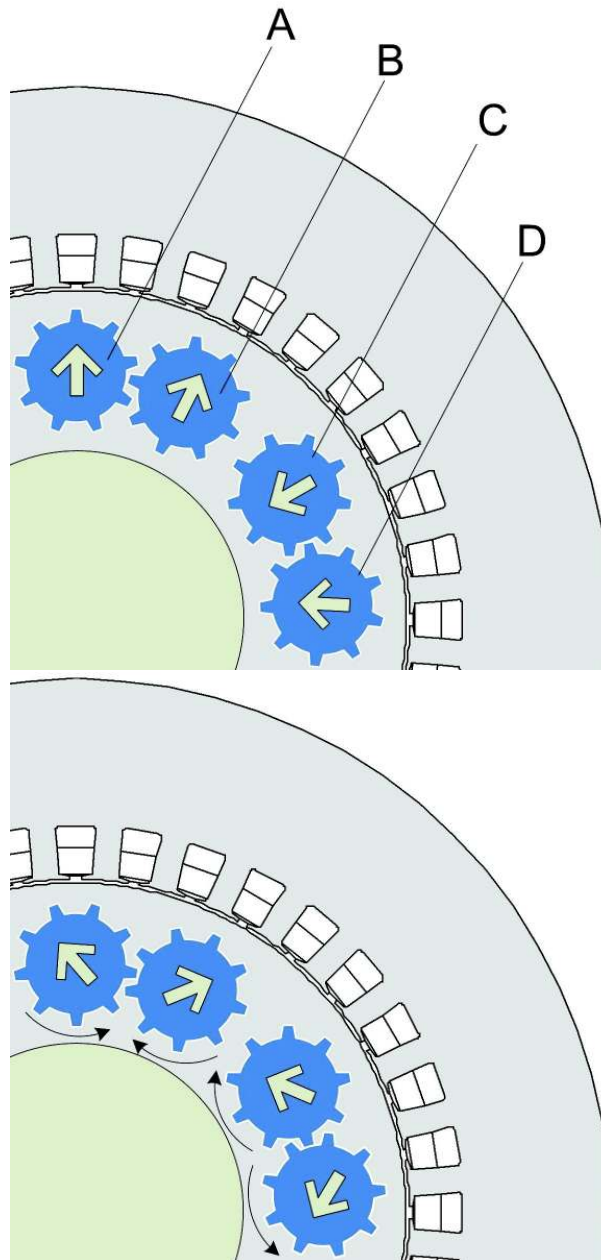
Figure 1.8: a) Configuration with full flux; b) configuration with weakened flux. A, B) Permanent magnets of one pole. C, D) Permanent magnets of adjacent pole.
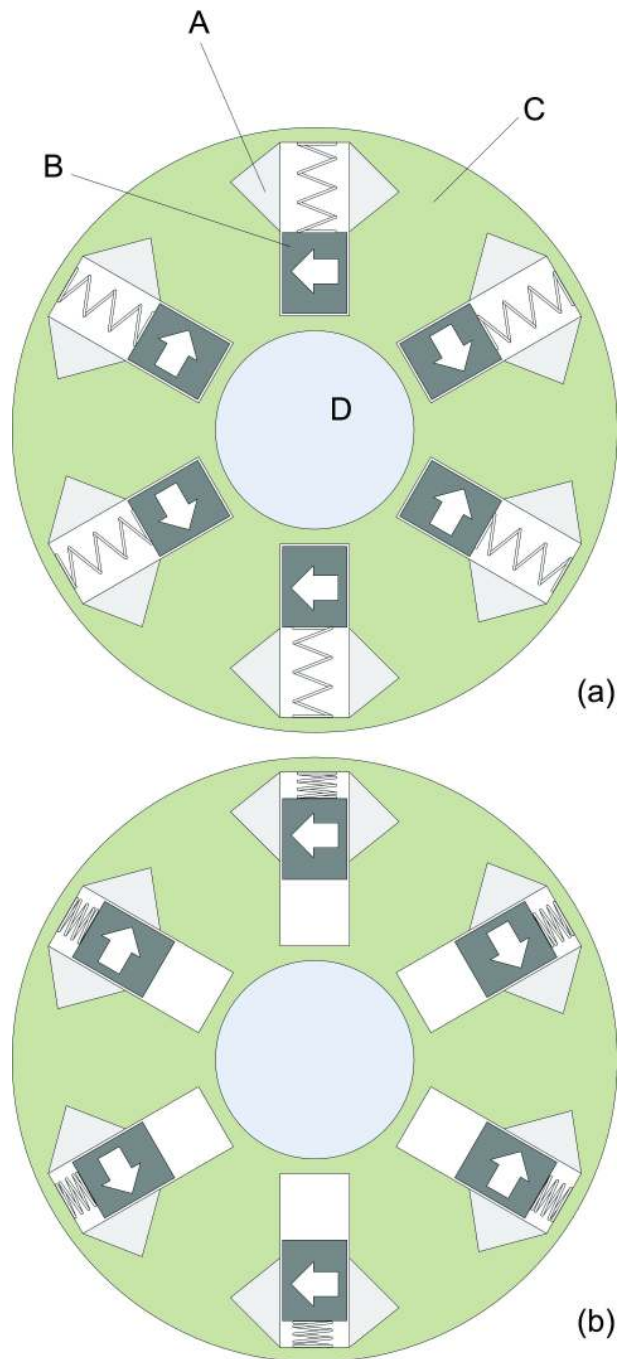
Figure 1.9: a) Low-speed configuration (full flux); b) high-speed configuration (reduced flux). A)Higher-reluctance core region. B)Permanent magnet. C)Laminated rotor core. D)Shaft.

is confined to the springs embedded in rotor slots. On the other side, the solution shown in fig.1.9 suffers from the drawback that only part of the rotor slot can be effectively employed to generate the useful flux when the machine operates at rated speed. On the contrary, rotor slots can be fully occupied by permanent magnets in the solution described in fig.1.6, with beneficial effects on the motor torque density.

1.6 Conclusions

In this chapter, a survey has been proposed of the main methods found in the technical literature and patent databases for permanent-magnet motor flux weakening through mechanical and electromagnetic design modifications. Probably, the most effective results can be obtained with those solutions where the flux weakening results from the displacement of some rotor parts (either permanent magnets or core portions). These solutions exhibit different degrees of complexity in terms of the mechanical apparatus required to produce or control the displacement. Mechanical design features may actually constitute the most challenging issues for the mentioned strategies to spread in industrial and vehicular traction applications. It is however believed that it will be worth putting further effort in their development and improvement for the significant benefits they could bring especially in the automotive industry once consolidated as mature technologies. Major advantages would be due to the lower inverter current required by the motor for high speed operation, which would in turn imply: higher efficiency at high speed for copper loss reduction; reduced inverter size; extension of motor speed range.

1.7 References

[1] G. F. Profumo, Z. Zhang, A. Tenconi, *"Axial flux machine drives: a new viable solution for electric cars"*, IEEE Trans. on Industrial Electronics, vol. 44, no. 1, Feb. 1997, pp. 39-45.

[2] K.T. Chau, C.C. Chan, *"Emerging Energy-Efficient Technologies for Hybrid Electric Vehicles"*, Proceedings of the IEEE, vol. 95, no. 4, pp.821-835, April 2007.

[3] W. L. Soong, T. J. E. Miller, *"Field-weakening performance of brushless synchronous AC motor drives"*, IEE Proceedings, Electric Power Applications, vol. 141, issue 6, Nov. 1994, pp. 331-340.

[4] F. Luise, A. Odorico, A. Tessarolo, *"Extending the speed-range of surface permanent-magnet axial-flux motors by flux-weakening characteristic*

modification", International Conference on Electric Machines, ICEM 2010, 6-9 Sept. 2010, Rome, Italy, CD-ROM paper RF-008893.

[5] Cheol Jo, Ji-Yun Seol, In-Joong Ha, *"Flux-Weakening Control of IPM Motors With Significant Effect of Magnetic Saturation and Stator Resistance"*, IEEE Transactions on Industrial Electronics, vol. 55, no. 3, pp. 1330-1340, 2008.

[6] Jiunn-Jiang Chen, Kan-Ping Chin, *"Minimum copper loss flux-weakening control of surface mounted permanent magnet synchronous motors"*, IEEE Transactions on Power Electronics, vol.18, no.4, pp. 929- 936, July 2003.

[7] M. Aydin, S. Huang, T. A. Lipo, *"A new axial flux surface mounted permanent magnet machine capable of field control"*, IEEE Industry Application Annual Meeting 2002, vol. 2, Oct. 2002, pp. 13-18.

[8] A. Di Napoli, O. Honorati, E. Santini, L. Solero, *"The use of soft magnetic materials for improving flux weakening capabilities of axial flux PM machines"*, IEEE Industry Applications Society Annual Meeting 2000, Oct. 2000, vol. 1, pp. 8-12.

[9] A. Tessarolo, F. Luise, M. Mezzarobba, M. Bortolozzi, *"A new magnetic wedge design for enhancing the performance of open-slot electric machines"*, ESARS 2012.

[10] A. Tessarolo, F. Luise, M. Mezzarobba, M. Bortolozzi, L. Branz, *"Special Magnetic Wedge Design Optimization with Genetic Algorithms for Cogging Torque Reduction in Permanent-Magnet Synchronous Machines"*, ESARS 2012. A. M. E. Refaie, T. M. Jahns, P. J. McCleer, J. W. McKeever, *"Experimental verification of optimal flux weakening in surface PM machines using concentrated windings"*, IEEE Trans. on Industry AApplications, vol. 42, no. 2, Mar.Apr. 2006, pp. 443-453.

[12] B. Stumberger, A. Hamler, M. Trlep, M. Jesenik, *"Analysis of interior permanent magnet synchronous motor designed for flux weakening operation"*, IEEE Transactions on Magnetics, vol. 37, no. 5, pp. 3644-3647, Sep 2001.

[13] Xu Longya, Ye Lurong; Zhen Li; A. El-Antably, *"A new design concept of permanent magnet machine for flux weakening operation"*, IEEE Transactions on Industry Applications, vol. 31, no. 2, pp. 373-378, Mar/Apr 1995.

[14] Japanese patent JP2012050292A, *"Permanent magnet embedded—fluxh-mounted type rotor"*, Toyota Jidosha KK, March 2012.

[15] Chinese patent CN102170211A, *"Variable excitation permanent magnet synchronous motor"*, Zuhou Industry Polytechnic University, China, Aug. 2011.

[16] A. Tessarolo, M. Mezzarobba, R. Menis, *"A Novel Interior Permanent Magnet Motor Design with a Self-Activated Flux-Weakening Device for Automotive Applications"*, paper accepted for presentation at International Conference on Electric Machines, ICEM 2012, Marseille, France, 2-5 Sept. 2012.

[17] Patent 20100213779, *"Permanent magnet motor or actuator with field weakening capability"*, inventors: K. Hochhalter, M. Seiler, August 2010.

[18] Japanese patent JP2011015476A, *"Rotary electric machine with variable permanent magnet direction"*, Ishikawa M, Jan. 2011.

[19] Baoquan Kou, Chunyan Li, Shukang Cheng, *"Flux-Weakening-Characteristic Analysis of a New Permanent-Magnet Synchronous Motor Used for Electric Vehicles"*, Plasma Science, IEEE Transactions on , vol.39, no.1, pp.511-515, Jan. 2011.

Chapter 2

A Novel Interior Permanent Magnet Motor Design with a Self-Activated Flux-Weakening Device for Automotive Applications

2.1 Introduction

Electric motors for hybrid and electric vehicle traction are usually required to operate over a wide speed range. Their top speed may be several times the base speed at which the rated torque is to be delivered [1], [2]. As a consequence, in order not to exceed inverter output voltage capabilities, the motor flux is to be weakened as the speed increases above a given threshold, [1]. For permanent-magnet (PM) motors, the flux weakening is usually achieved by injecting a demagnetizing stator current along the d axis [2]. This operation can be critical for two main reasons: on one side it exposes permanent magnets to demagnetization risks due to the stator-injected d-axis current; on the other side, it leads to raise the current capability requirement for inverter sizing.

In the literature, various PM motor designs have been proposed to improve flux weakening capabilities. Some approaches rely on the appropriate or optimal dimensioning of motor active parts [3], [4] and on the employment of such particular design features as: rotor axial laminations [5], properly-shaped flux barriers [3], fractional-slot stator windings [6], special rotor topologies capable of deviating permanent magnet flux lines towards higher-reluctance paths when a stator d axis current is applied [7], [8]. Other design approaches involve the use of an auxiliary current source to control the d

axis flux of the machine depending on the speed [9], [10]. Finally, there are ideas for achieving a PM machine flux regulation not by means of external currents but by changing the very electromagnetic structure of the machine when it enters a high speed region [11], [13].

In this chapter, a design solution is proposed that applies to Interior Permanent Magnet (IPM) machines with tangential magnetization [13]. The solution consists of equipping the usual machine topology with a self-activating mechanical device that establishes a partial magnetic short circuit on permanent magnets, so that the rotor flux crossing the air-gap noticeable decreases. The device is designed to activate automatically due to centrifugal force effects when the speed exceeds a given threshold that can be determined in the design stage.

This chapter describes the structural and functional details of the proposed IPM motor arrangement. The design guidelines followed for its conception and detailed dimensioning are outlined. Numerical performance predictions, based on finite element analysis (FEA) and lumped-parameter simulations, are presented.

The theory presented in this chapter forms the basis for the design of a technological demonstrator which is presently under construction and that will be shortly available for experimental assessment of the proposed flux-weakening solution.

2.2 Description of proposed IPM motor topology

2.2.1 Usual IPM motors with tangential magnetization

The IPM machine with tangentially magnetized permanent magnets is known to be a promising topology in electric drives for electric or hybrid vehicle traction [13]. With respect to Surface Permanent Magnet (SPM) machines it offers the advantage of higher inductance values, which implies smaller demagnetization currents for flux weakening operation [6]. Compared to other IPM structures characterized by radial magnetization, it features a very simple and cheap construction from a manufacturing viewpoint [2].

It is then reasonable to take an IPM motor structure with tangential magnetization as the basis for the technological enhancement described in this chapter, intended to further extend the motor flux weakening capability and speed range.

2.2.2 New IPM motor concept design

The IPM motor arrangement proposed in the chapter features a conventional stator equipped with a normal three-phase dual-layer short-pitch winding. The rotor is the same as in the usual IPM topology with tangential magnetization fig.2.1a except for a modified ferromagnetic back-iron yoke. In

fact, in usual IPM rotors with tangential magnetization, permanent magnets have a non-magnetic back-iron support, so that their flux is forced to cross the air-gap fig.2.1a instead of uselessly flowing through the rotor yoke fig.2.1b.

In the proposed arrangement fig.2.2, the non-magnetic back-iron is replaced by a set of ferromagnetic friction pads which can move in the radial direction so as to occupy the two extreme positions shown in fig.2.2a and fig.2.2b. In the case of fig.2.2a, they are in contact with the inner rotor rim and thereby establish a partial magnetic short circuit between permanent magnet ends. In the case of fig.2.2b, an air-gap exists between the friction pads and the inner rotor rim.
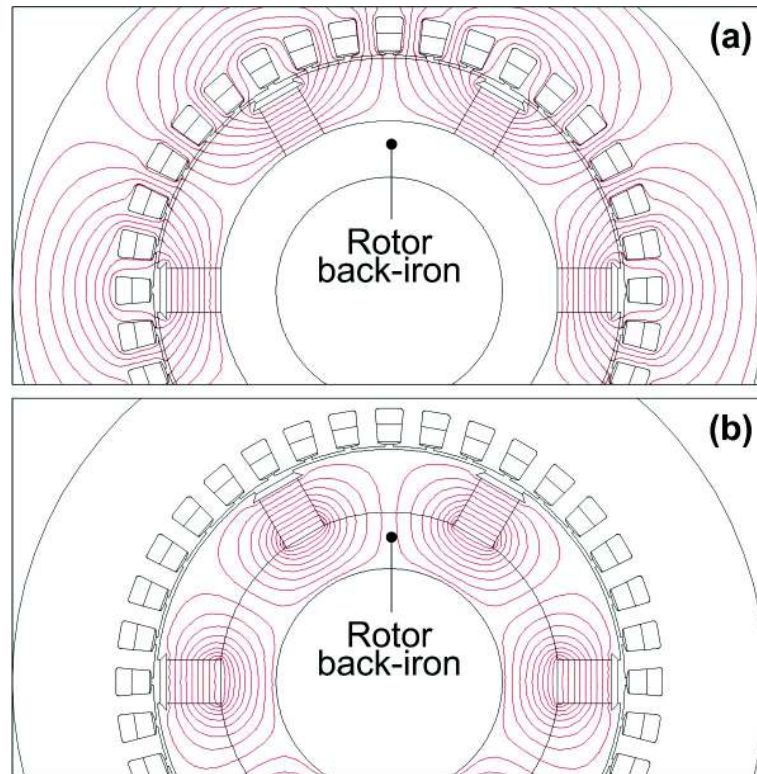
Figure 2.1: No-load flux lines in an IPM motor. (a) Case of non-magnetic unsaturated back-iron; (b) case of ferromagnetic back-iron.

The no-load flux lines which arise in the motor in the two cases are shown in fig.2.3. The figure clearly shows that, when friction pads adhere to the rotor rim, part of the flux generated by each permanent magnet crosses the air-gap while the rest flows through the pads fig.2.3a. Conversely, when the pads are detached, almost all permanent magnet flux flows into the stator

25
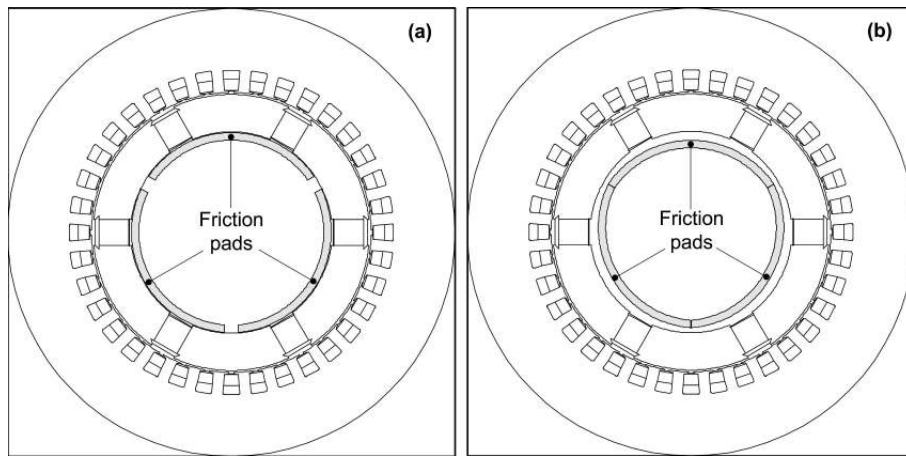
Figure 2.2: Proposed IPM structure with ferromagnetic friction pads (a) Friction pads adhere to the inner rotor rim; (b) friction pads are detached from the rotor rim.

and only very few lines pass through friction pads fig.2.3b.

The air-gap flux density in the two cases over three pole spans is diagrammed in fig.2.4. The diagram shows that the friction pad adherence to the rotor rim brings the maximum flux density from a peak value of $0.43T$ to a peak value of $0.27T$, which corresponds to a 27% decrease. Of course, the residual air-gap flux passing into the stator with adherent friction pads can be changed by design. The main design variables on which one should act for this purpose are the friction pad thickness and magnetic permeability: in fact, as the thickness and permeability increase, the magnetic saturation inside the pads decrease and a growing percentage of the total permanent magnet flux is deviated from the stator. A limit situation is shown in fig.2.1b, where almost all the permanent magnet flux flows through the back-iron due to its thickness and to the absence of magnetic saturation inside it.

2.2.3 Self-activating flux weakening device

The movement of the ferromagnetic friction pads causing motor air-gap flux weakening is activated by means of a centrifugal clutch fig.2.5 directly mounted on the motor shaft. The operation principle of a centrifugal clutch is illustrated in fig.2.6. The device is composed of a shaft-mounted hub on which two or more movable clutch shoes (two in the case of fig.2.6) are present. At one end, each clutch shoe is hinged on a pivot around which it can rotate, and at the other end an extension spring tends to keep it in rest position fig.2.6a. When the rotational speed grows, the centrifugal
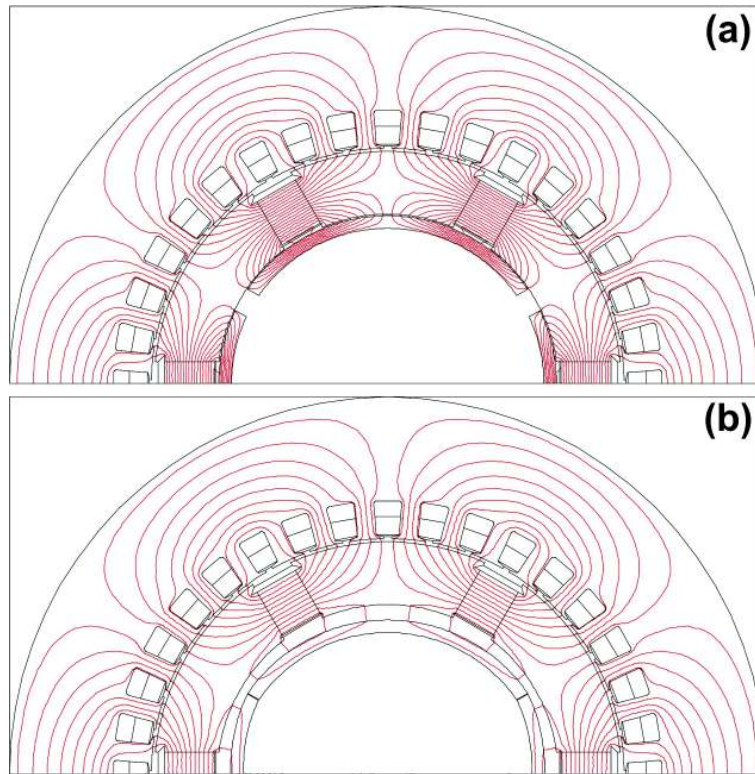
Figure 2.3: No-load flux lines with (a) attached friction pads; (b) detached friction pads.
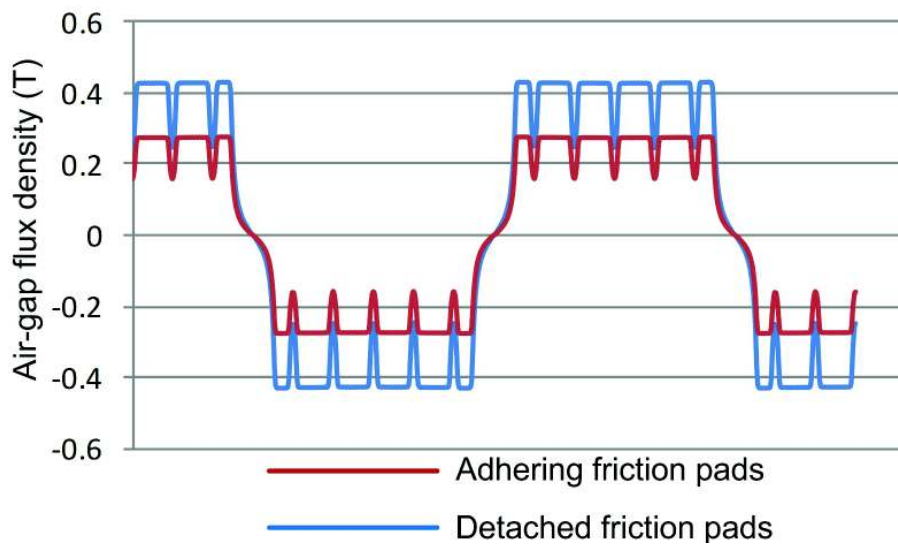
Figure 2.4: No-load air-gap flux density over three pole spans in case of adhering and detached friction pads.

force causes the clutch shoes to rotate around their hinges, which is made possible by spring extension fig.2.6b. The friction pads are soldered to the clutch shoes so that when the latter swing out, friction pads engage on the inner rotor rim and the flux weakening takes effect.Centrifugal clutches are selected as flux weakening devices as they are robust and reliable mechanical components which are already widely used and qualified in the automotive industry.

Figure 2.5: Picture of a dual-shoe centrifugal clutch used in the automotive industry.

2.2.4   Prototype features and details

In order to assess the feasibility and effectiveness of the IPM motor design presented above, a prototype is presently under constructions. The prototype main dimensions, winding data and predicted ratings are given in Tab.2.1-2.3, where reference is made to the symbols illustrated in fig.2.7. As concerns material selection, Samarium-Cobalt is chosen for permanent magnets, with a magnetic coercitivity of about $600kA/m$ and with a relative magnetic permeability of around 1.04. Rotor poles could be built from silicon-iron laminations like the stator core, but for robustness and easier manufacturability, a solid steel construction is preferred. The friction pads are made of ordinary carbon steel. From a mechanical construction viewpoint, the prototype rotor design is illustrated in fig.2.8. It should be noticed

28
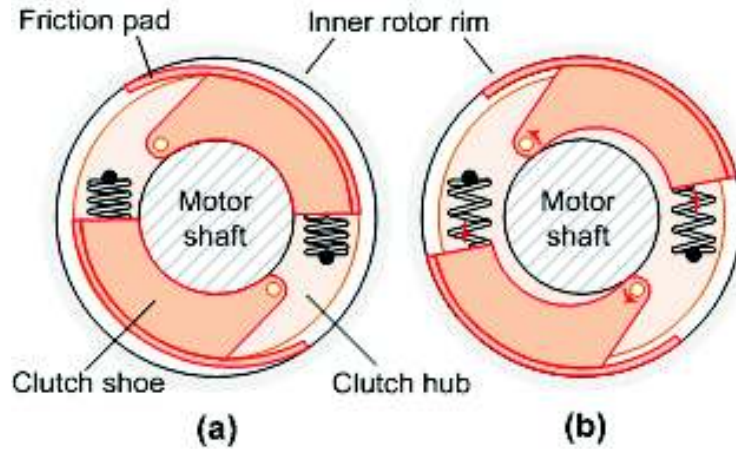
Figure 2.6: Centrifugal clutch: (a) in rest position; (b) in engaged position under centrifugal stress.

that, while in the ordinary motor design fig.2.1 rotor poles and permanent magnets can be fixed to the shaft, either directly (in case of non-magnetic shaft) or through a non-magnetic annulus, this is not possible in the proposed prototype construction because the centrifugal clutch must be located just between the shaft and rotor active parts. As a consequence, rotor poles and permanent magnets must be fixed to the shaft by means of solid-steel end plates appropriately shaped as shown in fig.2.8. Both end plates and rotor poles are provided with holes for the insertion of bolted tie rods, whose function is to give the rotor structure the needed axial compactness. Tie rods are also needed to secure rotor poles in the radial direction counteracting centrifugal stresses.

Each permanent magnets are fixed to rotor poles by means of two non-magnetic wedges: an upper (thicker) wedge dimensioned to withstand centrifugal forces and a lower (thinner) wedge used to support permanent magnets when the rotor is at stand-still or at very low speeds. The lower wedge, in particular, is necessary because each permanent magnet (although shown as a continuous block in fig.2.8) is actually composed of a sequence of axially aligned modules. An axial cross section schematic of the overall rotor assembly is finally reported in fig.2.9, where it is possible to identify the following components: **A** - motor shaft; **B** - key for torque transmission from the shaft to the rotor; **C** - end plate; **D** - bolted tie rod; **E** - rotor pole; **F** - friction pad; **G** - centrifugal clutch. It can be seen from fig.2.9 that end plates are mounted on motor shaft by interference using a key for torque transmission.

Furthermore, since friction pads are to be almost as long as the motor core in order to magnetically short-circuit permanent magnets in an effective

DIMENSIONS OF THE PROTOTYPE IPM MOTOR		
	Symbol	mm
Stator outer diameter	D_s	210
Rotor outer diameter	D_r	148
Stator slot height	h_s	12
Rotor pole height	h_p	20
Permanent magnet height	h_m	15.8
Permanent magnet width	w_m	14
Air-gap width	θ	1
Friction pad thickness	h_c	4
Minimum gap g between friction pads and rotor rim		0
Maximum gap g between friction pads and rotor rim		5
Core length	L	150

Table 2.1: Dimensions of the prototype IPM motor

WINDING DATA OF THE IPM MOTOR	
Number poles	6
Number of stator slots	36
Number of stator phases	3
Number of winding layers	2
Coil to pole pitch ratio	5/6
Number of turns per coil	21
Number of series-connected turns per phase	252

Table 2.2: Winding data of the IPM motor

PREDICTED RATINGS OF THE IPM MOTOR		
Base frequency	Hz	50
Base speed	rpm	1000
Maximum speed	rpm	2500
Base voltage	V	340
Base torque	Nm	43
Maximum phase current	A	8

Table 2.3: Predicted ratings of the IPM motor
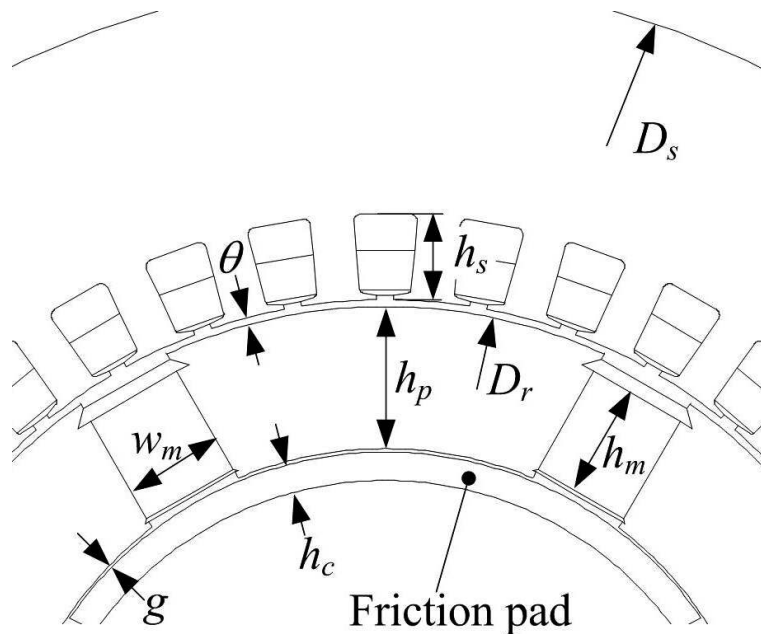
Figure 2.7: Symbols used to characterize prototype dimensions.

way and due to the limited axial length of commercially-available centrifugal clutches, the use of several clutches (three in the case of fig.2.9) is mandatory. The possibility that friction pads may not equally adhere to the inner rotor rim along the axial direction at high speeds due to imperfect assembly or slightly different thrusts exerted by the different clutches has been considered in the design stage and shown to be not critical. In fact, the presence of a small air-gap (in the order of few tenths of millimeters) between the friction pad and the inner pole rim ($g \cong 0.5 mm$ in fig.2.7) does not practically alter the magnetic short-circuit effectiveness according to FEA simulations. One last observation which can be made observing fig.2.8 and fig.2.9 regards the material to be used for end plates. If these were made of a ferromagnetic material, a local magnetic short circuit would be induced in the end portions of permanent magnets. In fact, the ferromagnetic end plate would offer a low permeance path where permanent-magnet flux could flow without crossing the air-gap. This would be detrimental in the sense that the rotor portion placed in contact with end-plates would not contribute to torque production and the overall air-gap flux of the machine would be diminished regardless of rotor speed. For this reason, stainless-steel (practically non-magnetic) end plates will be used for prototype construction.
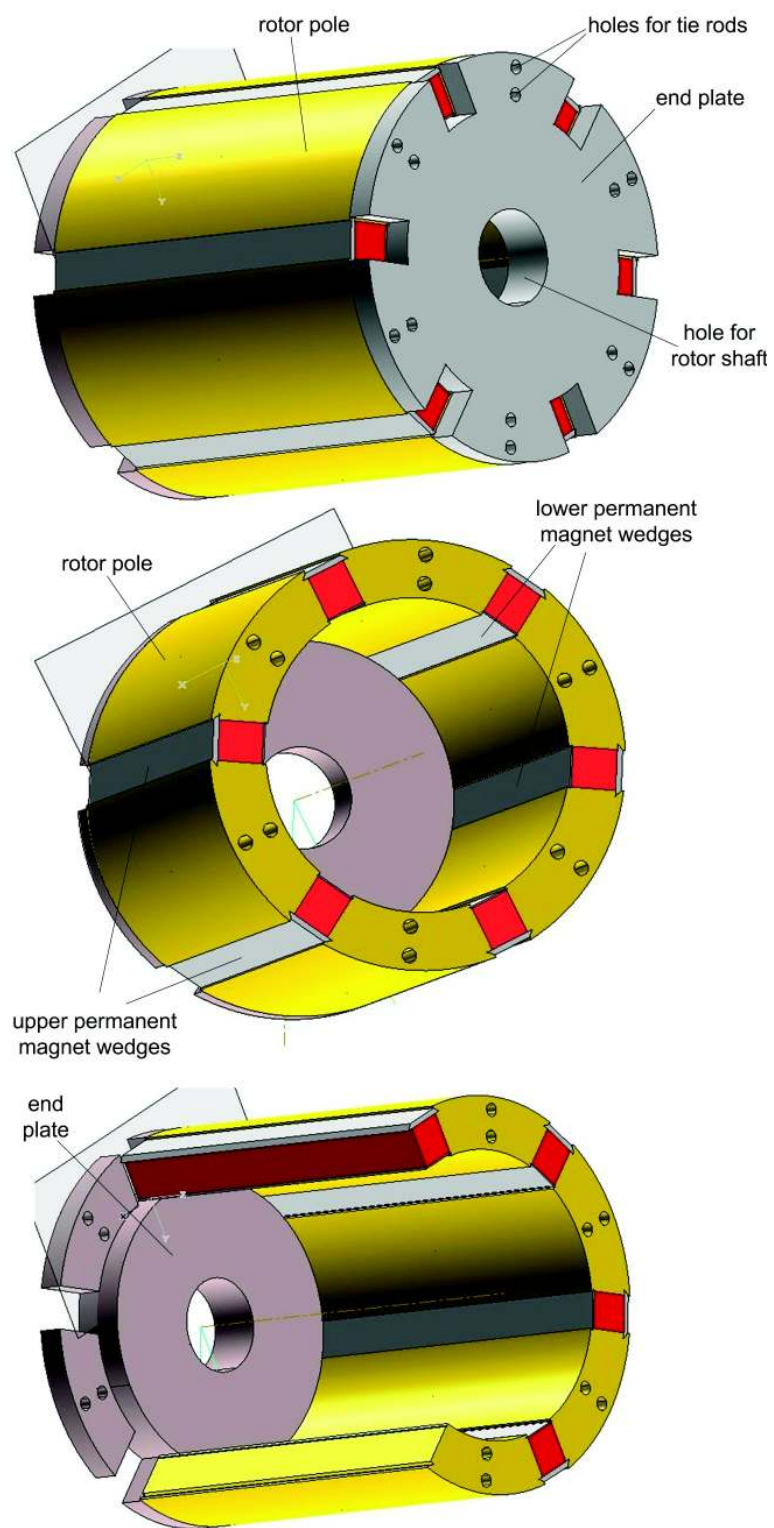
Figure 2.8: Illustrative views and cross sections of the prototype rotor.
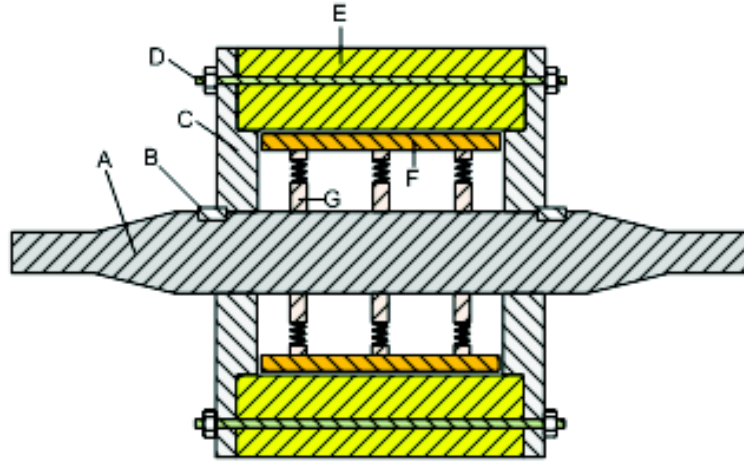
Figure 2.9: Axial cross section schematic of the proposed IPM motor.

2.3 Performance prediction by dynamic simulations

Theoretically, the flux weakening device to be integrated into the proposed IPM motor structure should be dimensioned so that the centrifugal clutch activates exactly when a given speed (identified as the base speed according to Tab.2.3) is exceeded during acceleration and returns to the rest position when the speed drops below the same value during deceleration.

Obviously, this theoretical on-off behavior could not be reasonably achieved in practice due to the amount of forces involved in the device activation / deactivation and to the intrinsically dynamic nature of its operation.

It is therefore important, in the design stage, to predict what the behavior of the real system will be with adequate accuracy. For this purpose, magneto-static FEA simulations are not sufficient because the geometry of the machine to be studied cannot be represented with a single static model as it is subject to changing over time. Also time-stepping or time-domain FEA simulations including electromagnetic analysis only would not be enough because mechanical effects produced not only by rotor motion but also by other mechanical parts moving in the radial directions should be considered. A multi-domain multi-physics approach, combining electromagnetic and structural FEA simulations should be rather used as the most accurate tool for system transient analysis [14].

However, it can be noticed that in the system under study the mechanical stresses and deformations to be taken into account are only related to centrifugal stresses and to the consequent clutch spring extension. On the other side, the electromagnetic effects to be included in the device simulation reduce to the magneto-dynamic attractive force which arises between

rotor poles and the friction pad; such a force can be easily found as a function of the distance between the two parts by a set of magneto-static FEA simulations.

Therefore, the approach which will be next followed for transient system simulation basically relies on a lumped-parameter model where the distance between rotor poles and friction pads is the only unknown time-varying quantity and where the magneto-dynamic attraction of rotor poles on friction pads is treated through a look-up table based on previously-launched magneto-static FEA simulations.
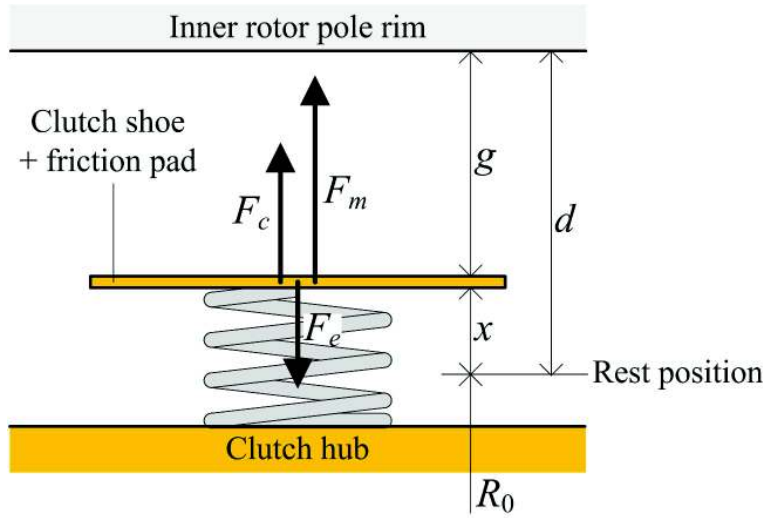
Figure 2.10: Schematic of the model used for dynamic simulations.

A schematic of the model assumed for dynamic lumped-parameter simulations is shown in fig.2.10. In the model, the clutch shoe and the friction pad soldered to it are represented as a single body (called mover in the following) of equivalent mass M, whose displacement is identified by the variable x with respect to its rest position. Such rest position is located at a distance R_0 from the shaft center. The geometric constant d indicates the distance between the mover rest position and the inner rotor rim. The mover is subject to three forces: the elastic force F_e exerted by the clutch spring; the centrifugal force F_c due to shaft revolution and the magnetic force F_m accounting for the attractive effect of the rotor pole on the ferromagnetic friction pad. The following differential equation can be thereby written which governs mover displacement x over time:

$$M\frac{d^2x}{dt^2} = F_m + F_c - F_e \qquad (2.1)$$

The centrifugal force depends on the rotor speed n (measured in revolu-

34

tions per minutes) according to the low:

$$F_c = M \left(\frac{2\pi}{60} n \right)^2 (R_0 + x) \tag{2.2}$$

Calling k the spring constant of the equivalent clutch spring, the expression for the elastic force F_e is:

$$F_e = k \cdot x + F_{e0} \tag{2.3}$$
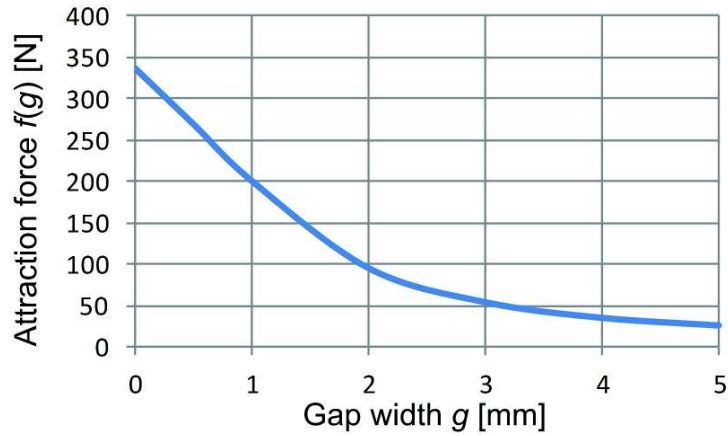
Figure 2.11: Attraction force f as a function of gap g.

PARAMETER VALUES FOR SYSTEM DYNAMIC MODEL			
Equivalent mover mass	M	0.48	kg
Radius at mover rest position	R_0	47	mm
Equivalent clutch spring constant	k	59	N/mm
Distance	d	5	mm
Spring preload	F_{e0}	309	N

Table 2.4: Parameter values for system dynamic model

where F_{e0} indicates the spring "pre-load", i.e. the elastic force exerted by the spring when the mover is in its rest position. Regarding the magnetic force F_m, it depends on the air-gap width g between the inner pole rim and the friction pad according to a function f that can be easily determined by a set of magneto-static FEA simulations fig.2.11):

$$F_m = f(g) = f(d - x) \tag{2.4}$$

Equations (2.2)-(2.4) can be substituted into (2.1), using parameter values given in Tab.2.4. The differential equation (2.1) can be then solved
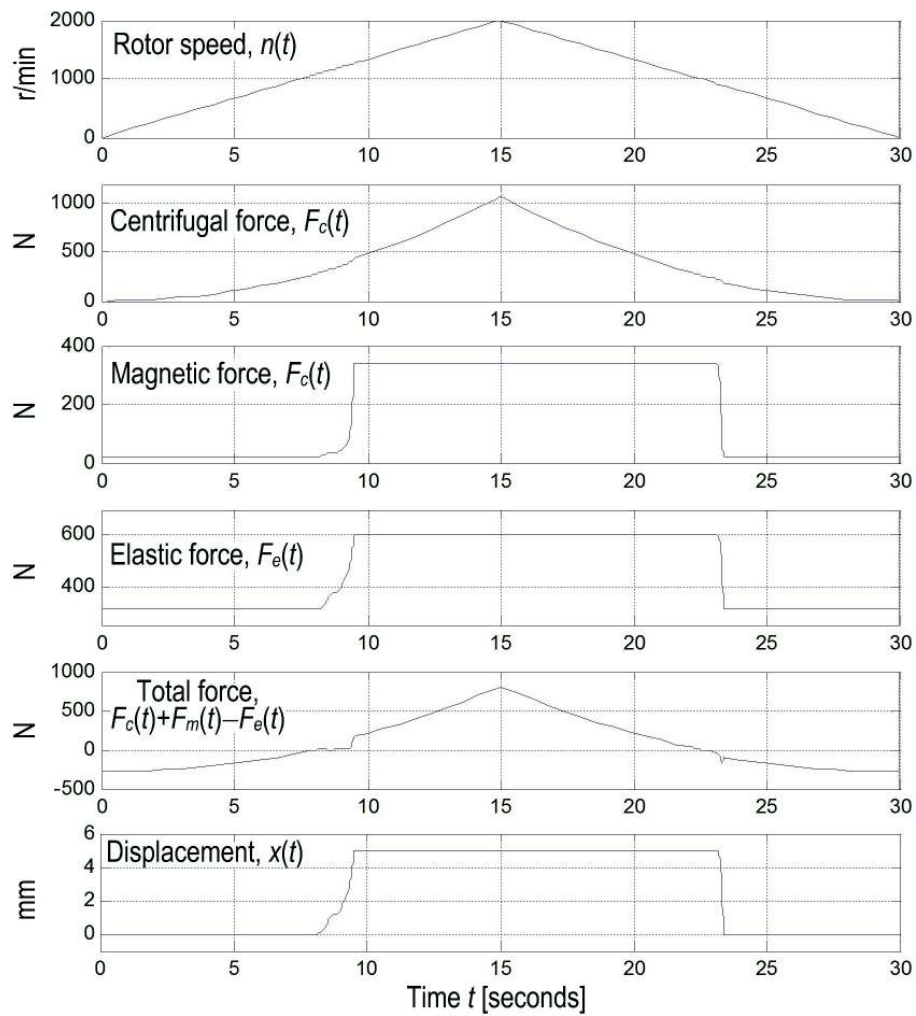
Figure 2.12: Forces acting on the mover and mover displacement x(t) for rotor speed profile n(t).

numerically to determine the displacement law $x(t)$ corresponding to any given rotor speed profile. As an example speed profile, the motor is supposed to accelerate from 0 to $2000rpm$ in $15seconds$ and then to decelerate from $2000rpm$ to standstill in the following $15seconds$ fig.2.12. The numerical integration results of equation (2.2) in terms of the forces acting on the mover and mover displacement over time for such a speed profile are shown in fig.2.12. In particular, it can be seen that, below a certain threshold speed (that we shall indicate as activation threshold, around $1200rpm$) during acceleration, the total force acting on the mover is negative (i.e. oriented downwards in fig.2.10), hence the mover remains in its rest position. Above the activation speed, the increasing centrifugal stress causes the total force to become positive and the mover to translate upwards (in the reference of fig.2.10). The mover translation from its rest position to the final position where it adheres to the pole rim is made faster by the rapidly increasing magnetic attraction exerted by the pole fig.2.11. After getting in contact with the pole rim, the mover remains in such position under the effect of a positive total force until the speed drops below a new threshold (that we shall indicate as detachment threshold). The detachment threshold can be noticed to be located at around $800rpm$, i.e. lower than the activation threshold as a consequence of the attraction force exerted by the pole rim, while would tend to retain the mover from returning to its rest position.
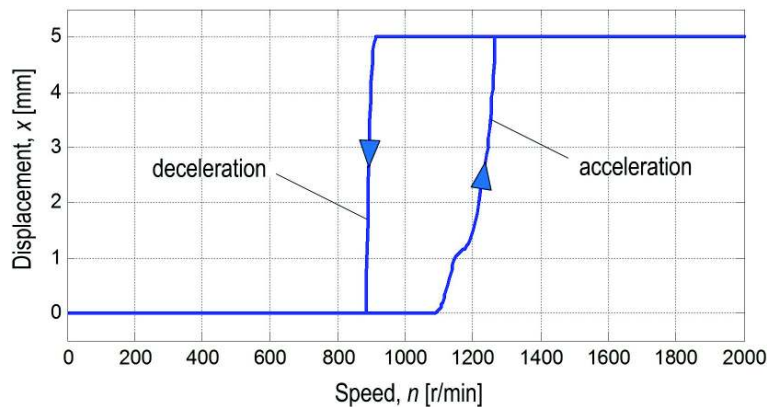
Figure 2.13: Mover displacement as a function of the rotor speed during the overall acceleration-deceleration cycle.

In other words, the flux weakening device activation is shown not to be a reversible process. To clarify this fact, we can plot the mover displacement versus the rotor speed throughout the acceleration and deceleration cycle fig.2.13. By changing the system design parameters given in Tab.2.4 and repeating the dynamic simulation presented with the new parameters, it is possible to find out the system behavior sensitivity to the various design variables. In particular, the appropriate selection of the spring constant, of the

spring preload and of the equivalent mover mass would enable the designer to noticeably change the profiles shown in fig.2.13, in particular allowing for a closer location of the activation and detachment speed thresholds. The problem is that the mentioned design variables cannot be independently and freely chosen, as they are closely related to one another, affected by technological limits and also strongly influenced by the design choices made in the overall IPM motor electromagnetic sizing. An interesting optimization development could be therefore foreseen after the prototype construction in order to maximize its performance and optimize its design. Because of the multiple objective functions to be satisfied (relating to performance, size, weight and cost) under various constraints and due to the amount of mutually-dependent design variables, the use of genetic multi-objective design optimization tools [15], [16] will be probably mandatory.

2.4 Conclusion

In this chapter a new design and technology solution has been presented to endow tangentially-magnetized IPM motors with an enhanced flux weakening capability. The most promising applications are in the electric and hybrid vehicle traction, where electric drives with an extended speed range are usually required. The design proposed is based on a self-activated flux weakening device capable of establishing a partial magnetic short-circuits in rotor magnets when the speed exceeds a given threshold. The device is triggered by the centrifugal force and basically employs a set of centrifugal clutches assembled between the motor shaft and rotor active parts. Acting on the motor electromagnetic dimensioning, the motor residual air-gap flux density after flux weakening device activation can be modulated according to performance requirements. A lumped-parameter FEA-assisted dynamic study has also been presented to investigate the proposed motor transient performance during typical acceleration and deceleration ramps. It has been noticed that the speed at which the flux weakening device activates during acceleration is necessarily higher than the speed at which it deactivates during deceleration as a consequence of magnetic attraction forces exerted by the rotor on the clutch moving parts. It has also been remarked how the predicted motor dynamic performance can be significantly modified through a proper selection of various design variables. A prototype is presently under construction to demonstrate the feasibility and effectiveness of the proposed technology. As a further development in case of successful prototype testing, extensive design and performance optimization perspectives can be foreseen based on state-of-the-art genetic multi-objective optimization tools.

2.5 Reference

[1] W.L. Soong, N. Ertugrul, "Field-weakening performance of interior permanent-magnet motors", *IEEE Transactions on Industry Applications*, vol. 38, no. 5, pp. 1251- 1258, Sep/Oct 2002.

[2] K. T. Chau, C.C. Chan, Liu Chunhua, "Overview of Permanent-Magnet Brushless Drives for Electric and Hybrid Electric Vehicles", *IEEE Transactions on Industrial Electronics*, vol. 55, no. 6, pp. 2246-2257, June 2008.

[3] M. Barcaro, N. Bianchi, F. Magnussen, "Permanent-Magnet Optimization in Permanent-Magnet-Assisted Synchronous Reluctance Motor for a Wide Constant-Power Speed Range", *IEEE Transactions on Industrial Electronics*, vol.59, no.6, pp.2495-2502, June 2012.

[4] S. Chaithongsuk, B. Nahid-Mobarakeh, J.-P. Caron, N. Takorabet, F. Meibody-Tabar, "Optimal Design of Permanent Magnet Motors to Improve Field-Weakening Performances in Variable Speed Drives", *IEEE Transactions on Industrial Electronics*, vol. 59, no. 6, pp. 2484-2494, June 2012.

[5] B. J. Chalmers, L. Musaba, "Design and field-weakening performance of a synchronous reluctance motor with axially laminated rotor", *IEEE Transactions on Industry Applications*, vol. 34, no. 5, pp. 1035-1041, Sep/Oct 1998.

[6] A. M. E. Refaie, T. M. Jahns, P. J. McCleer, J. W. McKeever, "Experimental verification of optimal flux weakening in surface PM machines using concentrated windings", *IEEE Trans. on Industry Applications*, vol. 42, no. 2, Mar./Apr. 2006, pp. 443-453.

[7] B. Stumberger, A. Hamler, M. Trlep, M. Jesenik, "Analysis of interior permanent magnet synchronous motor designed for flux weakening operation", *IEEE Transactions on Magnetics*, vol. 37, no. 5, pp. 3644-3647, Sep 2001.

[8] Xu Longya, Ye Lurong; Zhen Li; A. El-Antably, "A new design concept of permanent magnet machine for flux weakening operation", *IEEE Transactions on Industry Applications*, vol. 31, no. 2, pp. 373-378, Mar/Apr 1995.

[9] Hua Wei, Cheng Ming, Zhang Gan, "A Novel Hybrid Excitation Flux-Switching Motor for Hybrid Vehicles", *IEEE Transactions on Magnetics*, vol. 45, no. 10, pp. 4728-4731, Oct. 2009.

[10] M. Aydin, S. Huang, T. A. Lipo, "A new axial flux surface mounted permanent magnet machine capable of field control", *IEEE Industry Application Annual Meeting 2002*, vol. 2, Oct. 2002, pp. 13-18.

[11] Baoquan Kou, Chunyan Li, Shukang Cheng, "Flux-Weakening-Characteristi Analysis of a New Permanent-Magnet Synchronous Motor Used for Electric Vehicles," *Plasma Science, IEEE Transactions on* , vol.39, no.1, pp.511-515, Jan. 2011.

[12] H. Woehl-Bruhn, W.-R. Canders, N. Domann, "Classification of field-weakening solutions and novel PM machine with adjustable excitation", *2010 XIX International Conference on Electrical Machines (ICEM)*, 6-8 Sept. 2010.

[13] K.I. Laskaris, A.G. Kladas, "Internal Permanent Magnet Motor Design for Electric Vehicle Drive", *IEEE Transactions on Industrial Electronics*, vol.57, no.1, pp.138-145, Jan. 2010.

[14] H.P. Liu, Y.L. Ting, R.C. Zowarka, A. Alexander, "Electromagnetic and structural analyses of an integrated launch package", *IEEE Transactions on Magnetics*, vol. 35, no. 1, pp.74-78, Jan 1999.

[15] A. Tessarolo, V. Venuti, F. Luise, P. Raffin, "Multi-objective design optimization of a surface permanent-magnet slotless alternator for small-power wind generation", *International Conference on Clean Electrical Power*, ICCEP 2011, Ischia, Italy, 14-16 June 2011, pp. 371-376.

[16] F. Luise, A. Tessarolo, S. Pieri, P. Raffin, M. Di Chiara, F. Agnolet, M. Scalabrin, "Design and technology solutions for high-efficiency high-speed motors", submitted paper for presentation at *ICEM 2012* conference.

Chapter 3

Design, construction and testing of an IPM motor prototype with with the novel self-activated flux-weakening system

3.1 Introduction

In the previous chapter, a novel interior permanent magnet motor design with a self-activated flux-weakening device has been presented. In the same chapter its static and dynamic behavior was presented, by means of FEM analysis and lumped parameters study. In the first part of this chapter, the design and consttuction process of a motor prototype implementing the above idea will be presented in detail. Test results on the built motor prototype will be finallyshown. With respect to the basic configuration presented in the previous chaper, some design changes have been made in order to make the implementation more robust and reliable, while faithfully preserving the originary functional principle. In particular, the use of conventional centrifugal clutches as described in the previous Chapter has been discarded because of the difficulty in procuring such components with the dimensional requirements needed for the prototype. As an alternative, it has been then decided to use a custom design that will be next presented

3.2 Stator characteristics

For economic and time reasons the choice to use an already existing stator stack has been made. So the stator of an asynchronous four pole motor

with a bore diameter of $150mm$ has been chosen. Originally, the machine had four poles, but to fit prototype characteristics the original winding was removed and the stator rewound as a six-pole one. In order to have the same rated voltage as the original four pole machine, the number of coils per phase had to be increased; to do so the section of each single wire had to be decreased compared to the original design so that the coil could fit the slot dimension. In fig.3.1 the stator and the two end shields are shown.

Figure 3.1: Picture of the stator and the shields of the motor.

In table3.1 stator dimensions and characteristics are reported.

Having a series connected winding is highly recommended if not even mandatory. In fact, as it will be discussed later, the three rotor mobile yokes are not mechanically connected to each other, hence that there is no guarantee that they activate and deactivate simultaneously: due to possible slight differences in spring pre-load, is it then possible that a yoke activates when the other are still in rest position; this would bring to magnetically unbalanced pole; if stator winding phases have series connected coils, pole flux unbalance does not cause significant troubles; conversely, if it has parallels ways per phase, the unbalance in back-electromotive forces is expected to cause potentially dangerous circulating currents.

DIMENSIONS and CHARACTERISTICS OF THE PROTOTYPE STATOR		
	Symbol	mm
Stator outer diameter	D_s	210
Stator inner diameter	D_{si}	150
Number of poles	$2p$	6
Number of parallels	NP	1
Number of coils per phase	NS	240

Table 3.1: Dimensions of the prototype IPM motor

3.3 Rotor characteristics

Due to the particular topology of the IPM rotor to be implemented into the prototype machine, it was not possible to obtain by simple modification of an already existing one but it was mandatory to build it ex-novo with a custom design. The parts composing the rotor can be regrouped in five main sets:

- end discs;

- poles;

- magnets;

- magnetic yokes;

- springs;

- shaft;

witch will independently presented in appropriate sub-sections.

As said in the introduction of the chapter, the solution witch implies the usa of conventional centrifugal clutches was discarded. That was due in particular to the fact that the total radial displacement of friction pads available from off-the shelf centrifugal clutches was not enough for the specific application. Other disadvantages are the limited range of diameters among which the choice must be made. It is also to be noticed that, in most of commercial clutches, the friction pad movement is not radial. In fact, one end of the pad is fastened to the core of the clutch; this appears to be unsuitable for the particular application of moving a magnetic yoke, since it would result in a non-uniform air gap between mobile yokes and the inner rotor rim. For the mentioned reasons a new system was designed to accomplish the duty of a centrifugal flux-weakening device fig.3.2,3.3.
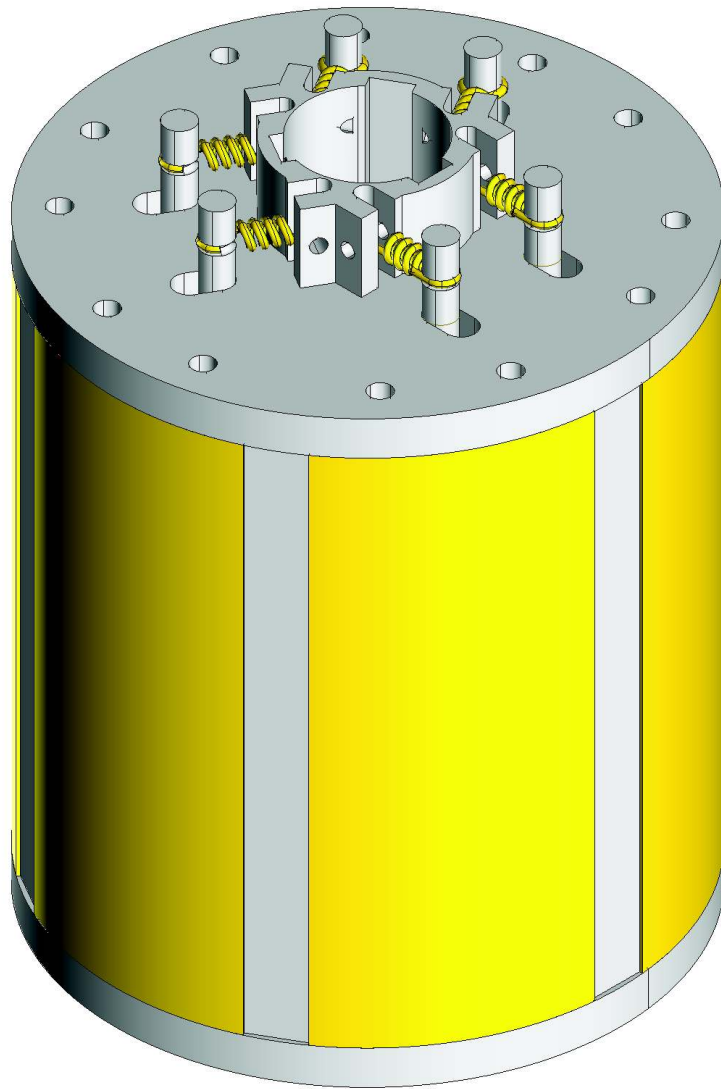
Figure 3.2: Picture of the rotor with the new centrifugal activating system.
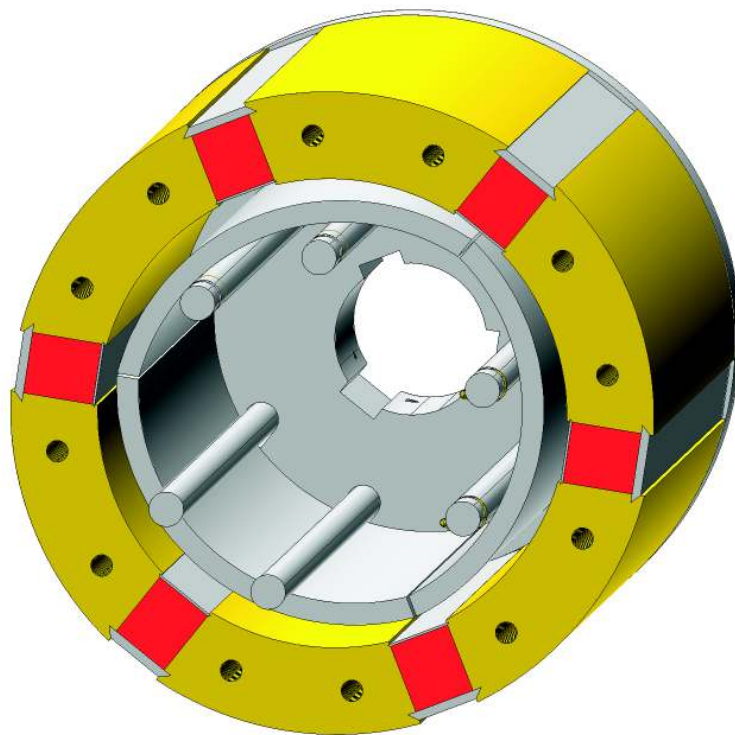
Figure 3.3: Picture of the internal view of the rotor with the new centrifugal activating system.

3.3.1 End Disc

The shape of end discs was changed compared to the initial concept described in the previous chapter fig.3.4. In fact, in the new rotor design they do not only fulfill the duty of transmitting the torque to the shaft (by means of keys) and holding the poles together, but they also have to guide the movent of the magnetic yokes in theirs radial movent; that is done thanks to six eyelet-shaped guides (two for every moving yoke). At the outer side of it, the end disc has a overhang serving as a support for spring fastening springs fig.3.5.
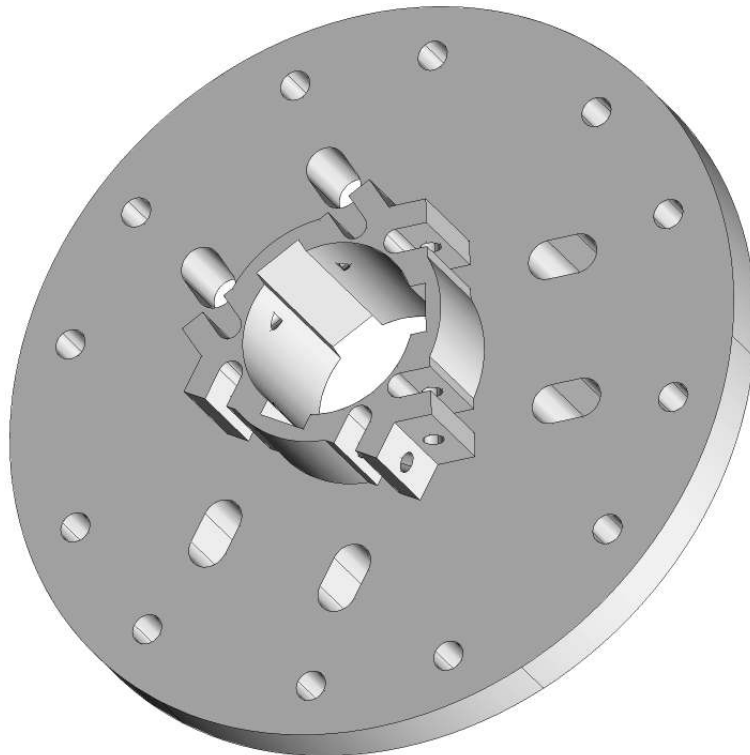
Figure 3.4: 3D view of the end disc.

It is to remembered that for the correct working of the rotor this part as to be made of a no-magnetic material; otherwise a large part of the magnets flux will find easy leakage path in it. For the prototype a AISI316 INOX steel was chosen.

3.3.2 Magnetic yoke

The shape of the magnetic yokes has also changed compared to the original design (see previous chapter),. In the original design, moving yokes simply consisted of steel plates properly shaped to perfectly fit the inner rotor pol
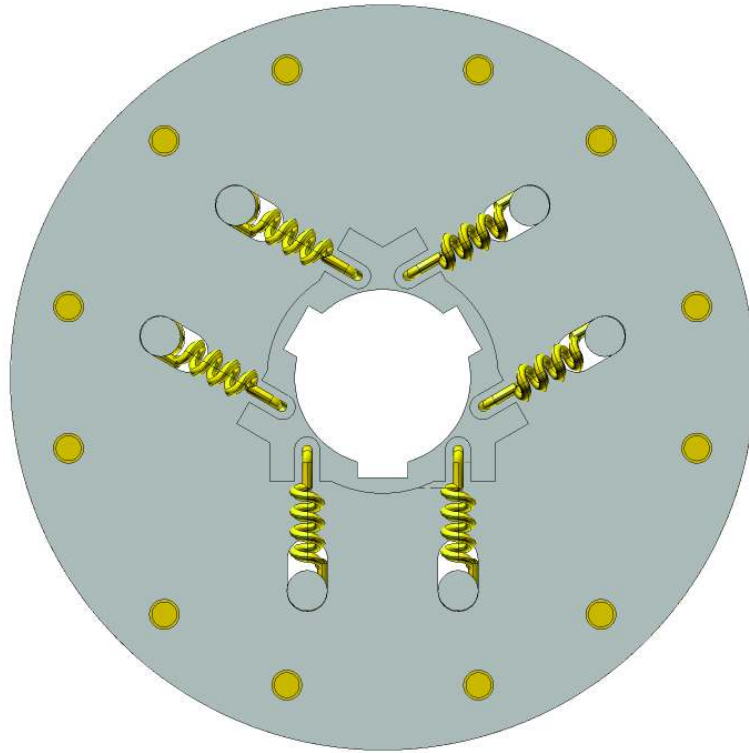
Figure 3.5: Front view of the rotor.
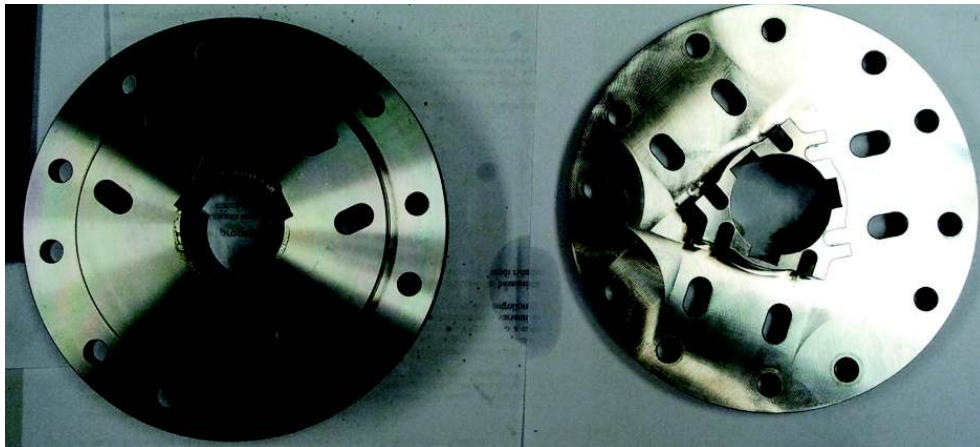
Figure 3.6: Manufactured end discs of the prototype.

surface, and welded to clutch expansions. Due to the the decision of not adopting conventional clutches, the yokes themselves became part of the centrifugal device as it happened for end discs. For this purpose, two bars are welded on the concave face of the yoke as can be seen in fig.3.7.
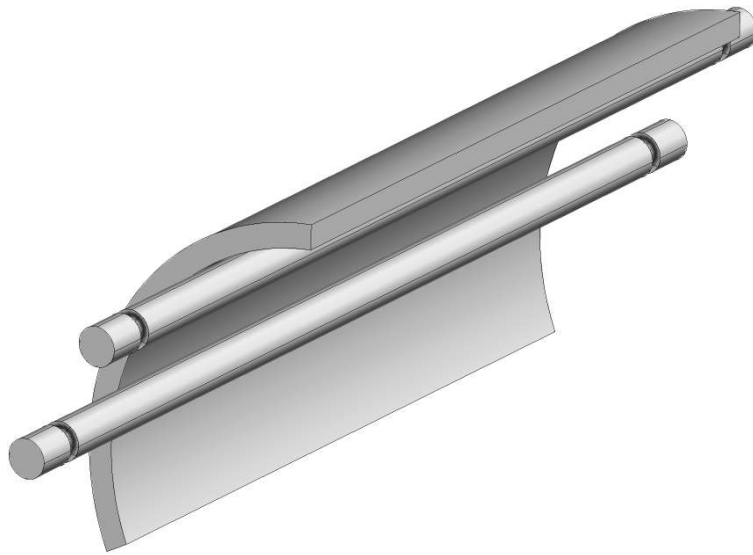
Figure 3.7: 3d representation of a magnetic yoke.

The bars serve two purposes: firstly, passing trough the appropriate eyelets of the end disc, they guide the yoke on radial direction; secondly, by means of a groove at each bar end, they allow the hooking of the springs as shown in fig.3.8.

In fig.3.9 a difference can be noted from what is show in fig.3.7; in fact, due to manufacturability issues, in the concave part of the yoke two ribs had to be machined in order to accomodate the two bars in exactly the right position. An incorrect mounting of the bars might have prevented bars from smoothly sliding along eyelet guides. The three magnetic yokes are made of Fe430B (a ferromagnetic material had to be used to draw flux lines from permanent magnets to the yokes in high speed operation)

3.3.3   Pole

Rotor poles fig.3.10 are made out of solid iron to allow an easy assembly.

At each end of the pole, two threaded holes can be found,. They have been made in a corresponded position to those (not threaded) present on the end disc, so that bolts can hold the parts together. On the inner side of each pole, grooves were milled for wedge insertion and magnet retention. On the air gap side, a more resistant wedge is needed since it has to hold the centrifugal force acting on the magnet. So a 2.5mm height wedge was
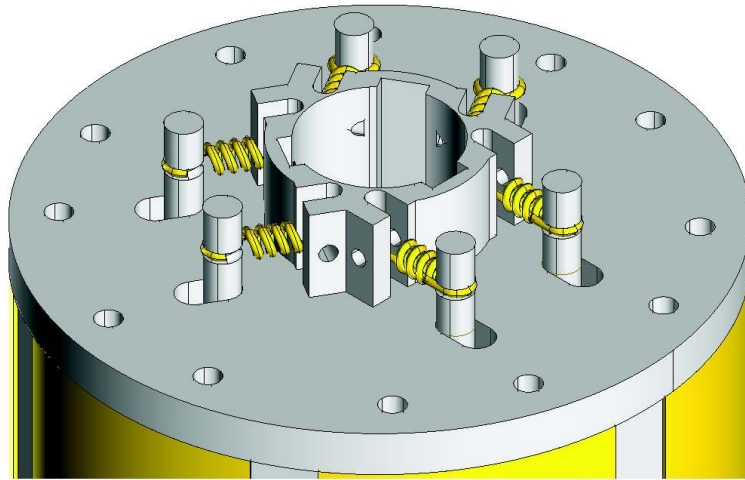
Figure 3.8: Zoom on the yoke end bar and spring coupling.
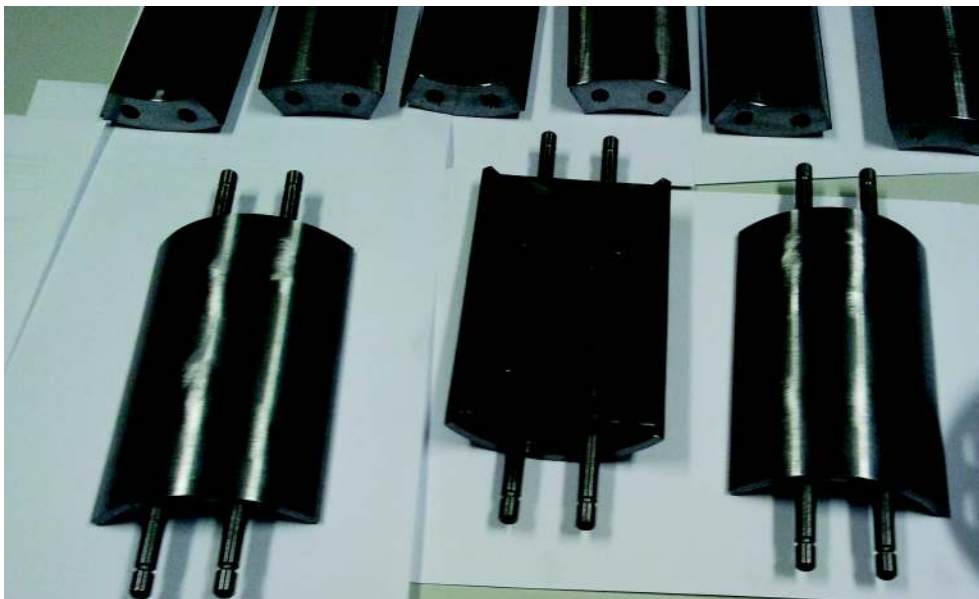
Figure 3.9: Picture of the three manufactured yokes.
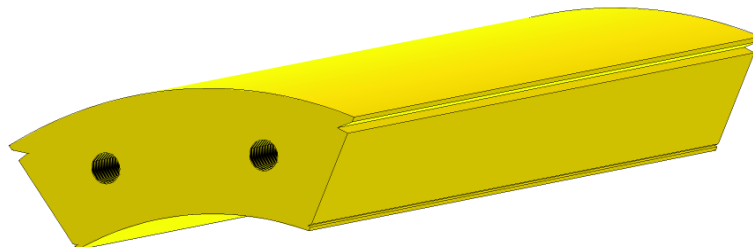
Figure 3.10: Representation of a rotor pole.

choused; on the contrary, the wedge on the shaft side of the pole has merely the duty of protecting the magnet, since no force act on the magnet pushing it towards the shaft, except for the gravity force.; so a $0.5mm$ height wedge was chosen.

The material chosen for the pole is Fe430B. The completed poles can be seen in fig.3.11.
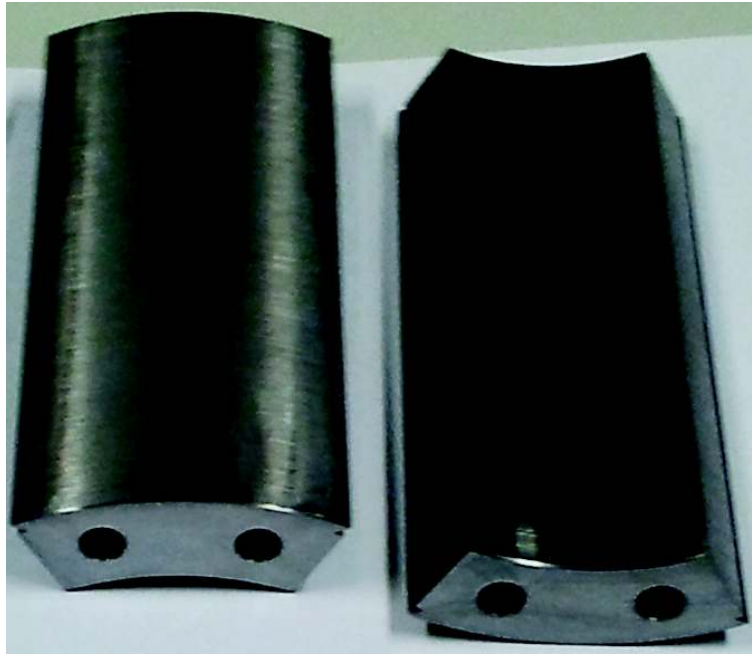
Figure 3.11: Picture of two of the six realized poles.

3.3.4   Magnets

For its high coercivity force Neudinium Iron Bore magnets were chosen, whose characteristics are shown in tab.3.2

MAGNETS MEASURED CHARACTERISTICS		
Symbol	$Unit$	$Value$
B_r	mT	1249
bH_c	kA/m	976.5
jH_c	kA/m	1585.3
$(BH)_{max}$	kJ/m^3	306.68

Table 3.2: Magnets test report

3.3.5 Spring

Four extension springs for each yoke are used; one end of each spring is mounted on the yoke rods passing trough the end disc and the other end is bolted to the end disc as shown in fig.3.15. Every springs consists of three turns of harmonic steel with one half loop over center ends; the two ends lie on perpendicular planes fig.3.14.

Figure 3.12: Picture of the manufactured springs.

3.3.6 Shaft

As regards the steel shaft, fig.3.13, the only two things to be mentioned is that its diameter is a few millimeters larger in the middle so that the end discs can axially fit it and the six keys are located where the change of diameter takes place. Keys are meant to transfer the torque from the end discs to the shaft.

Figure 3.13: Picture of the manufactured shaft.

3.3.7 Realized rotor

Putting all the previous components together fig.3.14 the rotor has been assembled as can be seen in fig.3.15,3.16.

Figure 3.14: Picture of the parts of the rotor.
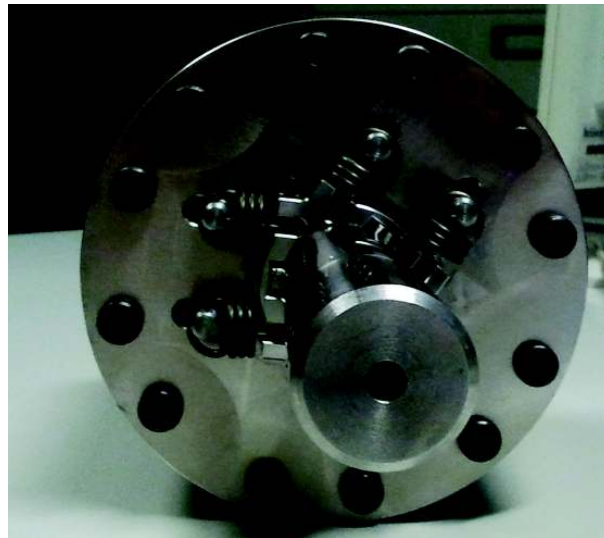
Figure 3.15: Picture of one side of the rotor.
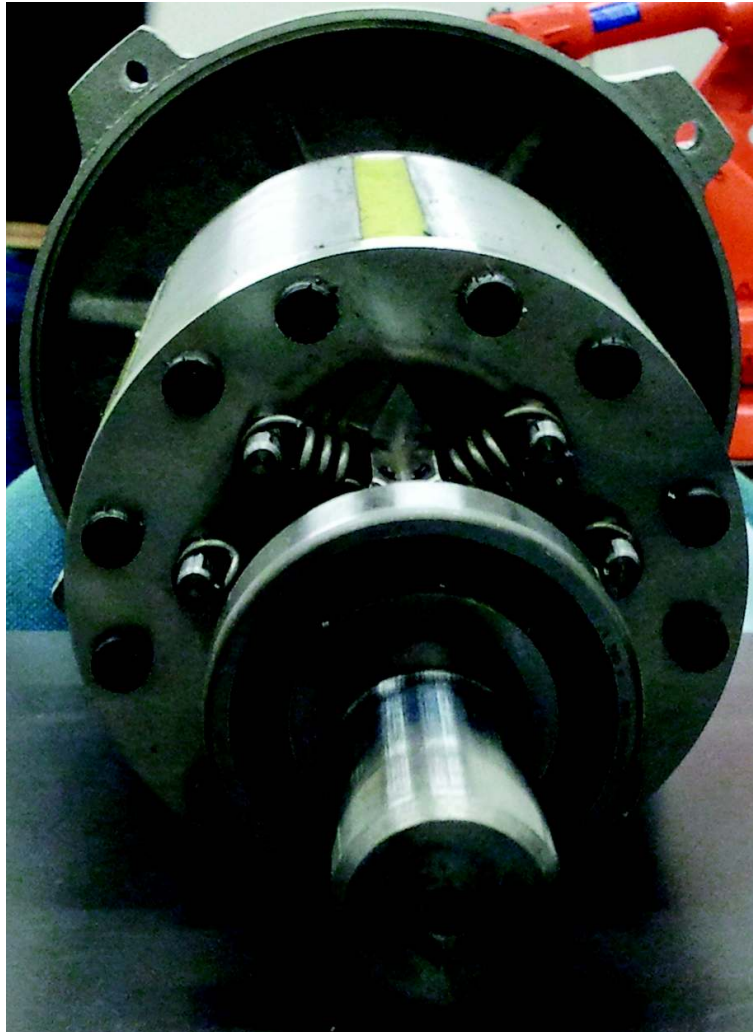
Figure 3.16: Picture of the rotor with the magnets inserted and the bearings and one shield mounted.

3.4 Prototype Testing

A test bench for the motor has been set up to verify the effectiveness of the flux-weakening device fig.3.17. To do so the motor has been coupled to a speed-controlled induction machine, so that the back electromotive force of the prototype could be measured as a function of speed to assess the effectiveness of the self-activated flux-weakening system.
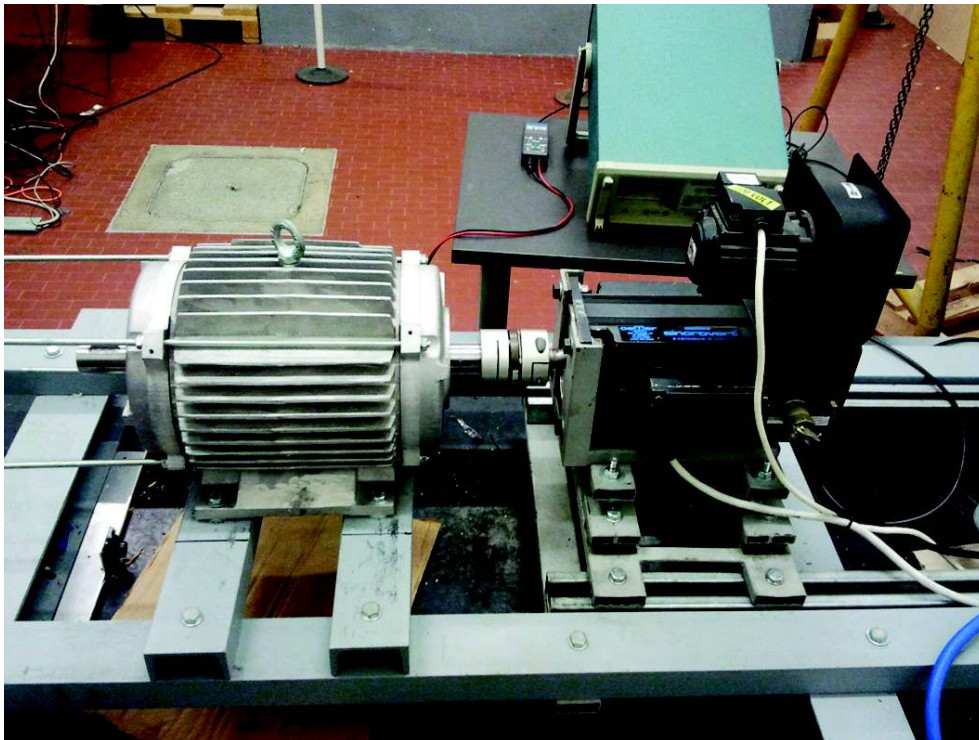
Figure 3.17: Test bench.

Measures were collected both in acceleration and deceleration ramps, performed by steps of speed.

In fig.3.18 the phase to phase back electromagnetic force when the rotor spins at $1000rpm$, (rated speed at 50 Hz) is show in the two cases of both acceleration and deceleration ramps.

By means of 3.1 the phase linkage-flux λ can be found from the phase to phase voltage V and the frequency f.

$$\lambda = \sqrt{\frac{2}{3}} \frac{V}{4.44f} \tag{3.1}$$

In fig.3.19 the linkage-flux versus frequency is show, either in acceleration and in deceleration ramps. Two main observations can be made:
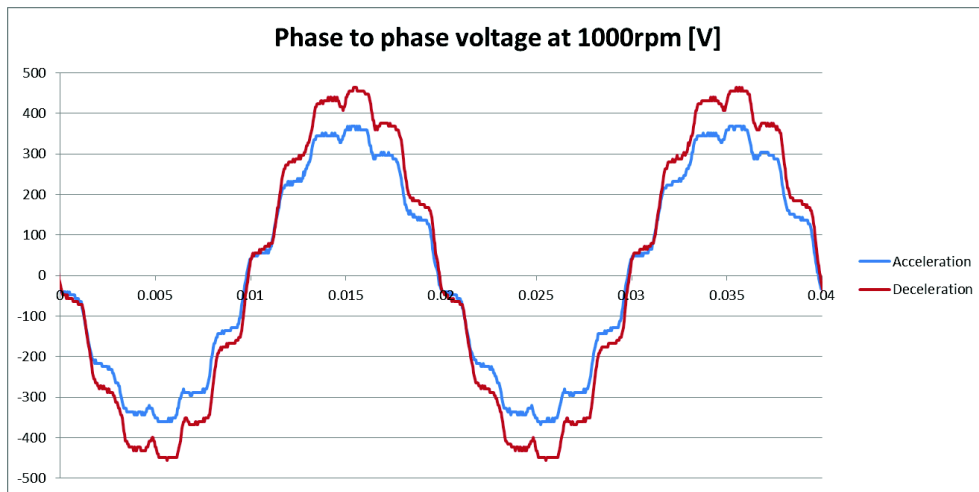
Figure 3.18: Measured phase to phase back electromagnetic force when the rotor spin at $1000rpm$.

1. It can be noted that the flux linkage variation during both acceleration and deceleration does not happen abruptly (namely in a stepwise manner) but by steps. This is due to the fact that the three mobile yokes do not activate simultaneously, but at slightly different speeds. This is due to the small inevitable differences in the elastic force exerted by the various springs, which result in the yokes to move radially at different instants although subject to the same centrifugal force.

2. it can be noted that a sort of "*hysteresis*" effect occurs. In other words, the flux weakening behavior observed during the acceleration ramp is found not to be reversible. During deceleration, in fact, the flux linkage exhibits a different variation with the speed compared to the acceleration ramp. Such irreversible behavior is due to the magnetic attraction force arising between the mobile yoke and inner pole rim. The presence of such a force was well predicted in the analysis and dimensioning stage (see previous chapter) along with the consequent irreversible ("*hysteretic*") behavior.

The exact points of attaching and detaching of the different yokes can be found by analyzing fig.3.19. We can see that below $800rpm(40Hz)$ all the yoke still in rest position, which means that the machine runs under full phase flux; when the speed approaches $1000rpm(50Hz)$, the yokes are moving towards the inner rotor circumference and due to slightly reduced air gap some flux-weakening performance appears; at $1100rpm(55Hz)$ two of the three yokes attach to the inner rotor circumference so in the range of $100rpm$ a sudden decrease in the linkage flux happens until the entire flux weakening device is activate at $1500rpm(75Hz)$ and the full flux-weakening
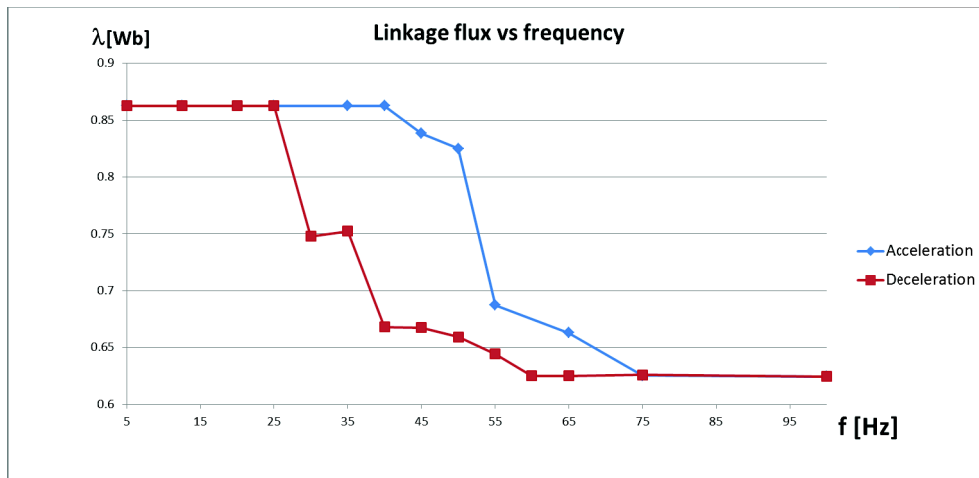
Figure 3.19: Phase linkage flux versus frequency in acceleration and deceleration ramps.

capability is deployed. In the deceleration stage, it can be noticed that above $1200rpm(60Hz)$ the flux maintains weakened at the maximum possible extent allowed by motor design; then, yokes are gradually recalled by the springs into rest position; at $800rpm(40Hz)$ one of the three yokes reaches its rest position then at $700rpm(35Hz)$ only one yoke remains activated; it can be found that the machine return to its full-flux state at $500rpm(25Hz)$.
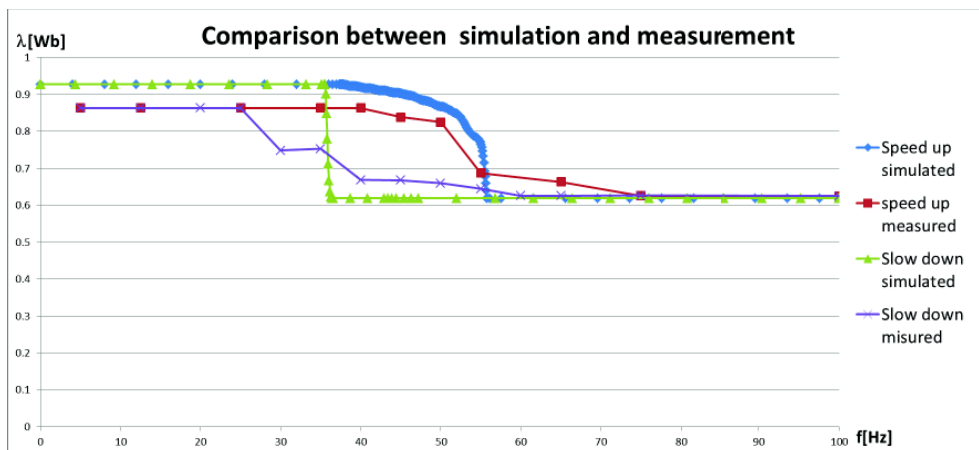
Figure 3.20: Comparison between simulation results and measures.

The comparison between the simulated behavior of the machine and the test results on the prototype are proposed in fig.3.20. It can be noticed how the flux-weakening performances predicted with the dynamic model of the machine are quite well followed by measurements; the way of passing

56

between the two states (full-flux and flux-weakening) presents some discrepancies especially in the decelerating ramp were the simulation presents a step wise behavior while the measured -flux linkage presents a smoother evolution; as said before that is due to the non simultaneous movement of the three rotor magnetic yokes. Actually, such a gradual behavior represents an advantage with respect to the abrupt change predicted by simulations, because having a sudden change in machine flux can cause some issues from the control viewpoint.

Chapter 4

Multi-objective optimization of a reluctance assisted synchronous motor

4.1 Introduction

An other type of motor world-wide acknowledged to be suited for auto motive traction application the synchronous permanent magnet reluctance assisted motor (SPMR)[1]-[6]. In this chapter the multi-objective optimization of the design of this type of motor fig.4.1 is presented. The performance of the machine is influenced by a large number of variables that can be grouped into three main categories: materials, geometry and cost [7],[8]. The optimization has been carried out numerically by means of a genetic multi-objective optimization algorithm combined with a finite-element code. For this study it was decided to focus only on the rotor geometry and not on the entire machine, that means that only the geometry of the rotor is changed by the optimization algorithm while the stator is always the same. Two objectives for the optimization algorithm were chosen as follows: first is the maximization of the torque, that tends to increase the size of the magnet and consequently the cost of the motor; the second is the minimization of the demagnetizing current, defined as the current needed to totally counteract the flux due to the magnets. The latter objective tends to minimize the size of the magnets, since all the designs being considered in the optimization have the same stator and consequently the same rated current.

4.2 Model and optimization variable

Since the motor under study has to be placed into a vehicle, it has been chosen to fix its external dimensions, in particular a stator diameter $D_s = 500mm$; the stack length is to be chosen afterwards based on the torque
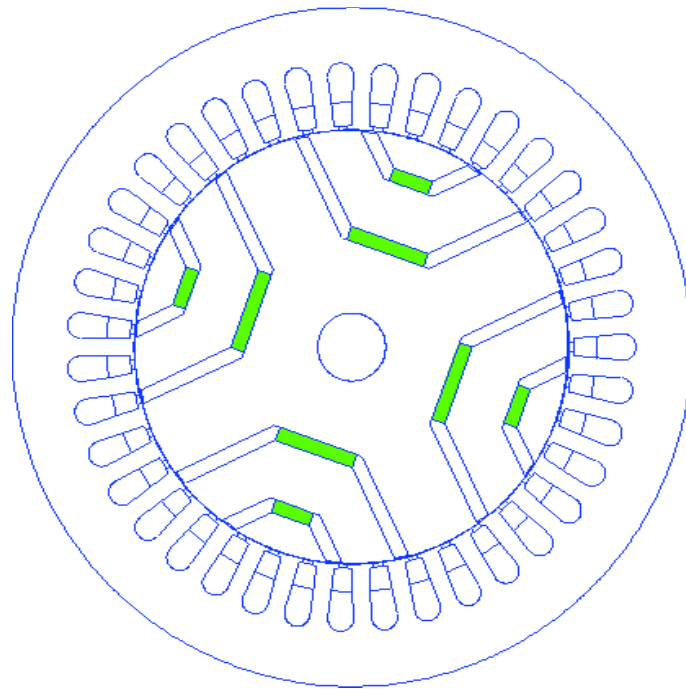
Figure 4.1: Example of synchronous reluctance motor with the permanent magnets highlighted in green.

that the motor is required to deliver. As already said, the attention is posed on the rotor geometry so the stator geometry and materials are defined and they do not take part in the optimization process. As a consequence, also the rotor diameter and the air gap are set as constant values.

Figure 4.2: Example of semi-closed stator slot.

In Table4.1 the the stator characteristic data are presented; to reduce the torque ripple, a fractional slot winding was chosen (39 slots, 4 poles),

DIMENSIONS OF THE MODEL STATOR		
	Symbol	$[mm]$
Stator outer diameter	D_s	500
Stator slot height	h_s	48
Rotor outer diameter	D_r	320
Air-gap width	θ	0.5
Number of slots	NS	39
Tooth width	WT	13
Number of poles	$2p$	4

Table 4.1: Dimensions of the model stator
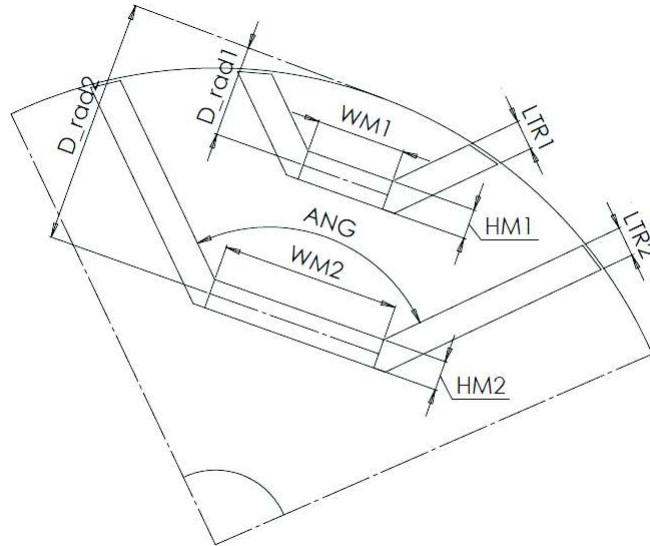
Figure 4.3: Rotor geometry optimization variables.

60

and semi-close slots are used to mitigate cogging torque effects fig.4.2.

For the rotor a two layer topology was chosen as show in fig.4.1; as said the rotor diameter is fixed at $D_r = 320mm$ so the optimization variables are the dimension and the radial position of the magnets, the width of the air ribs and their opening angle (fig.4.3). It worth noting that it is imposed that the air ribs of the the two layers are parallel. In Tab.4.2 the nine optimization variables with their respective range can be found.

OPTIMIZATION VARIABLES AND RANGES			
Symbol	Layer 1	Layer 2	$[Units]$
WM	$20-60$	$60-100$	$[mm]$
HM	$3-12$	$3-12$	$[mm]$
LTR	$3-15$	$3-15$	$[mm]$
D_{rad}	$10-70$	$50-150$	$[mm]$
ANG	$30-120$		$[deg]$

Table 4.2: Optimization variables and ranges

Another constraint imposed on the rotor geometry is the width of the iron bridge that close air ribs, for mechanical reason its it is imposed to be $1.5mm$ wide.

As far as materials are concerned, an high grade Samarium Cobalt characterized by a coercitivity force of $Hc = 900000A/m$ was chosen for the magnets, mainly due its high resiliency to temperature stresses.

In fig.4.4 the BH curve of the ferromagnetic material chosen for the motor is reported.

The optimization problem stated above is a multi-objective problem with nine constrained design variables. The objective functions are the torque T to be maximized and the demagnetizing current I_sm defined as the part of the rated current needed to cancel permanent magnet flux (4.1) ,to be minimized; also a supplementary constrain was implemented, namelythat in any case the torque as to be higher than a minimum value.

$$I_{sm} = \frac{\lambda_M}{L_d I_N} \tag{4.1}$$

where:

I_{sm} is the demagnetizing current expressed in p.u;

λ is the phase linkage flux due to the magnets;

L_d is the direct axis inductance;

I_N is the rated current of the motor.
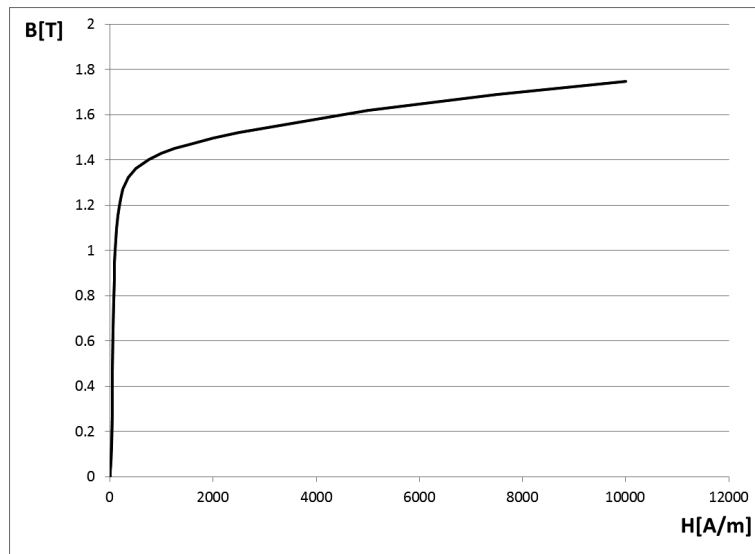
Figure 4.4: Saturation curve of the silicon steel used for the motor core.

4.3 Optimization results

The optimization problem has been implemented in the program `ModeFontier` (fig.4.5), that launch a sequence of FEM simulations in which the direct axis inductance L_d and quadrature axis inductance L_q are calculated; then, throught a series of magneto-static simulations, the maximum torque that the specific rotor geometry is capable of providing is found. Next, thanks to a multi-objective genetic optimization algorithm the nine design variable are changed in accordance with the objective functions an the constrains.

In fig.4.6 the pareto front in the objective function space is highlighted in green. Since the optimization under study is a two-objective one, the choice of the "*best solution*" is non trivial. In fact, from the optimization point of view all the designs on the pareto front are equivalent and the choice of the best design must be related to the entire system behavior (energy management strategy, battery pack, torque-power requirement,...).

For description, it has been chosen to show the two opposite designs and a middle solution., In Tab.4.3 the solution that presents the highest torque is reported; then in Tab.4.4 the antipodes pareto front solution characterized by the minimum demagnetizing current are characterized.
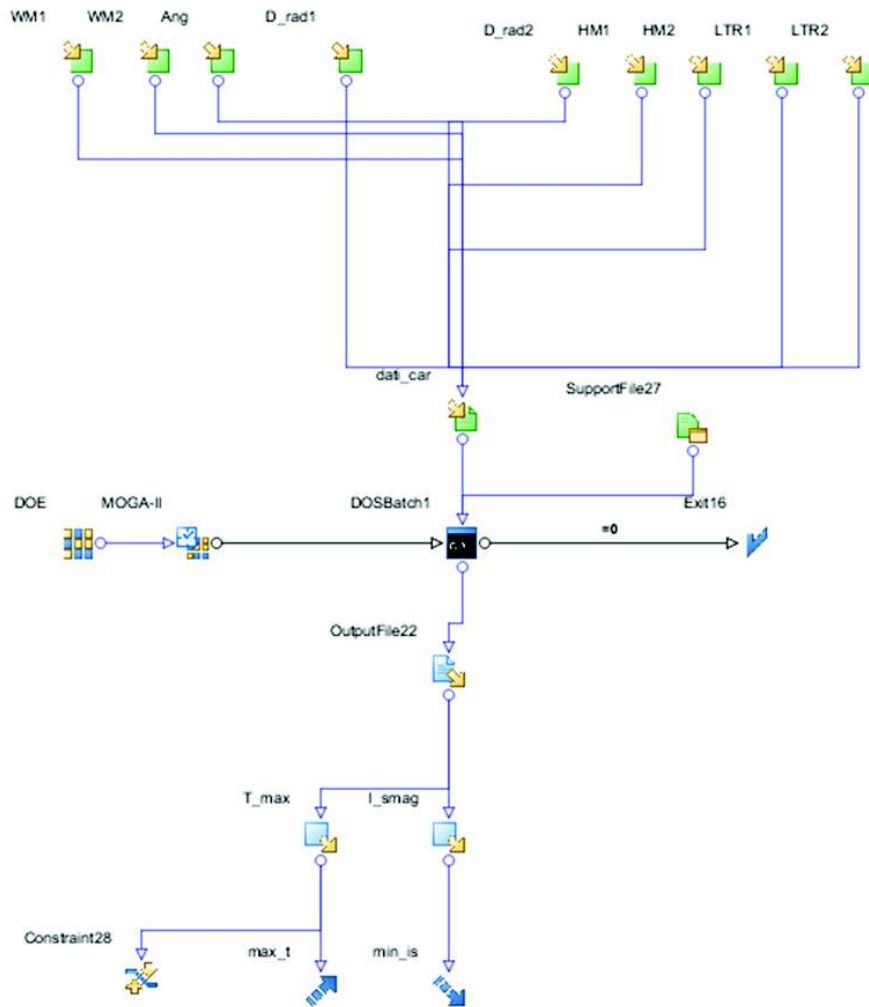
Figure 4.5: Workflow in `ModeFrontier`.
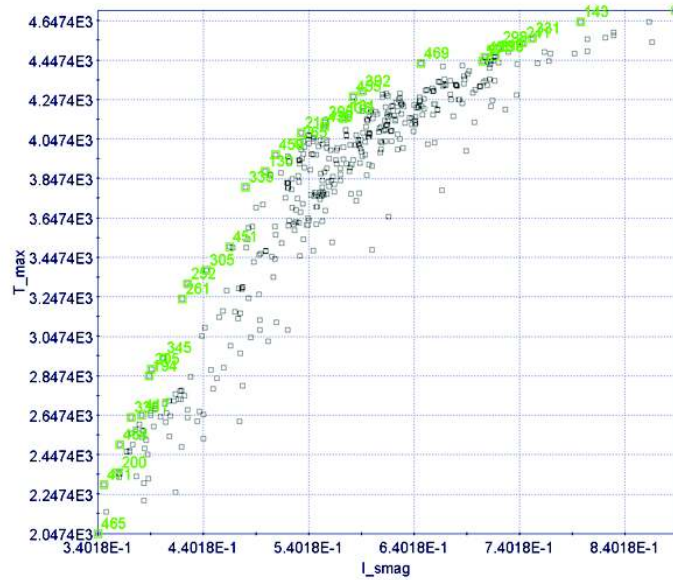
Figure 4.6: Pareto front in the objective functions plane $(T[Nm], I_{sm}[p.u.])$.
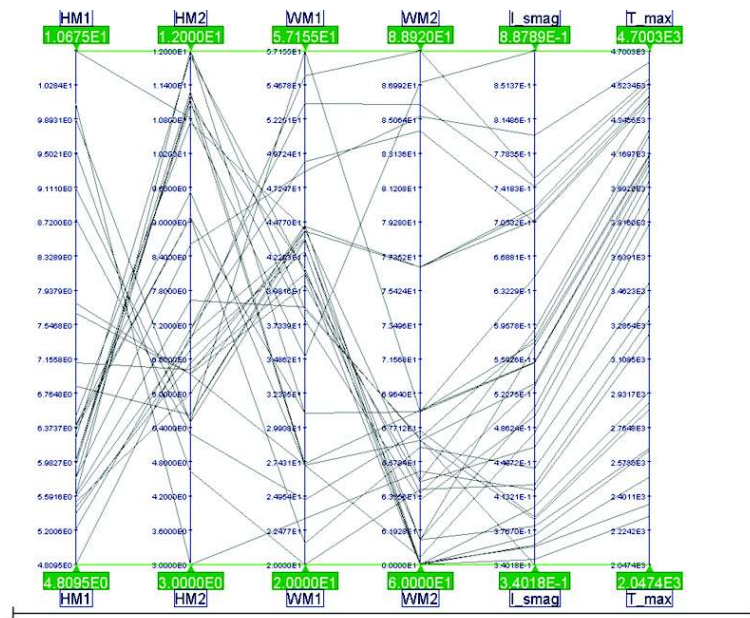
Figure 4.7: Variables and objective of the pareto front's designs.
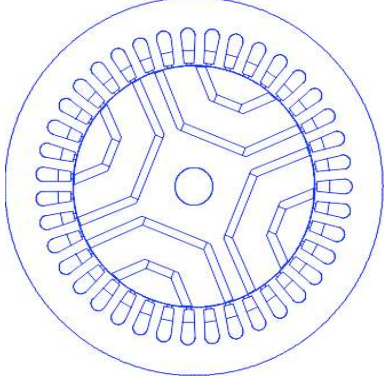
HIGHEST TORQUE CONFIGURATION FOUND			
$T = 4700Nm, I_{sm} = 0.8879 p.u.$			
Cross section of the motor	variable	value	[units]
	ANG	88.456	[deg]
	$D_{rad}1$	40.7	[mm]
	D_{rad2}	91.9	[mm]
	$HM1$	10.7	[mm]
	$HM2$	10.8	[mm]
	$LTR1$	12.0	[mm]
	$LTR2$	11.4	[mm]
	$WM1$	35.0	[mm]
	$WM2$	87.1	[mm]

Table 4.3: Highest torque configuration, cross section and variables.
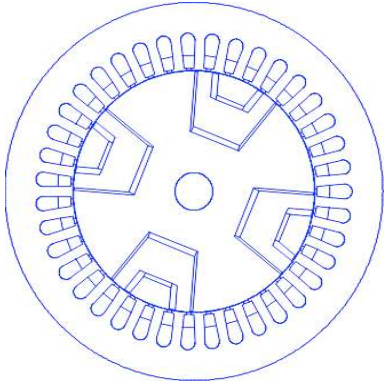
LOWER DEMAGNETIZING CURRENT CONFIGURATION FOUND			
$T = 2047Nm, I_{sm} = 0.3402 p.u.$			
Cross section of the motor	variable	value	[units]
	ANG	34.671	[deg]
	$D_{rad}1$	33.1	[mm]
	D_{rad2}	83.9	[mm]
	$HM1$	5.6	[mm]
	$HM2$	7.6	[mm]
	$LTR1$	8.6	[mm]
	$LTR2$	3.0	[mm]
	$WM1$	38.6	[mm]
	$WM2$	67.0	[mm]

Table 4.4: Lower demagnetizing current, cross section and variables.

4.4 Conclusions

Synchronous permanent magnet assisted motors find large approval for auto motive applications. In this chapter a multi-objective design optimization based on FEM model of the motor has been presented. The two objective functions were the maximum torque and the minimum demagnetizing current. The optimization is focused only on rotor geometry to limit the number of variables, that even so are in number of nine. The pareto front and two opposite solutions are shown, since a single optimal solution cannot be univocally determined in a multi-objective optimization problem.

4.5 Reference

[1] N. Bianchi and S. Bolognani, "Parameters and volt-ampere ratings of synchronous motor drive for flux-weakening applications", *IEEE Transactions on Power Electronics*, vol. 12, pp. 895-903, Dec 1997.

[2] B. E. Donald, D.W. Novotny, and T. A. Lipo, "Field weakening in buried permanent magnet ac motor drives", *IEEE Transactions on Industry Applications*, vol. 21, no. 2, pp. 398-407, Mar-Apr 1987.

[3] A. Fratta, A.Vagati, and F. Villata, "Design criteria of an IPM machine suitable for field-weakened operation", *Proc. of International Conference on Electric Machines*, ICEM, pp. 1059-1064, Sept. 1990.

[4] T. Jahns, G. Kliman, and T. Neumann, "Interior PM synchronous motors for adjustable speed drives", *IEEE Trans. on Industry Applications*, vol. IA-22, no. 4, pp. 738-747, July/Aug 1986.

[5] T. Jahns, "Flux-weakening regime operation of an interior permanent magnet synchronous motor drive", *IEEE Trans on Industry Applications*, vol. IA-23, no. 3, pp. 681-689, May 1987.

[6] A. Fratta, A. Vagati, and F. Villata, "Permanent magnet assisted synchronous reluctance drive for constant-power application: Drive power limit", *In Proc. of Intelligent Motion European Conference*, PCIM, pages 196-203, April Nurnberg, Germany, 1992.

[7] N. Bianchi and S. Bolognani, "Design optimisation of electric motors by genetic algorithms", *IEE Proceedings - Electric Power Applications*, vol. 145, no. 5, pp. 475-483, Sep. 1998.

[8] T. Matsuo and T.A. Lipo, "Rotor design optimization of synchronous reluctance machine", *IEEE Transactions on Energy Conversion*, vol. 9, no. 2, pp. 359-367, Jun. 1994.

Chapter 5

A New Magnetic Wedge Design for Enhancing the Performance of Open-Slot Electric Machines

In electric machines with open-slot stator design, magnetic wedges are often used to improve the flux-density profile in the air-gap by reduction of slotting harmonics [1], [2], [3]. A possible drawback of magnetic wedges is the increase of the phase inductance values due to the low reluctance paths through which slot leakage flux can pass [2]. In the field of vehicular traction permanent-magnet motors, high-power machines are often required which need to be fed from low-voltage sources, resulting in large rated current values. As a consequence, the stator needs to be wound with flat turns instead of round wire. As an example, fig.5.1 shows the stator of an axial-flux in-wheel motor designed for boosting the peak torque performance of a large vehicle; it can be seen that the stator coils are made of flat turns. The use of flat turns is also beneficial in terms of insulation resilience to PWM spikes coming from the supplying inverter. As a result of flat turn winding, an open slot design needs to be adopted. In absence of magnetic wedges and other design provisions, the large slot openings would interact with rotor permanent magnets giving highly harmful cogging torque effects [3]. The use of magnetic wedges is then often mandatory. In vehicular traction applications, the use of magnetic wedges is also important because it enables the designer to increase the stator phase inductance, which is usually desirable for limiting the current needed in flux weakening operation [2], [4], [11]. In this chapter, a novel magnetic wedge design is presented [6] which is particularly suitable to fit the needs of highpower electric motors for vehicular traction applications. In the chapter, the proposed wedge design is described and its possible application illustrated through some study cases.

The advantages of this design are highlighted by means of finite element (FE) analysis also showing the criteria for selecting the appropriate wedge dimensions and shape to fit the particular application requirements; it will also be shown the optimal wedge geometry in order to minimize the cogging torque amplitude for a given surface permanent-magnet machine structure. The problem is numerically solved by means of a genetic optimization algorithm combined with a finite-element code for automatic cogging torque calculation.

Figure 5.1: Axial flux machine for a in-wheel automotive application. The stator design features flat-turn windings placed in open slots.

5.1 New wedge design

The proposed magnetic wedge design is shown in fig.5.2. It is obtained from a usual magnetic wedge by milling a straight hollow groove along the wedge length. The groove is then filled with a non-magnetic bar which serves a purely mechanical function of increasing wedge robustness. By using suitable milling cutters, it is possible to shape the nonmagnetic portion of the wedge with different geometries, widths (w) and depths (h) as shown in fig.5.3a and different positions with respect to the center of the wedge. Furthermore, by changing the milling direction, the groove can be properly slanted with respect to the wedge axis (fig.5.2) so as to obtain a stator skewing-like effect. When the machine is in load conditions, the slot leakage flux causes the magnetic wedge to strongly saturate in the region placed under the non-magnetic portion. Therefore, to a good approximation, the wedge behaves as if it had a full rectangular opening of width w as shown in fig.5.3b. In the following of the chapter, the simplified model shown in fig.5.3b will be then adopted for the proposed wedge design. Even in absence
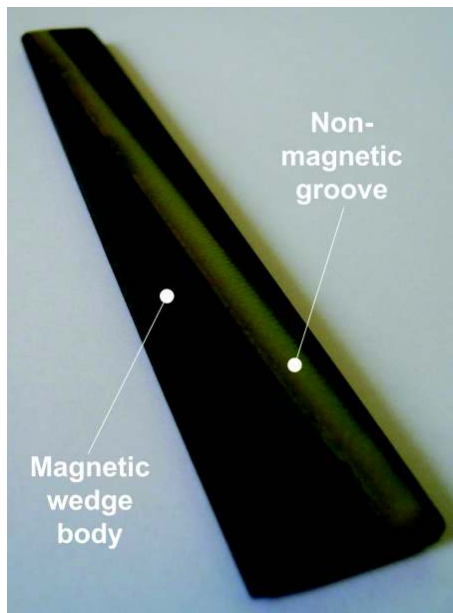
Figure 5.2: Magnetic wedge prototype with slant non-magnetic groove.
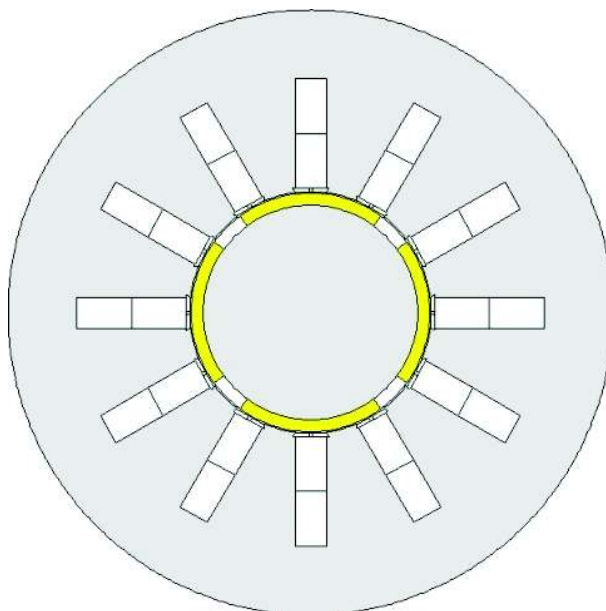
Figure 5.3: Sample surface permanent-magnet machine considered for opti-mization.

of important saturation, finite element analyses clearly show that no significant changes occur in machine parameters and performance when passing from the actual configuration (fig.5.3a) to the simplified one (fig.5.3b). It
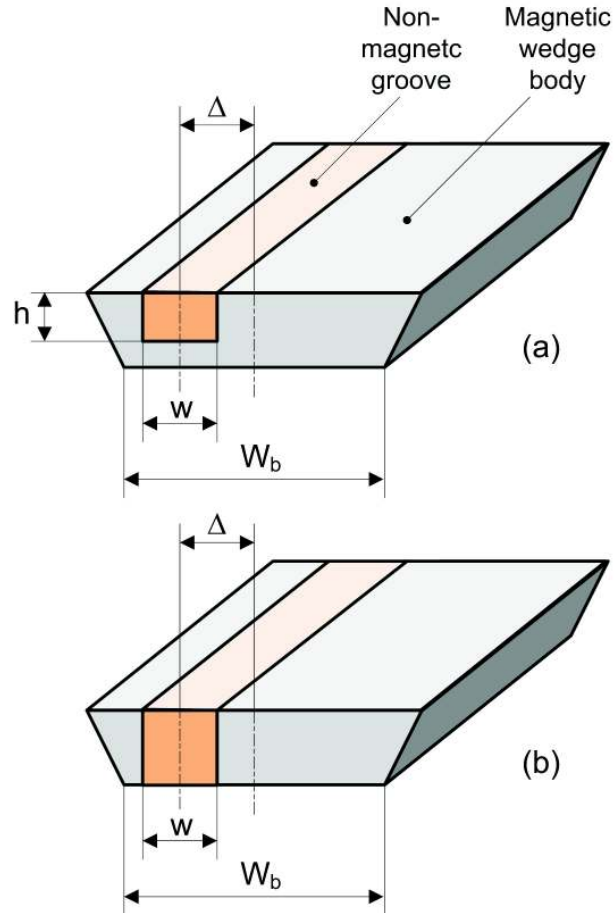
Figure 5.4: Scheme of proposed magnetic wedge geometry and dimensions.

is thereby easily understood that, from a magnetic viewpoint, the use of the proposed wedge design is practically equivalent to the non-uniformly distributed teeth method discussed in [3]. Unlike the non-uniformly distributed method, however, the adoption of the wedge design herein described does not imply any modification in stator core (slots can be then obtained from ordinary punching processes and tools) and the manufacturing modification with respect to usual machines is confined in the magnetic wedges. The main influences of the proposed magnetic wedge design on permanent-magnet motor performance can be observed in terms of cogging torque and stator phase slot leakage inductance. These two effects determine the most convenient cross-section design of the wedge depending of the specific application. They will be hereinafter explored by FE analysis on a sample surface

permanent-magnet (SPM) motor shown in fig.5.12. The characteristic data of the sample machine are summarized in Table5.1.

SAMPLE MACHINE DATA	
Number of poles	4
Number of slots	12
Permanent magnet thickness	10 mm
Permanent magnet span	0.8
Permanent magnet coercivity	900 kA/m
Permanent magnet permeability	1.05
Air-gap width	1 mm
Core magnetic permeability	10000
Magnetic wedge permeability	100
Stator bore diameter	200 mm
Stator slot opening	26 mm

Table 5.1: Sample machine data

5.2 Study of wedge design effect on stator leakage inductance

The phase inductance value L is important for machine performance for different reasons. Let us first consider the operation in rated load conditions. A phasor diagram is represented in fig.5.5a for the case (which normally occurs in practice) when the current is fully oriented in the q-axis direction (ω_n is the rated speed, λ the permanent-magnet flux linkage, V the terminal voltage, $\cos \phi$ the power factor and I_n the rated current).
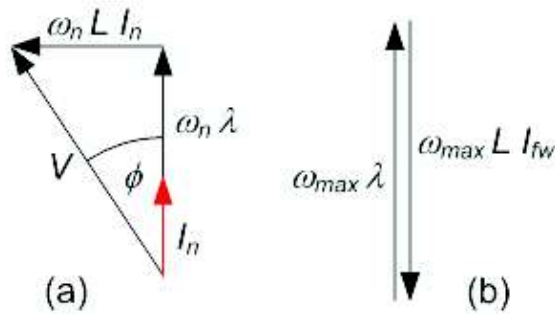
Figure 5.5: Phasor diagram for (a) operation at rated load; (b) flux-weakening operation.

It can be easily seen from fig.5.5a that the angle ϕ can be expressed as

71

$$\phi = \arctan\left(\frac{\omega_n L I_n}{\omega_n \lambda}\right) = \left(\frac{L I_n}{\lambda}\right) \qquad (5.1)$$

and therefore increases when L increases. This would make it desirable to have low values of L in order to achieve a good power factor.

On the other side, during flux-weakening operation at maximum speed ω_{max}, we can approximately write (fig.5.5b, [12]):

$$I_{fw} = \frac{\omega_{max}\lambda}{\omega_{max}L} = \frac{\lambda}{L} \qquad (5.2)$$

where I_{fw} is the flux-weakening current. Equation (5.2) shows that a large inductance L makes it possible to beneficially reduce the flux-weakening current. This would lead the designer to raise the value of L as much as possible [2], [4], [11]. Finally, a large value of L helps reduce the short-circuit current, which is very important especially in permanent-magnet machines to avoid demagnetization during faults [10]. The proposed wedge design gives the possibility to easily change the phase inductance by acting on the width w (5.3b). Quantitatively, fig.5.6 shows how the phase inductance L of the sample motor described above (fig.5.12, Table 5.1) varies with the dimension w. The inductance value for $w = 20mm$ (equal to the slot opening) represents the value which we would have without magnetic wedges. As w decreases, the inductance increases due to the diminishing reluctance of slot leakage flux paths. For very small values of w, the inductance can be increased by more than 50% with respect to the non-magnetic wedge case.
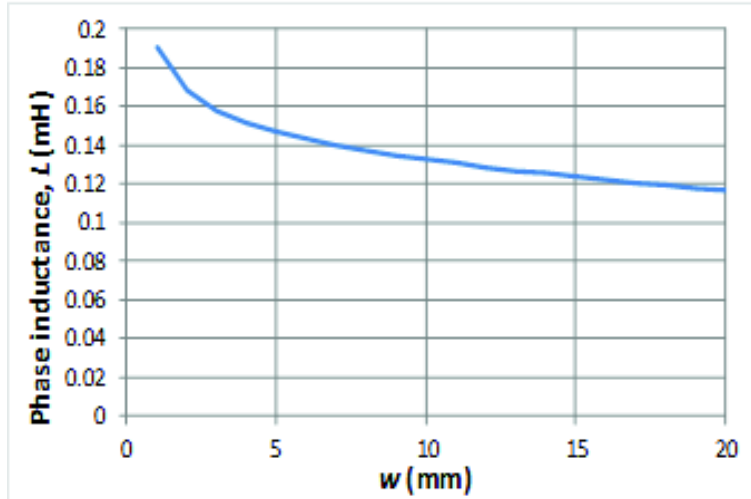
Figure 5.6: Phase inductance as a function of the wedge groove width w.

5.3 Study of wedge design effect on cogging torque

The cogging torque in permanent-magnet machines with open slots results from the interaction between the stator teeth and the rotor permanent magnets which would naturally drive the rotor to the angular position where the total magnetic energy is maximum [3]. It is therefore intuitive that reducing the slot opening leads to a magnetically more uniform stator bore surface and then reduces cogging torque. This can be achieved with the proposed wedge design by suitably reducing the dimension w. Furthermore, another strategy to mitigate cogging torque effects is to design the stator so that the groove position with respect to the wedge center (fig.5.3b) is not the same for all the slots but is properly changed from the one slot to the other. The latter method is conceptually the same as designing the machine stator with non-uniformly distributed tooth widths as proposed in [3] but has the advantage of not requiring a stator core modification. The two design strategies (variation of w and variation of the groove position) are examined next.

5.3.1 Influence of the groove width

Reducing the groove width w has an effect which approximately resembles the reduction of the slot opening, with the difference that the wedge permeability is lower than tooth tip permeability. Fig.5.7 shows the torque waveform as a function of the rotor position which is moved across a slot pitch, for different values of w. It can be seen that the cogging torque amplitude noticeably increases as the width w grows. The same dependency is illustrated in fig.5.8 by means of a surface diagram.
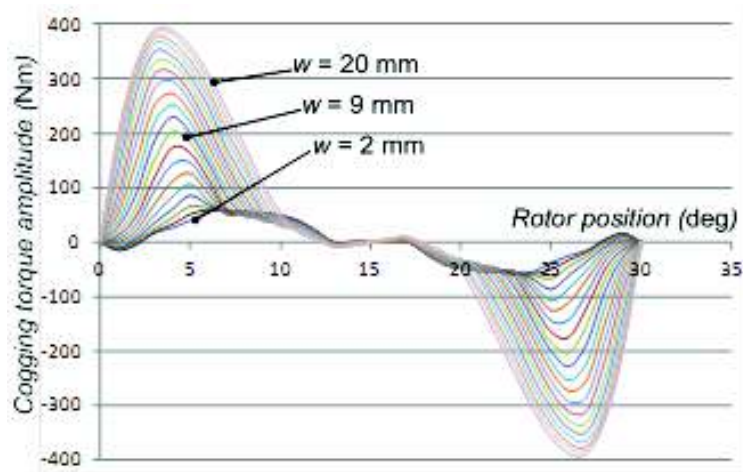
Figure 5.7: Cogging torque waveforms as functions of the rotor position for different wedge groove widths w.
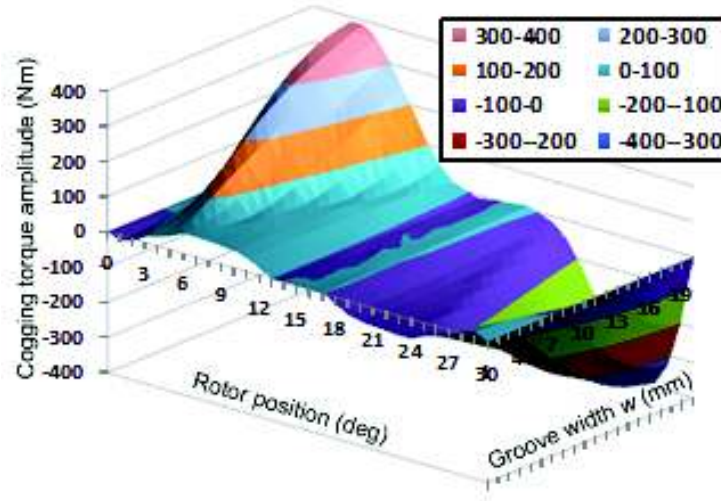
Figure 5.8: Surface diagram of the cogging torque versus the rotor position and the wedge groove width.

5.3.2 Influence of the groove position with respect to the wedge center

A further method for changing the cogging torque amplitude is to act on the groove position with respect to the wedge center. In this case, the groove width w is maintained the same for all the stator slots, but the groove position is changed as we move from one stator slot to the other. Using the nomenclature illustrated in fig.5.3b, the position of the groove can be identified by the distance Δ between the groove axis and the wedge axis, with positive or negative sign depending on whether the groove is shifted leftwards or rightwards. For the sake of commodity, it is convenient to express the distance Δ as a non-dimensional quantity which can vary between -1 and 1. This can be done by defining the non-dimensional distance

$$\delta = \frac{2\Delta}{W_b - w} \tag{5.3}$$

which equals zero when the groove is centered, -1 when the groove is completely shifted to the left ($\delta = -W_b/2 + w/2$) and 1 when the groove is completely shifted to the right ($\delta = Wb/2 - w/2$), as illustrated in fig.5.9. To highlight the impact of groove positions on the cogging torque three configurations are considered next. Each configuration is identified by the sequence of twelve rational numbers δ_i (such that $-1 \leq \delta_i \leq 1$), where i is an integer from 1 to 12 identifying the slot and δ_i defines the wedge groove

74

position as per (3). The three sequences δ_i taken into account are shown in Table5.2.

Slot ID	Values of δ_i		
(index i)	Central grooves	Random	$-1/+1/-1/\ldots$
1	0	-1	-1
2	0	-7/11	+1
3	0	+3/11	-1
4	0	-5/11	+1
5	0	+7/11	-1
6	0	-1/11	+1
7	0	-9/11	-1
8	0	+1/11	+1
9	0	+5/11	-1
10	0	+9/11	+1
11	0	+3/11	-1
12	0	+1	+1

Table 5.2: Groove position is stator slot wedges

The fist configuration is characterized by having all the twelve stator wedges designed in the same way with a centered groove ($\delta_i = 0 \, for \, any \, i$). The second configuration features a random distribution of groove positions over the twelve stator wedges as indicated in Table5.2.

The third configuration has the wedge grooves alternatively placed on one wedge end or the other, i.e. it alternates the two situations shown in fig.5.9a and fig.5.9b. The overall stator design for random groove positioning (second configuration is shown in fig.5.10).

The cogging torque waveforms computed by FE analysis for the three wedge groove positioning criteria are represented in fig.5.11. It can be seen that the configuration with centered grooves leads to the highest cogging torque amplitude. The cogging torque peak can be reduced by means of the random groove distribution and, even to a further extent, by resorting to the "$+1/-1$" alternate configuration.

5.4 Optimization problem implementation in the `Modefrontier®` environment

The optimization problem stated above is a single-objective problem with twelve constrained design variables. The single objective function is the cogging torque peak T_{peak} to be minimized. The constrained design variables are the twelve real numbers δ_i which are allowed to vary in the $[-1, 1]$
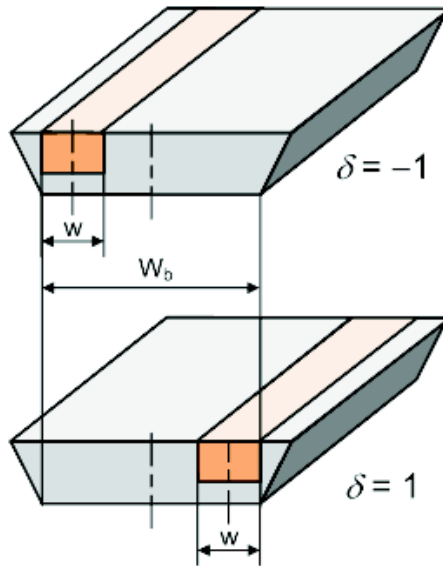
Figure 5.9: Extreme positions of the wedge groove and corresponding values of δ.
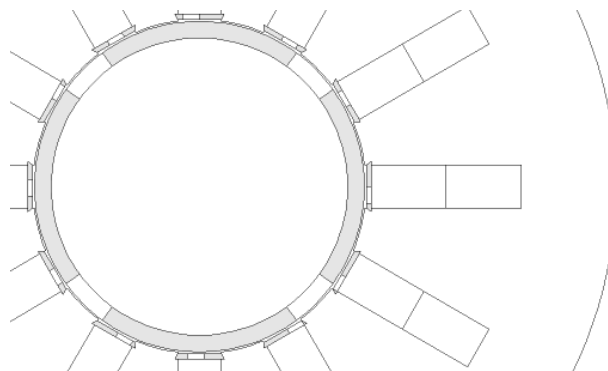
Figure 5.10: Machine cross-section for random groove positioning.
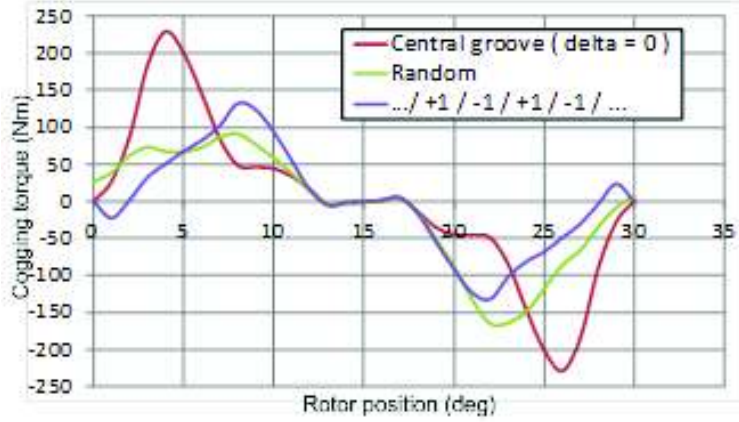
Figure 5.11: Cogging torque waveform as a function of the rotor position for different positioning criteria of wedge grooves.

interval. In mathematical terms the problem can be stated as follow:

$$\begin{cases} minimize\,(T_{peak}(delta_1, delta_2, \ldots, delta_{11}, delta_{12})) \\ \delta_k \epsilon [-1, 1]\ \forall k = 1, 2, \ldots, 11, 12 \end{cases} \tag{5.4}$$

The function T_{peak} which links the cogging torque amplitude to the twelve design variables δ_k could be expressed analytically by resorting to such algorithms as presented, for instance, in [6]. However, due to the well known inaccuracy in present analytical methods for cogging torque computation, it is find more reliable, although more time consuming, to implement the function $T_{peak}(\delta_1, \ldots, \delta_{12})$ numerically, that is by means of a sequence of finite-element analysis. The cogging torque calculation for any vector $\delta_1, \ldots, \delta_{12}$ of design variables is performed by means of a program written in LUA language which implements the flowchart drawn in fig.5.12 with black thin line. The program fist builds the machine model as shown in fig.5.3 by using the current vector $(\delta_1, \ldots, \delta_{12})$ of design variables to correctly place the wedge grooves. Then it performs a "for" loop by changing the rotor position by Δ_x-wide steps and, for the nth generic rotor position, it computes and stores the cogging torque value T_n. The computation is done by the FEMM software whose tasks can be executed through appropriate LUA language commands in batch mode [7]. When all the rotor positions across a 360-degree span have been analyzed, the program searches for the maximum in the vector $\|T_n\|$ of cogging torque amplitudes and sets T_{peak} equal to such maximum value. The objective function T_{peak} thus calculated is then fed into the optimizer which, based on genetic algorithms, will appropriately decide the following vector of design variables $(\delta_1, \ldots, \delta_{12})$ to be explored. The optimization process described has been implemented in the ModeFrontierÂ® environment [8] through the workflow diagram re-

77
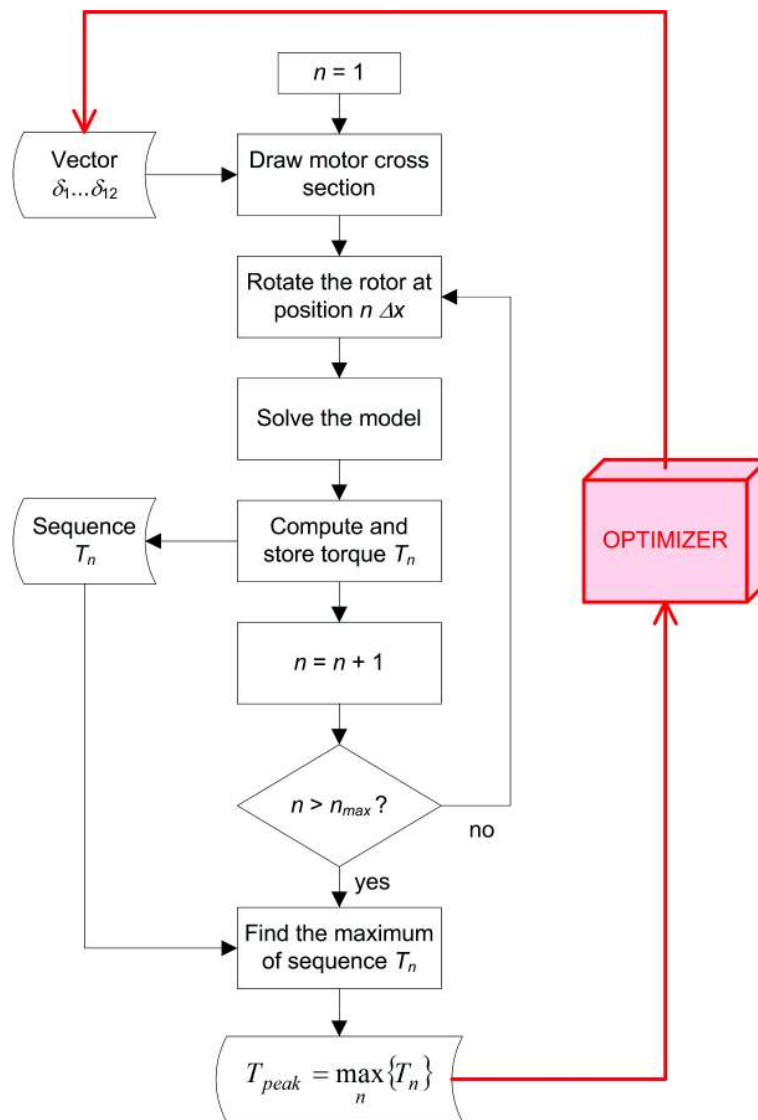
Figure 5.12: Flow chart for the numerical calculation of the cogging torque by finite-element analysis.

ported in fig.5.13. The workflow illustrates how the twelve input variables $\delta_1, \ldots, \delta_{12}$ are separately treated and, at any optimization step, transferred into the input file. The application node, at each iteration, launches the LUA program which performs the cogging torque computation through the flowchart shown in fig.5.12. The LUA program writes the results (cogging samples) in an output file and the cogging torque absolute peak in a further file which is intended to contain the number to be minimized. The overall optimization process employs the Simplex algorithm [8]. The initialization of the optimization process is performed by a DOE (Design of Experiments) section which used the Latin Hypercube mode to identify the initial designs to be explored which form the set from which the genetic algorithm search is started.
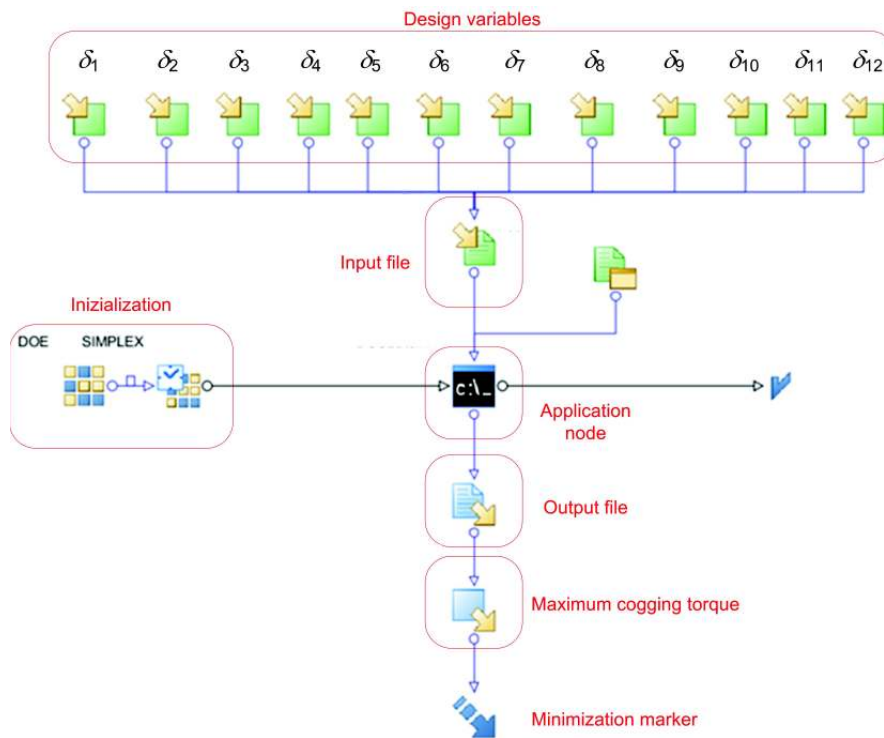
Figure 5.13: Workflow that implements the optmization in the modeFrontier environment.

5.5 Optimization Results

In the optimization process, more than one hundred configurations have been explored. Each configuration is simply called "*design*" and is assigned a progressive design **ID**. Each design is univocally determined by the order set of the twelve design variables $\delta_1, \ldots, \delta_{12}$.
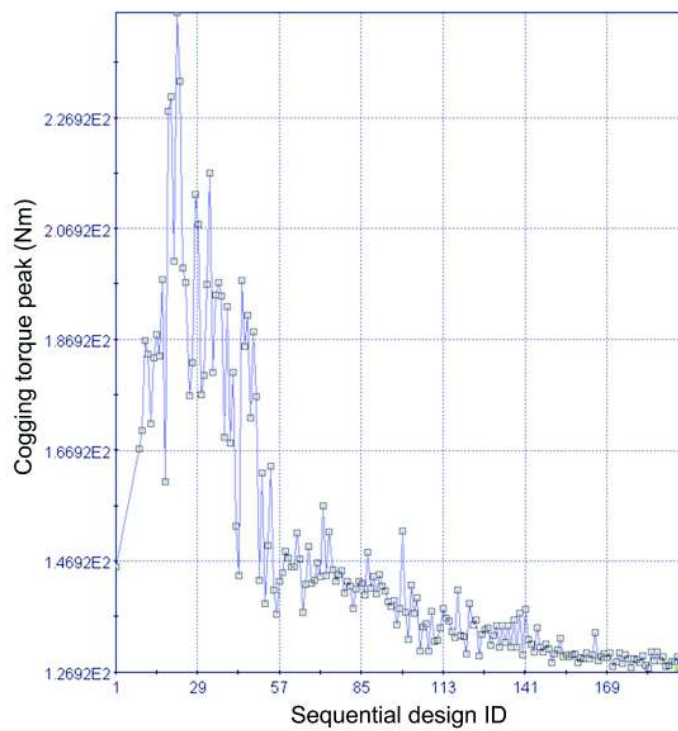
Figure 5.14: Peak torque values found throughout the optimization and plotted versus design **ID**

A first diagram which can be used to visualize the optimization process output is shown in fig.5.14. It represents the cogging torque amplitudes computed for all the explored design, ordered by design **ID**. It can be seen that, at the beginning (low design **ID** values) the amplitudes are relatively high and quite randomly distributed. As the optimization process continues (i.e. for increasing design **ID** values), the genetic algorithm tends to select only the "*fittest*" designs, whose cogging torque amplitude, in fact, tends to a value around $1.23 Nm$. This value can be treated as the lowest amplitude that can be achieved, provided that the optimization algorithm has worked properly identifying a global and not only local minimum for the given problem.
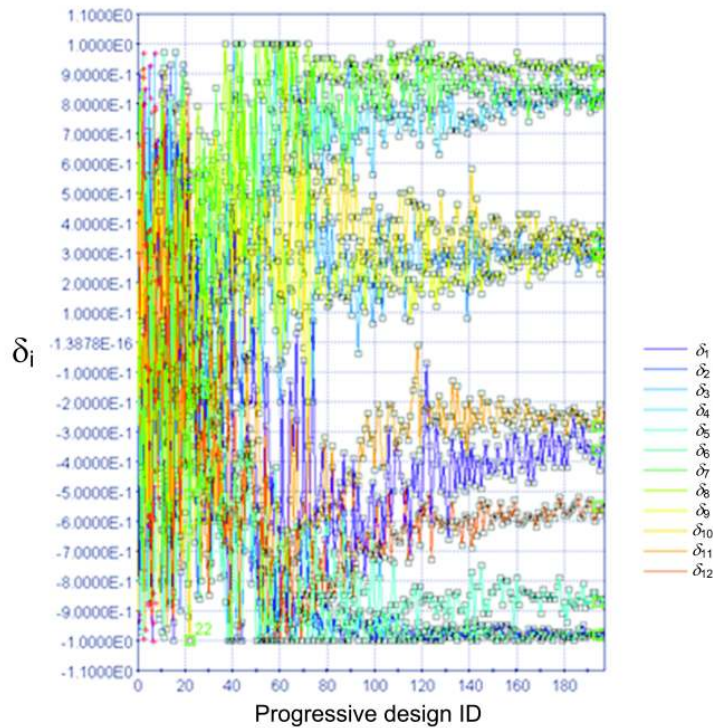
Figure 5.15: Trajectory of the twelve design variables throughout the optimization.

Another view of the optimization output is provided in fig.5.15, where we can see the values taken by all the design variables throughout the optimization. Representing all the design variable trajectories in the same diagram results in a quite confuse representation, so fig.5.17a-b shows the trajectory followed by each single design variable separately. The y-axis scale is between -1 and 1 for all the design variables, while the abscissa is the design **ID** in all cases. From fig.5.17 it can be clearly seen that each design variable,
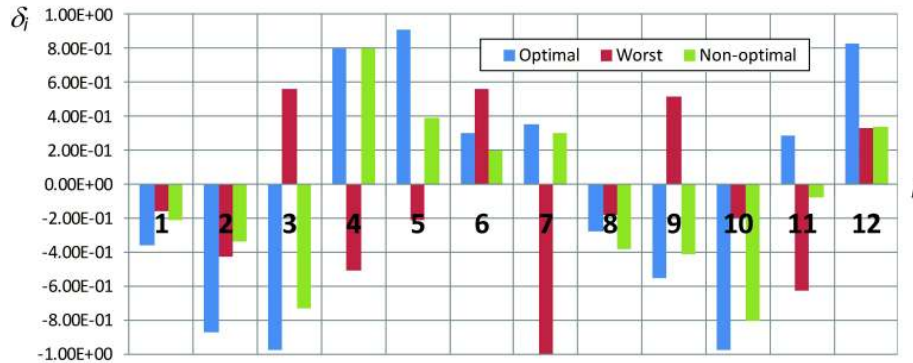
Figure 5.16: Numerical values of three design solutions: the optimal one, the worst one (among those been explored) and a generic non-optimal one.

after an initial wide fluctuation, tends toward a quite precise value which defines its optimal value.

The optimal solution is then constituted by the vector of variables δ_i indicated as "*optimal*" in the histogram in fig.5.16. For the sake of comparison, two more design solutions are considered in the same figure, i.e. the worst design (which gives the highest torque ripple amplitude found throughout the optimization) and a generic non-optimal solution.The cogging torque waveforms corresponding to the three designed mentioned above are reported in fig.5.19.

From a physical point of view, the optimal design determines a univocal distribution of groove positions around machine air-gap. Such distribution is illustrated in fig.5.17.

Such configuration is the one which can minimize the cogging torque. It may be interesting to note that, from fig.5.16 and fig.5.20 the optimal solution does not seem to be characterized by any particular recognizable pattern, which suggests that finding it without a optimization program would not be possible or, at least, intuitive.

Nevertheless, one can also observe from fig.5.19 one can see that the optimal solution leads to a surprisingly "*regular*" (i.e. periodic) cogging torque waveform, unlike non-optimal solutions.
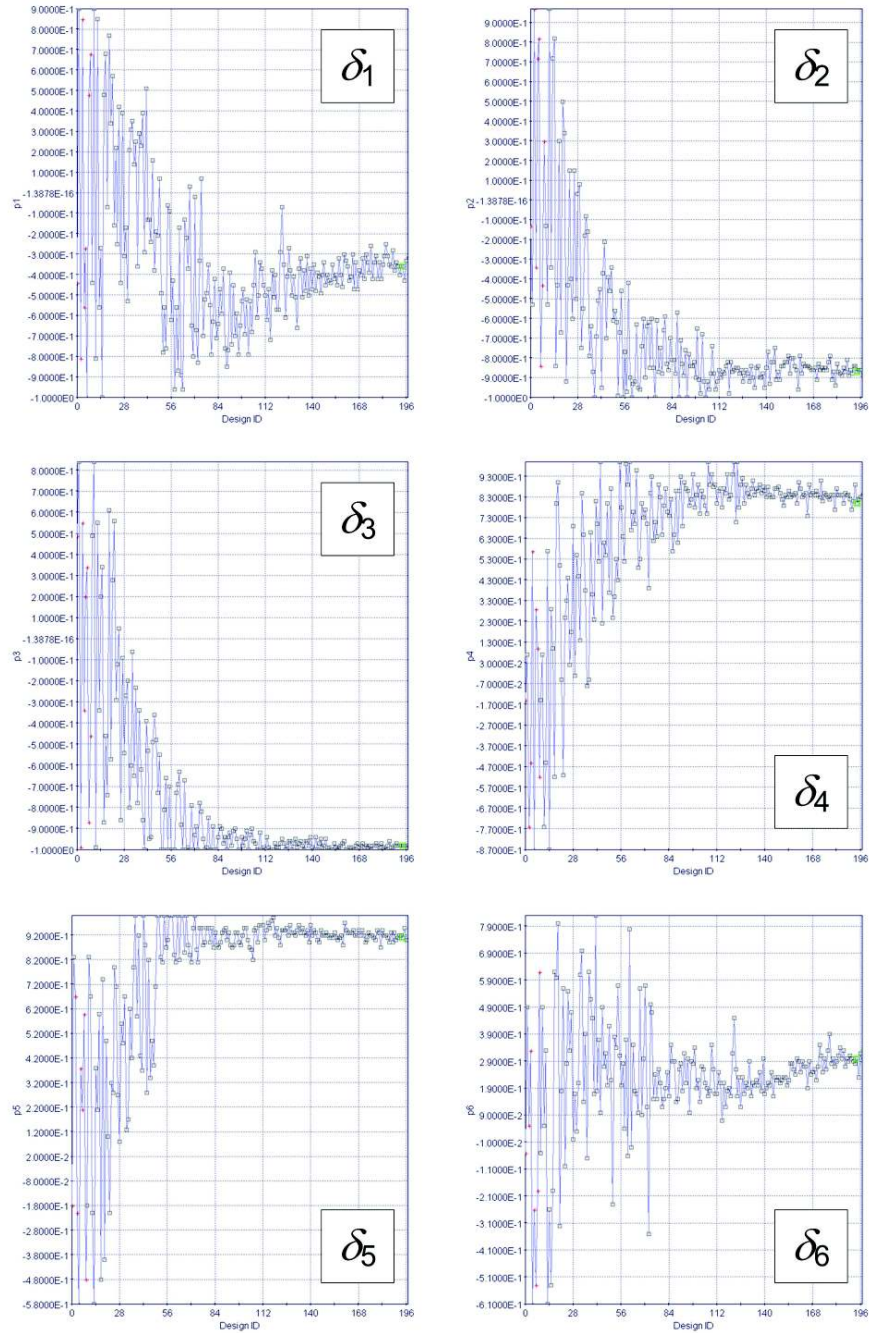
Figure 5.17: Trajectory of the first six design variables throughout the optimization.
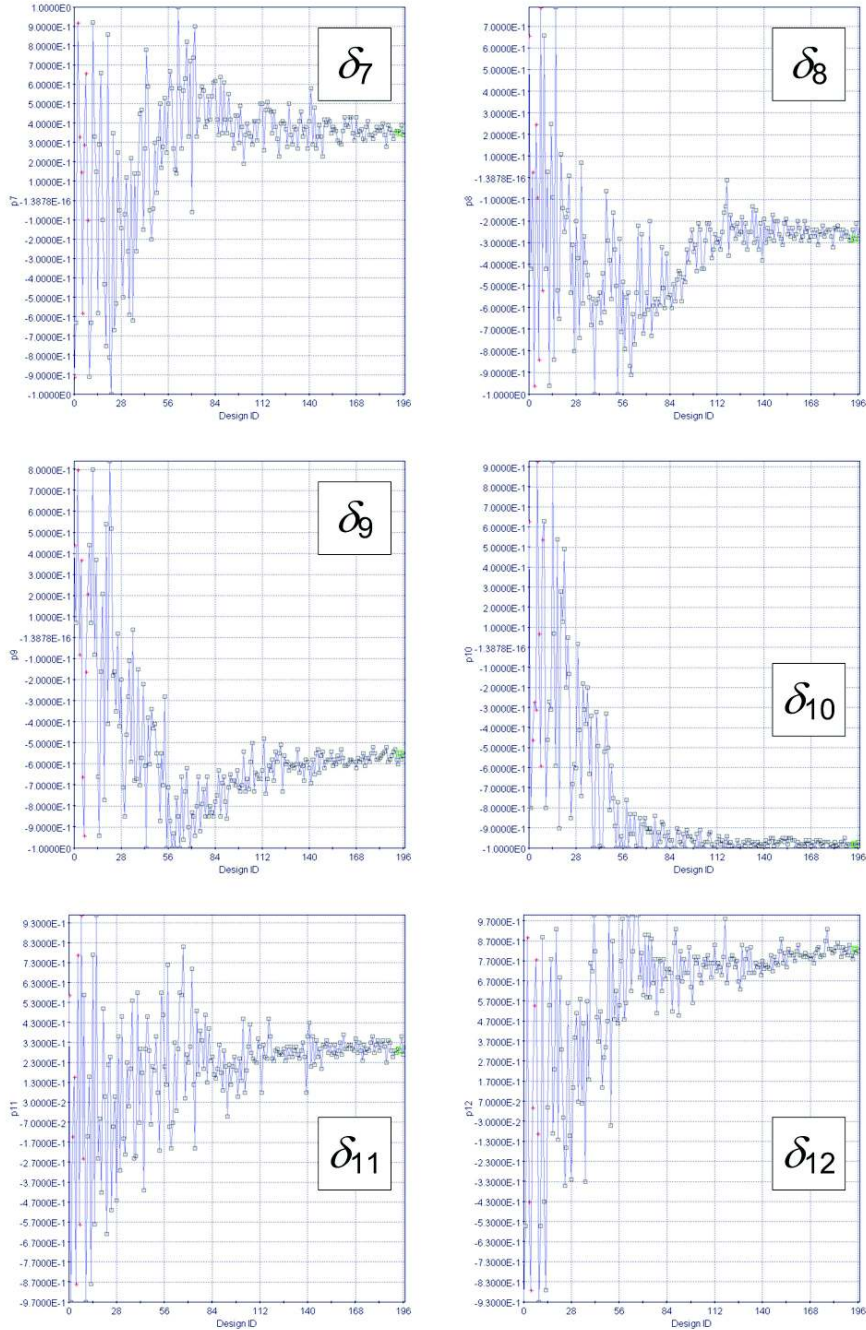
Figure 5.18: Trajectory of the last six design variables throughout the optimization.

84
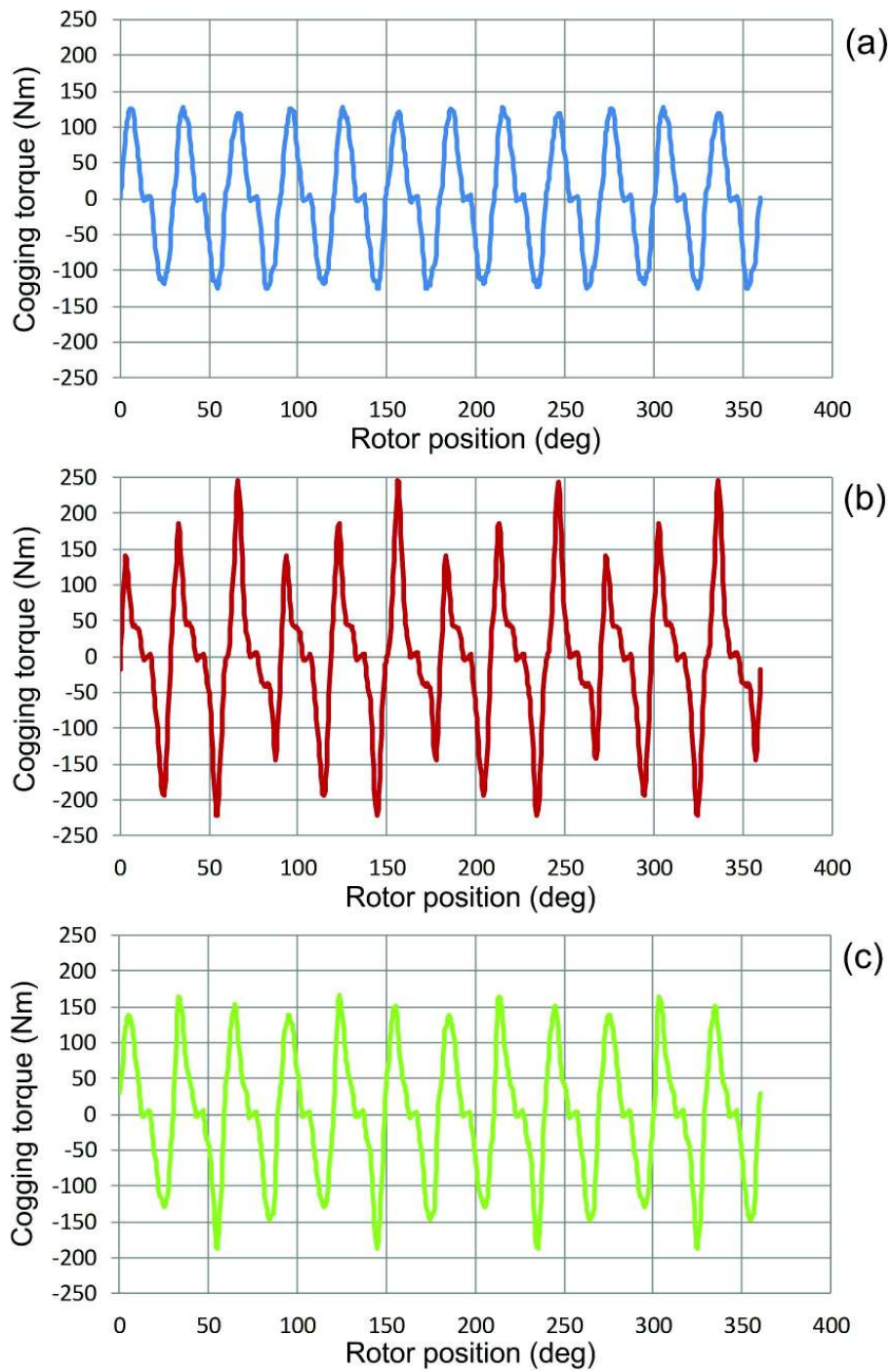
Figure 5.19: Cogging torque waveforms for: (a) optimal design; (b) worst design; (c) generic non-optimal design.
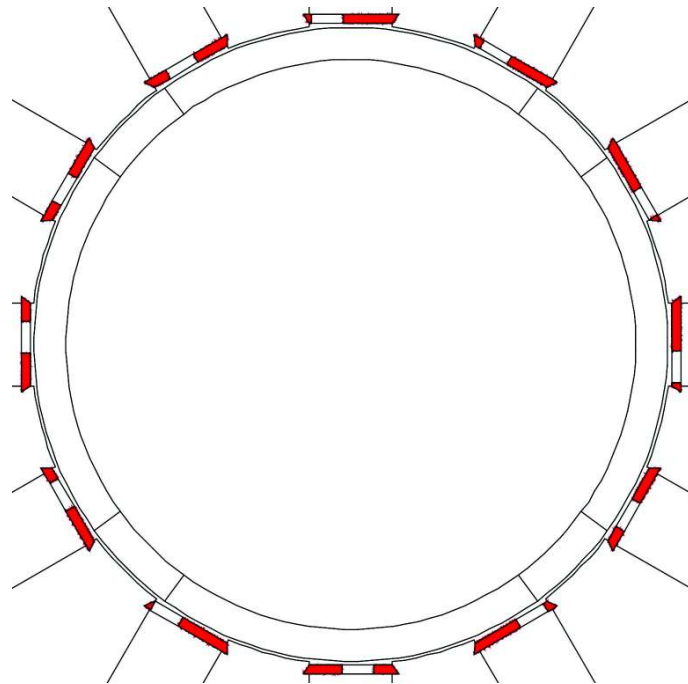
Figure 5.20: Optimal distribution of magnetic wedge grooves resulting from the optimization.

5.6 Conclusions

Cogging torque is a drawback of permanent-magnet machines with open slots. Magnetic wedges are widely used as a countermeasure, but while effective in reducing the cogging torque, they may lead to excessively high inductance value. This chapter proposes a special magnetic wedge design conceived for simultaneously control phase inductance and cogging torque in open-slot permanent-magnet motor design. The proposed wedge effectiveness has been investigated through some finite-element analysis simulations on a sample machine. It has been shown how acting on the proposed wedge geometry it is possible to strongly impact on both machine phase inductance and cogging torque amplitude.

Such wedge design has been considered in more detail with the specific aim of finding its optimal design, which minimized the cogging torque amplitude. For this purpose, a genetic optimization algorithm, available in the `ModeFrontier` software environment, has been employed. As a result of the optimization process, an optimal machine design with grooved wedges has been finally identified. Such optimal design does not exhibit any apparent feature such as to enable its recognition also without an optimization procedure. However, it has been also noted that the cogging torque wave-

form corresponding to the optimal design is not only the one with minimum amplitude, but also shows a periodic waveform which cannot be found, in general, in non-optimal design solutions.

5.7   References

[1] Y. Takeda, T. Yagisawa, A. Suyama, M. Yamamoto, *"Application of magnetic wedges to large motors"*, IEEE Transactions on Magnetics, vol. 20, no. 5, pp. 1780- 1782, Sep 1984.

[2] Di Napoli, O. Honorati, E. Santini, L. Solero, *"The use of soft magnetic materials for improving flux weakening capabilities of axial flux PM machines"*, IEEE Industry Applications Society Annual Meeting 2000, Oct. 2000, vol. 1, pp. 8-12.

[3] Daohan Wang, Xiuhe Wang, Dongwei Qiao, Ying Pei; Sang-Yong Jung, *"Reducing cogging torque in surface-mounted permanent-magnet motors by nonuniformly distributed teeth method"*, IEEE Transactions on Magnetics, vol.47, no.9, pp.2231-2239, Sept. 2011.

[4] F. Luise, A. Odorico, A. Tessarolo, *"Extending the speed-range of surface permanent-magnet axial-flux motors by flux-weakening characteristic modification"*, International Conference on Electric Machines, ICEM 2010, 6-9 Sept. 2010, Rome, Italy, CD-ROM paper RF-008893.

[5] A. Tessarolo, F. Luise, M. Mezzarobba, *"A new magnetic wedge design for enhancing the performance of open-slot electric machines"*, ESARS 2012.

[6] F. Luise, A. Calonico, *"Bietta magnetica per macchine elettriche rotanti"* (Magnetic wedge for rotating machines slots), International patent pending, P03894/PCT, March 2012.

[7] D. Zarko, D. Ban, T.A. Lipo, *"Analytical calculation of magnetic field distribution in the slotted air gap of a surface permanent-magnet motor using complex relative air-gap permeance"*, Magnetics, IEEE Transactions on , vol.42, no.7, pp. 1828- 1837, July 2006.

[8] D. Meeker, Finite Element Method Magnetics (FEMM): A Free Magnetic Finite Element Package for Windows [Online]. Available: http://www.femm.foster-miller.net.

[9] ESTECO, modeFrontier, www.esteco.it.

[10] A. J. Mitcham, G. Antonopoulos, J. J. A. Cullen, *"Favourable slot and pole number combinations for fault-tolerant PM machines"*, IEE

Proceedings - Electric Power Applications, vol.151, no.5, pp. 520- 525, 9 Sept. 2004.

[11] A. M. E. Refaie, T. M. Jahns, P. J. McCleer, J. W. McKeever, "*Experimental verification of optimal flux weakening in surface PM machines using concentrated windings*", IEEE Trans. on Industry Applications, vol. 42, no. 2, Mar./Apr. 2006, pp. 443-453.

[12] W. L. Soong, T. J. E. Miller, "*Field-weakening performance of brushless synchronous AC motor drives*", IEE Proceedings, Electric Power Applications, vol. 141, issue 6, Nov. 1994, pp. 331-340.

Part II

Chapter 6

On the Validity of the Harmonic Superposition Principle for Computing Rotor Eddy Current Losses in Permanent Magnet Machines

6.1 Introduction

Permanent magnet (PM) machines have been spreading in many applications over the last few decades, both as motors and generators [1]. An issue which arises in their design is constituted by the prediction of eddy current losses due to stator magnetomotive force (MMF) harmonics [2], [3]. The latter are particularly large in case of a fractional-slot stator winding design [2]-[4]. The practical importance of computing rotor eddy current losses is especially related to possible demagnetization issues that would occur if permanent magnet temperature exceeded some given limits. In the literature, various methods have been proposed to compute the losses under discussion [2], [3], [5], [6]. In all the approaches proposed, whether numerical or analytical, the harmonic superposition principle is applied for power computation. In fact, the computation procedure is the following: first the losses caused by each single MMF harmonics are calculated, then these contributions are summed up to obtain the total losses. This method would be rigorously correct if the eddy currents caused by different MMF harmonics had distinct frequency: under this hypothesis, the system could be actually regarded as excited by harmonic power sources having different frequencies and the total

power losses would result from the sum of the power losses due to the various power sources [8]. Different MMF harmonics in an electric machines, however, give rise to rotor eddy currents whose frequencies are not distinct, in general [2]. In particular, in a fractional-slot machine with $2p$ poles having a number q of slots per pole per phase less than one, pairs of MMF space harmonics can be recognized such that the sum of their harmonic order is $2p$ and which cause equal eddy current frequencies in the rotor [2], [7]. For these pairs of MMF harmonics, the superposition principle does not hold for rotor eddy current loss computation [8]. This chapter investigates if and to what an extent the harmonic superposition principle retains validity in presence of MMF harmonics giving equal rotor frequencies. The investigation is performed computing the power loss results obtained in two different ways, i.e. in a rigorous way and by the superposition principle. In both cases, losses are computed through the FE model proposed in [2], [3], where the stator is replaced by a cylindrical ferromagnetic annulus carrying a sinusoidal linear current density on its inner bore surface. The comparison is carried out for different kind of permanent magnet machines. The treatment starts (Section 6.2) considering the idealized case where surface-mounted permanent magnets constitute a uniform layer around a cylindrical rotor as supposed in [2], [6]. Next, real rotor designs, including surface-mounted and interior permanent magnet rotor topologies, are taken into account (Sections 6.3 and 6.4).

6.2 Eddy current loss calculation in the idealized model

The analytical expression of rotor eddy current losses in PM machines [6] as well as numerical calculation methods described in [2] assume an idealized "multilayer" machine model which, unrolled in a linear arrangement, looks as shown in fig.6.1. Each layer is characterized by its relevant magnetic per-
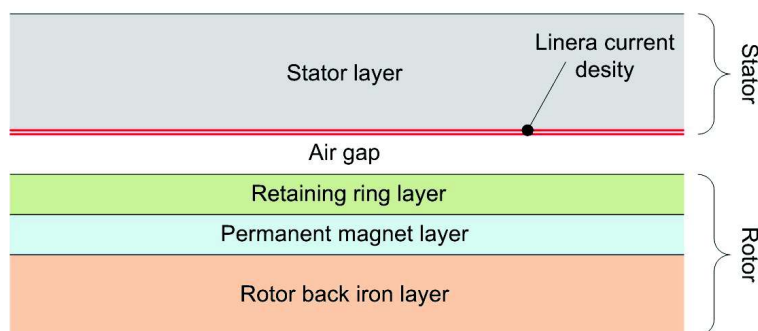
Figure 6.1: Multilayer machine model.

meability and electrical conductivity and the linear current density spread on the inner stator surface reproduces the effect of stator MMF harmonics in the stator reference frame. In the hypothesis of sinusoidal phase currents (absence of current time harmonics), the linear current density spread on the stator bore can be expressed as [6]:

$$\lambda(\theta, t) = \sum_{m=-\infty}^{+\infty} \Lambda_m \sin(p\omega_r t - m\theta + \theta_m) \tag{6.1}$$

where: θ is the spatial coordinate in mechanical radians along the air-gap, ω_r is the mechanical rotor speed, θ_m a suitable initial phase angle, p is the number of machine pole pairs, Λ_m is the mth order MMF harmonic amplitude, m the space harmonic order (equal to number of pole pairs of the mth space harmonic).

6.2.1   Theoretical approach

Reference [6] reports a complete analytical solution for the electric and magnetic fields in all points of the simplified model (fig.6.1) excited by the linear current density (6.1). This solution is very accurate as it accounts for the eddy current reaction. In particular, the expression of the current density in a generic rotor point having polar coordinates (r, θ) is:

$$j(\theta, r, t) = \sum_{m=-\infty}^{+infty} j_m(\theta, r, t) \tag{6.2}$$

where $j_m(\theta, r, t)$ is the current density distribution produced by the mth order MMF space harmonic in (6.1). The expression of $j_m(\theta, r, t)$ according to [6] is:

$$j_m(\theta, r, t) = \Lambda_m f_m(r) \sin[(p - m)\omega_r t - m\theta - \theta_m] \tag{6.3}$$

where $f_m(r)$ is a function of the radial coordinate r and of space harmonic order m, whose explicit expression can be find in [6]. From (6.3) it is clear that MMF harmonics of orders m and $2p - m$ produce rotor eddy currents with equal frequency, for any m. Let us now consider a generic rotor layer (fig.6.1) included between radii R_1 and R_2 and call ρ its resistivity. Let us compute the power losses produced in this layer respectively by the MMF harmonics of orders m and $2p - m$ order harmonics:

$$P_m = \int_{R_1}^{R_2} \int_0^{2\pi} \left[\rho j_m(\theta, r, t)^2\right] r d\theta dr \tag{6.4}$$

$$P_{2p-m} = \int_{R_1}^{R_2} \int_0^{2\pi} \left[\rho j_{2p-m}(\theta, r, t)^2\right] r d\theta dr \tag{6.5}$$

The power loss produced in the layer by both harmonics when they act together is:

$$P_{m,2p-m} = \int_{R_1}^{R_2} \int_0^{2\pi} \rho \left[j_m(\theta, r, t) + j_{2p-m}(\theta, r, t) \right]^2 r d\theta dr \qquad (6.6)$$

Substitution of (6.3) into (6.4) and (6.5) gives:

$$P_m = \pi \rho \Lambda_m^2 \int_{R_1}^{R_2} f_m(r)^2 r dr \qquad (6.7)$$

$$P_{2p-m} = \pi \rho \Lambda_{2p-m}^2 \int_{R_1}^{R_2} f_{2p-m}(r) r dr \qquad (6.8)$$

Substitution of (6.3) into (6.6) gives:

$$P_{m,2p-m} = P_m + P_{2p-m} + \int_{R_1}^{R_2} \int_0^{2\pi} 2\rho j_m(\theta, r, t) j_{2p-m}(\theta, r, t) r d\theta dr \qquad (6.9)$$

where the double integral in (6.9) is clearly equal to zero as one can verify by substitution of (6.3) into it. In conclusion, from the above theoretical derivation it is possible to write:

$$P_{m,2p-m} = P_m + P_{2p-m} \qquad (6.10)$$

which means that, for the two MMF harmonics of orders m and $2p - m$ the superposition principle holds even if they produce rotor eddy currents of equal frequency. Because the reasoning applies for whatever m, we can conclude that the harmonic superposition principle for rotor eddy current loss computation always holds if the idealized multilayer machine model (fig.6.1) is adopted.

6.2.2   Finite element numerical validation

The results obtained theoretically above are next checked numerically by FE analysis on an example fractional-slot machine, whose model is shown in fig.6.2a.

The stator is characterized by 10 poles and 12 slots and has the phases geometrically arranged according to the star of slots method [9]. Regardless of the rotor topology, the effect of stator MMF can be reproduced with a simplified slotless model (fig.??b) where the stator is replaced by a cylindrical ferromagnetic annulus having the same bore diameter as the actual stator [3] and bearing a surface current density (6.1). The current density (6.1) can be computed as per [7] and, in this particular instance, is characterized by the space harmonic spectrum given in fig.6.3. The effectiveness and accuracy of the simplified model is proven by the comparison (fig.6.4)
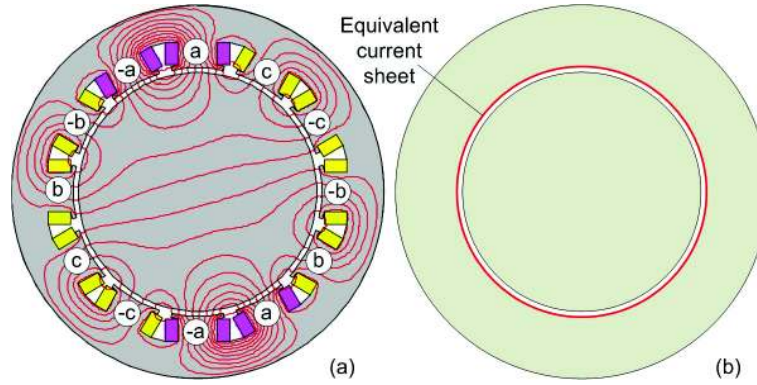
Figure 6.2: (a) Actual 10-pole 12-slot machine model; (b) simplified machine model.
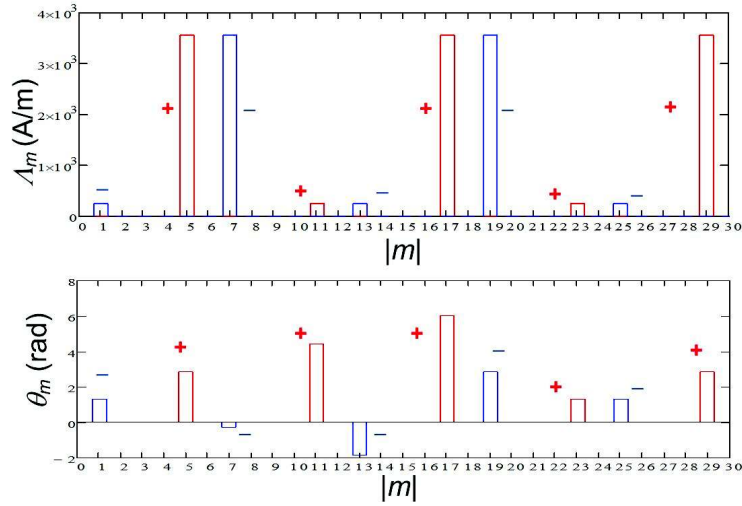
Figure 6.3: Equivalent current density spectrum. Signs "+" and "−" indicate whether m is positive or negative.

IDEALIZED MODEL DATA	
Stator outer diameter [mm]	150
Stator bore diameter [mm]	100
Air gap width [mm]	1
Permanent magnet height [mm]	4.8
Number of segments in Halbach-like configuration	32
Stator and rotor core relative magnetic permeability	50000
Permanent magnet relative magnetic permeability	1.05
Permanent magnet electrical conductivity [MS/m]	0.694

Table 6.1: Idealized model data

94
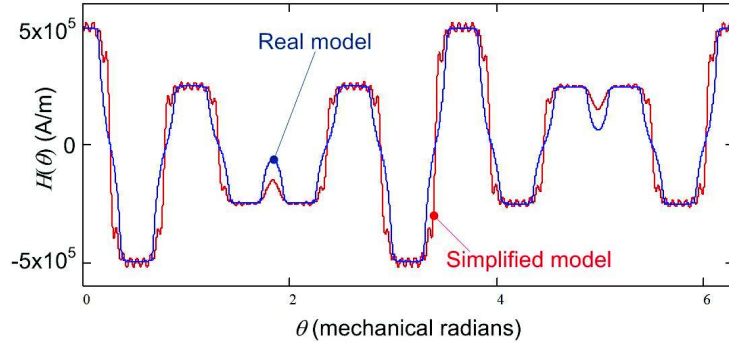
Figure 6.4: Air-gap fields obtained by FE analysis from the actual machine model and from the idealized multilayer model.
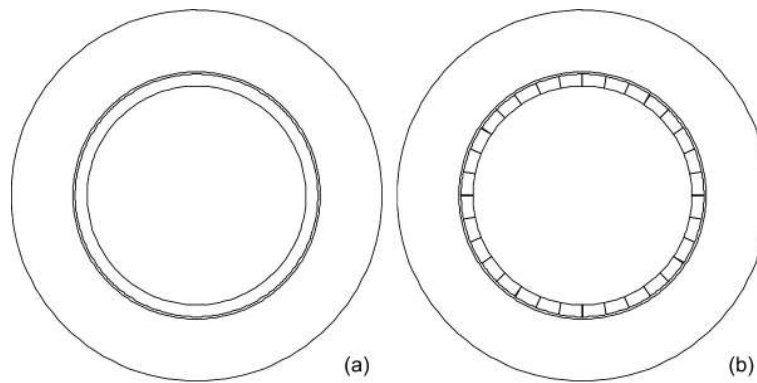
Figure 6.5: (a) Idealized rotor topology with continuous surface permanent magnet layer; (b) Rotor topology with segmented permanent magnet layer (Halbach-like design).

DATA FOR FE SIMULATIONS	
Mechanical speed, ω_r [rad/s]	62.8
Number of pole pairs, p	5
7th harmonic current density amplitude, Λ_7 [A/cm]	36
17th harmonic current density amplitude, $Lambda_{17}$ [A/cm]	36
Rotor eddy current frequency due to the 7th harmonic [Hz]	120
Rotor eddy current frequency due to the 17th harmonic [Hz]	120

Table 6.2: Data for FE simulation

95
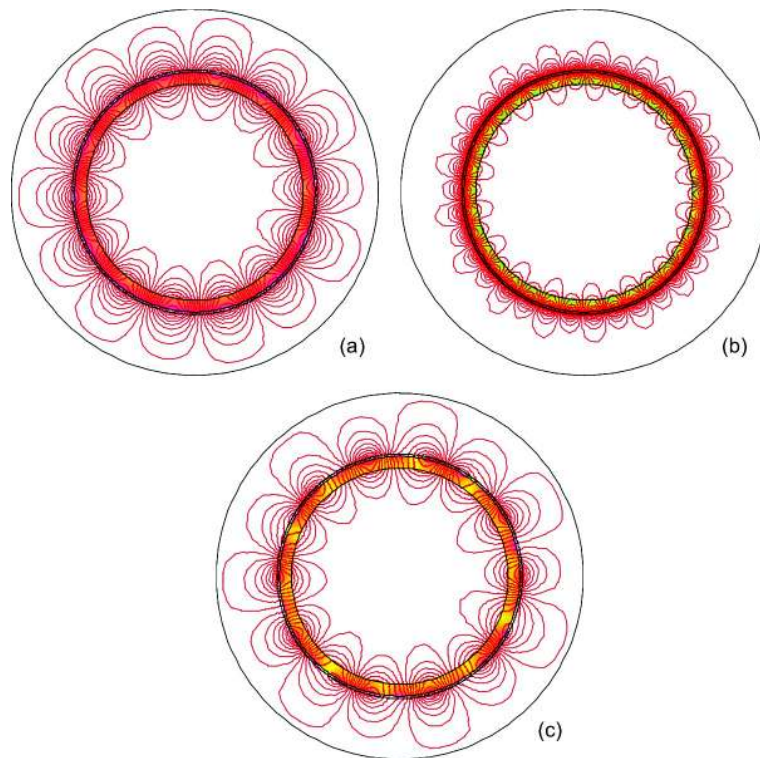
Figure 6.6: (a) Field produced by the 7th harmonic; (b) field produced by the 17th harmonic; (c) field produced by the 7th and the 17th harmonics acting together.

between the magnetic field profiles obtained by finite element (FE) analysis of the actual model and of the simplified model.

Looking at the current density spectrum shown in fig.6.3, one can see that harmonics can be grouped into pairs which produce the same rotor frequency. Each pair includes harmonics whose orders have $2p = 10$ as their sum. For example, pairs of such harmonics are those of orders $1 - 11$, $7 - 17$, $13 - 23$, *etc.* The aim of this Subsection is to check numerically if the superposition principle holds for these harmonic pairs in the case where the rotor is represented according to the idealized multilayer model (fig.6.1). For this purpose let us consider the rotor topologies shown in fig.6.5 and characterized by the data given in Table 6.1. Fig.6.5a strictly corresponds to the multilayer model shown in fig.6.1, while fig.6.5b features a segmented permanent-magnet layer. The structure depicted in fig.6.5b is the same as that of Halbach array rotors [10]. Among the different pairs of harmonics producing equal rotor eddy current frequency, the pair is taken for example constituted by harmonics of orders 7 and 17, which both give a rotor eddy current frequency of $120Hz$ according to (6.3). The data used for numerical simulations of the two models subjected to 7th and 17th harmonics are provided in Table 6.3. The FE analysis result for the idealized non-segmented model is shown in fig.6.6, where one case see the fields respectively produced by the 7th MMF harmonic alone, by the 17th MMF harmonic alone and by the two MMF harmonics acting together. Consistently with the notation used in the previous Subsection, the rotor power losses produced in the three mentioned cases will be called P_7, P_{17} and $P_{7,17}$ respectively.

The numerical computation results are illustrated by the histograms in fig.6.7. It can be seen that the sum of the losses produced by the single harmonics practically coincides with the losses produced by the two harmonics acting together. This means that the harmonic superposition principle holds for the power loss computation. This result applies to both the idealized case of continuous permanent-magnet layer and to the case of segmented (Halbach-like) layer.

6.3 Eddy current loss calculation in surface and interior permanent magnet machines

In this Section the focus is moved from the ideal case investigated in the previous Section to the real case of a Surface Permanent Magnet (SPM) and Interior Permanent Magnet (IPM) machines (fig.6.8). For this kinds of rotor topologies the theory developed in [6] does not hold and, therefore, the results derived in Section 6.2.1 of this chapter do not hold either. In other words, there is not any theoretical reason for supposing that the harmonic superposition principle can be applied for the calculation of rotor losses in these kind of machines. What is done next is to check for the superposition
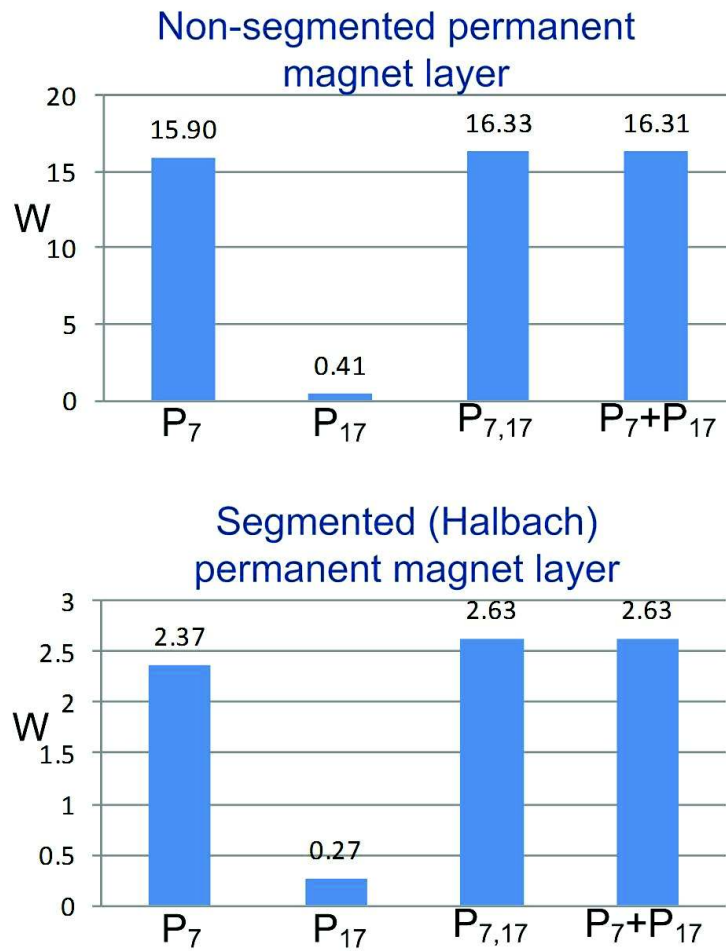
Figure 6.7: Rotor losses computed for the simplified model with cylindrical (segmented or non-segmented) permanent magnet layer.
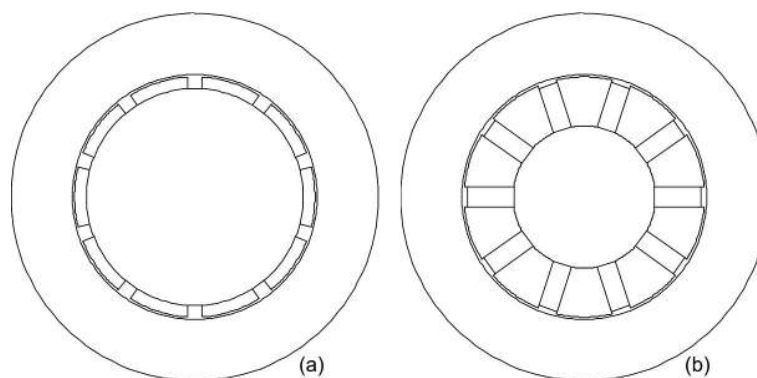
Figure 6.8: Machine model with: (a) SPM rotor; (b) IPM rotor.

principle validity numerically, i.e. using the loss computation method proposed in [3]. This method, in fact, approximates the stator MMF by means of the simplified cylindrical stator model carrying a linear current sheet on its inner bore (fig.6.2b), but can be correctly applied for any kind of rotor geometry [3].

SPM MACHINE GEOMETRY DATA	
Stator bore diameter [mm]	100
Core length [mm]	10
Permanent magnet coverage [%]	80
Permanent magnet height [mm]	4.8
Air gap width [mm]	1
Stator and rotor core relative magnetic permeability	5000
Permanent magnet relative magnetic permeability	1.05
Permanent magnet electrical conductivity [MS/m]	0.694

Table 6.3: SPM machine geometry data

IPM MACHINE GEOMETRY DATA	
Stator bore diameter [mm]	100
Core length [mm]	10
Permanent magnet width [mm]	10
Permanent magnet height [mm]	19
Air gap width [mm]	1
Stator and rotor core relative magnetic permeability	5000
Permanent magnet relative magnetic permeability	1.05
Permanent magnet electrical conductivity [MS/m]	0.694

Table 6.4: IPM machine geometry data

Again, in the computation the pair of harmonics of orders 7 and 17 is taken into account as an example. As in the previous Section, symbols P_7 and P_{17} are used to indicate the losses produced by the 7th harmonic alone and by the 17th harmonic alone, respectively. The symbol $P_{7,17}$ is used to indicate the losses produced by the 7th and 17th harmonics acting together.

The numerical computation results obtained by FE analysis are shown in fig.6.9. It can be seen that the identity $P_7 + P_{17} = P_{7,17}$ does not hold any more or, in other terms, the superposition principle is not strictly valid. The application of this principle leads to an error of about 6.7% in the SPM case and causes rotor losses to be overestimated. In the IPM case, the superposition principle leads to a larger error, equal to about 42% and causes rotor losses to be underestimated. The smaller error found in the SPM case is
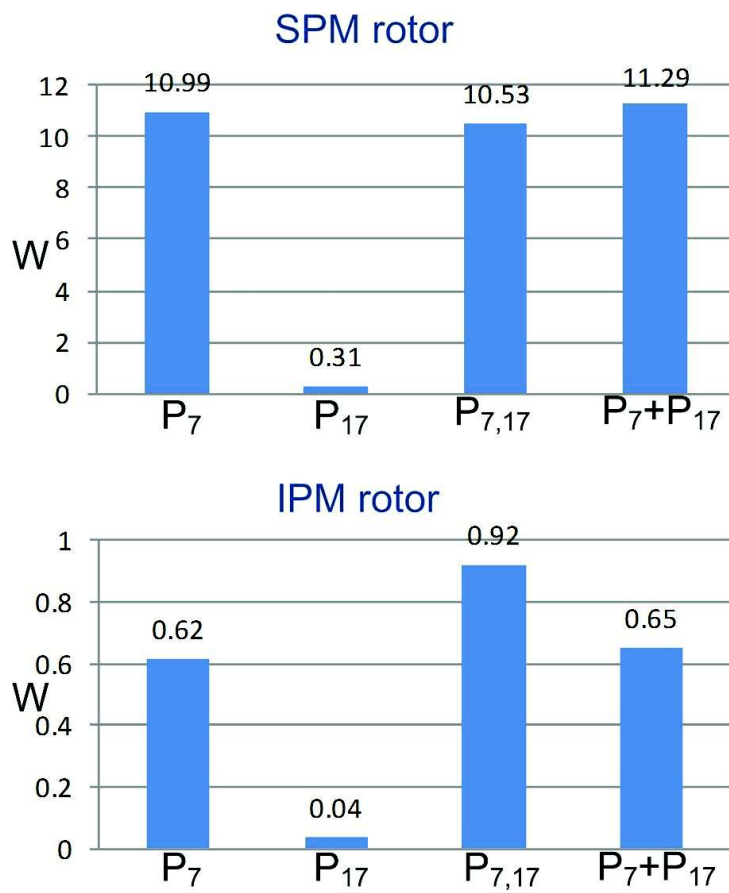
Figure 6.9: Computed rotor losses for the machine with SPM and IPM rotor.

easy to justify since this topology more closely resembles the idealized model (fig.6.5a), by which it differs only for the presence of inter-magnet regions. On the other side, the IPM topology is such that permanent magnet, buried in the rotor core, more strongly differ from the idealized geometry, which accounts for the larger error found in the IPM case.

6.4 Discussion

The treatment proposed in this chapter confirms that the harmonic superposition principle can be applied with theoretically and practically null errors for those rotor topologies where the permanent magnet region can be modeled as an either continuous or segmented cylindrical annulus (as it occurs for Halbach rotors, for instance). In presence of other rotor topologies, like SPM or IPM rotors, numerical examples have been given to show that the superposition principle does not hold. However, the information given in the chapter is not sufficient for the designer to decide a priori what would be the error that would result from applying the superposition principle also to SPM and IPM topologies. A way to solve the uncertainty is however quite straightforward. It simply consists of using a computation method which does not require the superposition principle to be applied. The strategy would be to consider stator MMF harmonics not individually but in pairs, such that each pair includes those harmonics which cause equal rotor eddy current frequency. The two MMF harmonics of each pair should be considered as simultaneously acting in the same simulation. The losses individually caused by all harmonic pairs can be then correctly summed up to find the total losses. An analytical approach to automatically group harmonics based on the rotor eddy current frequency they cause is proposed in [7].

6.5 Conclusions

Permanent magnet (PM) machines have been spreading over the last decades taking the place of induction and wound-field synchronous machines in many applications. A key issue in their design is the prediction of rotor eddy-current losses caused by stator MMF harmonics. Such losses are important as a possible cause of overtemperature and consequent demagnetization of permanent magnets. Most of the methods proposed in the literature for PM machine rotor eddy current calculation rely on the harmonic superposition principle, i.e. compute the losses individually caused by each stator MMF harmonics and then sum the results to find the total losses. In this chapter, the superposition principle validity has been critically investigated. It has been shown that it certainly holds for those rotor topologies where the permanent magnet region can be approximated as a continuous

or segmented cylindrical annulus (as it occurs in Halbach-array rotors, for example). Conversely, the superposition principle has been shown to hold neither for SPM machines (where an inter-magnet air regions exists) nor for IPM rotor topologies. To study SPM or IPM machines, then, a computation method should be adopted that does not rely on the superposition principle. This could be done by grouping MMF harmonics based on the rotor eddy current frequency they produce and computing the losses due to each group of harmonics with a single FE simulation.

6.6   References

[1] Wen Ouyang, D. Zarko, T. A. Lipo, "Permanent Magnet Machine Design Practice and Optimization", *Conference Record of the 2006 IEEE Industry Applications Conference*, vol.4, pp.1905-1911, 8-12 Oct. 2006.

[2] N. Bianchi, E. Fornasiero, "Impact of MMF space harmonic on rotor losses in fractional-slot permanent-magnet machines", *IEEE Trans. on Energy Conversion*, June 2009, vol. 24, issue 2, pp. 323-328.

[3] N. Bianchi, S. Bolognani, E. Fornasiero, "An overview of rotor losses determination in three-phase fractional-slot PM machines", *IEEE Transactions on Industry Applications*, vol. 46, no. 6, pp. 2338-2345, Nov.-Dec. 2010.

[4] A. M. El-Rafaie, "Fractional-slot concentrated-windings synchronous permanent magnet machines: opportunities and challanges", *IEEE Trans. on Industrial Electronics*, vol. 57, no. 1, Jan. 2010, pp. 107-121.

[5] Jiabin Wang; K. Atallah, R. Chin, W.M. Arshad, H. Lendenmann, "Rotor eddy-current loss in permanent-magnet brushless AC machines", *IEEE Transactions on Magnetics*, vol.46, no.7, pp.2701-2707, July 2010.

[6] Z. Q. Zhu, K. Ng, N. Schofield, D. Howe, "Improved analytical modelling of rotor eddy current loss in brushless machines equipped with surface-mounted permanent magnets", *IEE Proceedings, Electric Power Applications*, vol. 151, no. 6, 2004, pp. 641-650.

[7] A. Tessarolo, M. Mezzarobba, "On the computation of rotor losses through a set of harmonic finite-element analysis in fractional-slot concentrated-coil permanent-magnet machines", *International Conference on Computer as a Tool, IEEE Eurocon 2011*, Lisboa, Portugal, 27-29 April 2011, CD paper no. 581.

[8] E. J. Rothwell, M. J. Cloud, *Electromagnetics*, CRC Press, 2001, p. 45.

[9] N. Bianchi, M. Dai Pre, "Use of the star of slots in designing fractional-slot single-layer synchronous motors", *IEE Proceedings on Electric Power Applications*, May 2006, vol. 153, issue 3, pp. 459-466.

[10] Seok-Myeong Jang, Sang-Sub Jeong, Dong-Wan Ryu, Sang-Kyu Choi, "Design and analysis of high speed slotless PM machine with Halbach array", *IEEE Transactions on Magnetics*, vol.37, no.4, Jul 2001, pp.2827-2830.

Chapter 7

Use of Time-Harmonic FE Analysis to Compute Rotor Eddy-Current Losses in Synchronous Machines Subject to Distorted Stator Currents

7.1 Introduction

The evaluation of rotor eddy-current losses can be a crucial task in the electromagnetic design and verification of synchronous machines, both with traditional wound-rotor design [1] and with permanent-magnet [2]-[7] or reluctance [8] rotor topologies. Particular attention has being recently put on rotor eddy-current losses in permanent-magnet machines with fractional-slot windings [2], [3], [4]. In fact, such stator design gives rise to large air-gap field space harmonics, which rotate asynchronously with respect to the rotor and thus produce flux pulsations and eddy-current losses in permanent magnets, resulting in possible overheating and demagnetization issues.

The computation of rotor eddy-current losses becomes even more important when stator currents have a non-sinusoidal waveform (as typically happens if the machine is connected to power electronics equipment) because this leads to a worsened air-gap field distortion due to the presence of time harmonics [6], [8].

In general, the phenomena involved in rotor eddy-current generation are so complex to model that for their accurate evaluation a Time-Stepping Finite-Element Analysis (TSFEA) is employed, where rotor motion, stator

slotting and current distortion effects are naturally taken into account [7], [8], [9]. Though, TSFEA suffers from some remarkable drawbacks. Firstly, it requires long computation time; secondly, the power loss evaluation from TSFEA implies waiting for the TSFEA simulation to reach a steady-state condition and then computing the mean of power losses (which are generally time-variant) over a sufficiently long period of time after steady-state is reached. Such a post-processing task involves a certain subjective case-by-case judgment and is hard to implement into an automatic software algorithm.

For the aforementioned reasons, TSFEA method is unsuitable when the machine design needs to be processed through a genetic optimization algorithm and eddy-current loss calculation needs to be automatically repeated at each optimization step [11].

Analytical methods have been developed to solve the problem in much faster and flexible way [3]-[6], [10]. Actually, they have been used as a very effective strategy for qualitative evaluations [7] and for comparative analysis of different design solutions [3], [4], [10]. However, it has been pointed out that for some rotor topologies (e.g. in case of interior permanent magnets) analytical methods can lead to inaccurate results due to the simplifying hypotheses under which they have been derived [5].

The alternative proposed in this chapter for rotor eddy-current loss computation consists of using a limited set of time-harmonic finite-element analyses (THFEA) on a properly modified machine model. In each THFEA simulation, no motion is included and electromagnetic quantities (flux and current densities) are supposed to vary sinusoidally over time in any point. However, it will be shown how the appropriate definition of the modified machine model allows for both rotor motion and supply current distortion effects to be accounted for. The approach presented applies for any rotor geometry, any stator winding design and any current waveform, under the simplifying hypothesis that magnetic core saturation can be neglected.

To describe the proposed methodology, this chapter illustrates its application to the design optimization of a fractional-slot surface permanent magnet (SPM) concentrated-coil generator feeding a diode rectifier bridge, which causes remarkable phase current distortion. For accuracy assessment purposes, eddy-current loss values resulting from the proposed method are compared to those independently obtained by TSFEA. The comparison is repeated for several sample generator design configurations explored throughout the design optimization and in different operating conditions. The accordance found between the results thus obtained is deemed very satisfactory in all the cases considered. Furthermore, the proposed approach leads to a significant decrease of computational times and offers the advantage of easy integration into the design optimization environment.

7.2 Overview of rotor eddy-current computation

In this Section, the problem of computing eddy-current rotor losses in the design of an electric machine by means of a genetic optimization program [11] is addressed so as to justify the introduction of the new methodology. For illustrative purposes, reference is made to the practical design case of an SPM generator of which a briefly technical description is provided next.

7.2.1 Example machine description

The electric machine considered for application of the proposed eddy-current loss computation method is an SPM three-phase alternator with concentrated-coil winding conceived for electric power generation from sea wave. The machine is composed of N sectors, spanning $\lambda = 2\pi/N$ mechanical radians, each embracing six wound teeth and ten radially-magnetized permanent magnets (fig. 7.1). The stator sector is laminated as well as the rotor yoke, on which magnets are fixed. Each coil side in fig. 7.1 is marked with the name of the phase (u, v, w) to which it belongs and with its conventional current direction. The space between adjacent coil sides is not constituted by air as in usual concentrated winding design [2] but is filled with stator core laminations so as to make the heat transfer from stator copper more effective.

Some machine characteristic data, assumed as design constraints in the optimization, are provided in Tab.7.1.

MACHINE CHARACTERISTICS		
Peak torque	4×106	$kN \cdot m$
Peak speed	5	rpm
Stator outer diameter	9	m
Rated voltage	3.3	kV

Table 7.1: Machine characteristics

Since the alternator operates at strongly variable frequency depending on wave motion, the electric power produced needs to be processed through a power electronics dual-stage converter before being injected into a fixed-frequency grid. The alternator-side stage of the converter consists of a diode rectifier. Therefore the generator phase currents are assumed to have the typical waveform shown in fig.7.2, where T_c is the commutation interval, f the stator frequency, $\omega = 2\pi f$ the electric pulsation, $T = 1/f$ the period and I_{max} the converter DC-link current.

7.2.2 Practical reason for introducing THFEA approach for rotor eddy-current loss computation

The basic generator design described above is to be optimized by a dedicated multi-objective constrained optimization tool using genetic algorithms (`ModeFrontier`®) so as to determine the electromagnetic configuration capable of meeting performance requirements with the minimum production cost [11]. In particular, some of the quantities to be determined in the optimization are the number N and the dimensions of the sectors constituting the machine (fig.7.1). At each optimization step, eddy-current losses which originate in permanent-magnets need to be computed as a part of machine performance prediction.

An attempt is initially made to perform the computation by TSFEA. However, it is soon found that the approach is not viable because of the long computation time each simulation takes. Moreover, the loss value extraction from TSFEA implies some heuristic judgment in deciding when the simulation has reached a steady-state condition and in establishing the time interval over which the mean of eddy current losses has to be calculated. These issues make TSFEA simulations unsuitable for being integrated into the optimization environment, which requires a fully automated post-processing result extraction.
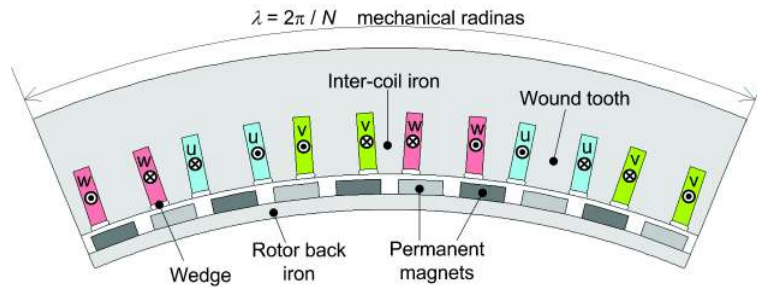
Figure 7.1: Cross-sectional model of one single machine sector.

The decision is thereby taken to work out a new method based on solving a set of THFEA simulations. THFEA, in fact, gives deterministic output results valid in steady-state conditions, takes short computation times and is simple to integrate into an automatic optimization process.

TSFEA simulations are not discarded, but used as a benchmark to assess the accuracy and reliability of eddy-current computations by THFEA methodology a posteriori [5], as it will be reported in Section 7.4.4.
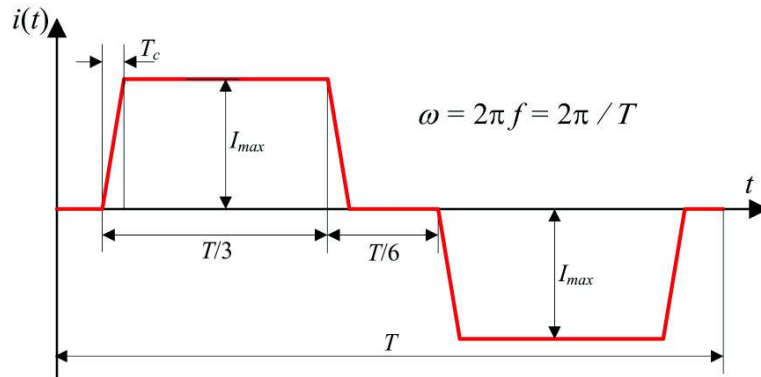
Figure 7.2: Phase current waveform.

7.3 Simplifying hypotheses

In order for the proposed methodology to be applicable, the simplifying hypothesis listed below have to be assumed:

A) magnetic saturation can be neglected, so that the superposition principle holds;

B) rotor eddy-currents do not significantly alter the flux density on the inner stator bore circumference; hence, on such circumference the flux density is assumed to be produced by stator currents only.

In addition to these problem-related assumptions, the more widely-assumed hypothesis is made of neglecting end-effects [4], so that a 2D machine modeling can be adopted. Therefore, throughout the chapter the vector potential obtained from field solutions will be always intended as its scalar component along the machine rotational axis.

7.4 Description of eddy-current loss computation procedure

When the machine is loaded with a balanced three-phase system of distorted currents (fig.7.2), various magnetic field space harmonics arise in the air-gap due to current time harmonics, to winding non-sinusoidal distribution and to slotting effects. Eddy currents (and consequent joule losses) are induced in rotor structures by all revolving harmonic fields except for those which rotate synchronous to the rotor. In the case of the machine under study, only eddy-current losses in permanent-magnets are of interest because the rotor yoke is constituted by laminations. However, the methodology presented would be the same in case of solid-steel rotor yoke.

7.4.1 Vector potential expression on the stator bore circumference

To illustrate how permanent-magnet eddy-current losses can be computed by means of THFEA simulations let us refer to fig.7.3. It represents the sketch of the machine cross-sectional model where an oriented contour Γ is introduced corresponding to the stator bore circumference. An angular coordinate x (in mechanical radians) is defined along Γ such that the point $x = 0$ lies on phase u magnetic symmetry axis. Let us suppose to energize phase u of the stator winding with unity current, while the other phases are at no load and permanent magnets demagnetized (fig.7.4a). A vector potential will then arise on circumference Γ. Its component along machine rotational axis will be called $A_u(x)$ (fig.7.4b) and its Fourier series coefficients will be called a_k (fig.7.4c):

$$A_u(x) = \sum_{k=1,3,5...} a_k \cos\left(\frac{2\pi}{\lambda}kx\right) \tag{7.1}$$

The function $A_u(x)$ (and then its Fourier coefficients a_k) can be easily found by a magnetostatic FEA.

Let us now suppose that the stator winding carries a balanced three-phase system of distorted phase currents $i_u(t)$, $i_v(t)$, $i_w(t)$ such that:

$$i_v(t) = i_u\left(t + \frac{2}{3}\pi\right), i_w(t) = i_u\left(t + \frac{4}{3}\pi\right) \tag{7.2}$$

The superposition principle (see Section 7.3) enables one to write the resulting vector potential on Γ as follows:

$$A(t, x) = i_u(t)A_u(x) + i_u\left(t + \frac{2}{3}\pi\right)A_u\left(x + \frac{1}{3}\lambda\right) + i_u\left(t + \frac{4}{3}\pi\right)A_u\left(x + \frac{2}{3}\lambda\right) \tag{7.3}$$

where the fact is used that the three phases are geometrically displaced by $\lambda/3$ mechanical radians apart (fig.7.1). If the phase current is distorted, it can be expressed in Fourier series as follows:

$$i_u(t) = \sum_{h=1,3,5...} I_h \cos\left(h\omega t - \psi_h\right) \tag{7.4}$$

For instance, in case of the waveform distortion shown in fig.7.2, I_h and ψ_h take the values below:

$$I_h = 4\frac{T}{T_c}I_{max}\frac{\sin(\pi h T_c/T)\cos(h\pi/6)}{\pi^2 h^2}, \psi_h = \frac{\pi}{2} \tag{7.5}$$

By substituting (7.1) and (7.4) into (7.3), after some algebraic manipulations we obtain the following equivalent expression for the vector potential:

$$A(t,x) = \frac{3}{2} \sum_{\substack{k+h= \\ 3,6,9\ldots}} a_k I_h \cos\left(h\omega t + kx - \psi_h\right) + \frac{3}{2} \sum_{\substack{|h-k|= \\ 0,3,6,9\ldots}} a_k I_h \cos\left(h\omega t - kx - \psi_h\right)$$

$$(7.6)$$

where the first sum is extended to all the pairs of odd integers (h,k) such that $h + k$ is a multiple of 3, while the second sum is extended to all the pairs of odd integers (h,k) such that $|h - k|$ is a multiple of 3.
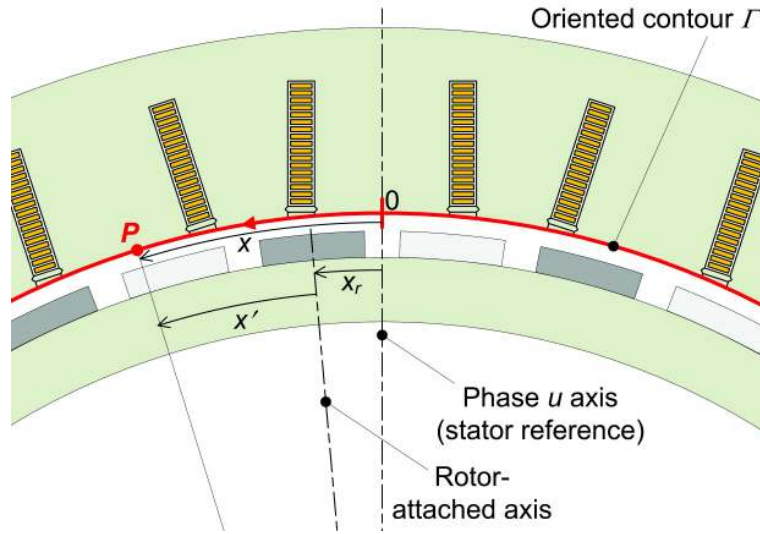
Figure 7.3: Machine model portion; stator- and rotor-attached axes introduced to identify the positions (x, x' respectively) of a generic point P on oriented contour Γ .

Adopting a complex notation for sinusoidally-varying quantities (complex numbers are indicated by overlined symbols), (7.6) can be rewritten in the complex form below:

$$\overline{A}(x,t) = \sum_{h,k} \left(\overline{C}_{h,k}^{+} e^{i(h\omega t + kx)} + \overline{C}_{h,k}^{-} e^{i(h\omega t - kx)} \right) \qquad (7.7)$$

where i represents the imaginary unit and

$$\overline{C}_{h,k}^{+} = \begin{cases} \frac{3}{2} a_k I_h e^{-i\psi_h} & if\, h+k \in \{3,6,9,12,\ldots\} \\ 0 & otherwise \end{cases} \qquad (7.8)$$

$$\overline{C}_{h,k}^{-} = \begin{cases} \frac{3}{2} a_k I_h e^{-i\psi_h} & if\, |h-k| \in \{0,3,6,9,12,\ldots\} \\ 0 & otherwise \end{cases} \qquad (7.9)$$

Equations (7.7)-(7.9) represent the vector potential produced, on contour Γ , by stator phase currents, including both current distortion effects

110
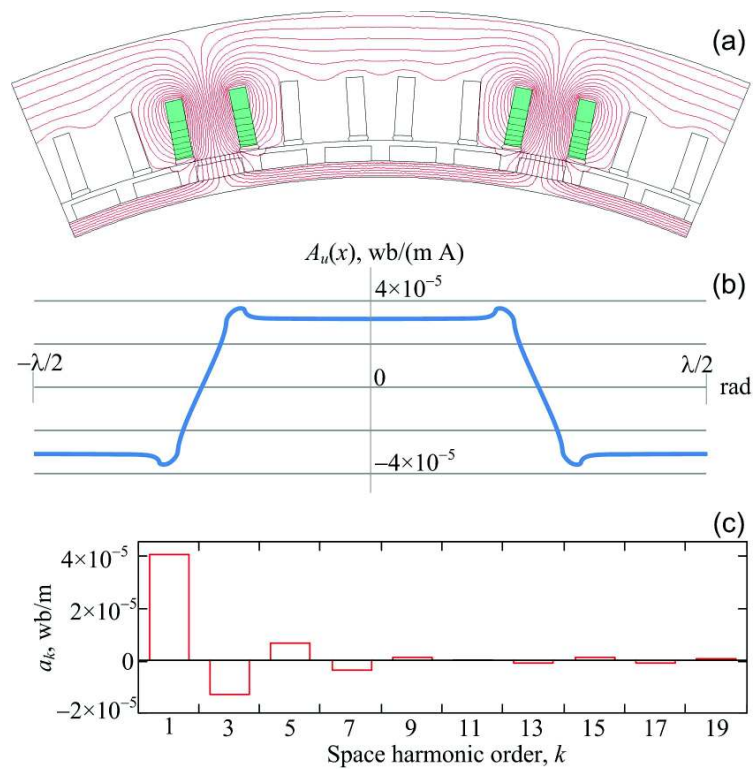
Figure 7.4: (a) Sector model with phase u energized; (b) vector potential $A_u(x)$; (c) its space harmonic spectrum of $A_u(x)$.

(through time harmonics I_h) and slotting effects (through space harmonic coefficients a_k). In order to be used in a TFFEA simulation (where the rotor is necessarily at stand-still), however, it is convenient to express (7.7) not in the stator but in the rotor reference frame. For this purpose, let us introduce a rotor-attached axis placed at position $x = x_r$ with respect to phase u axis (fig.7.3). Taking such rotor-attached axis as a new zero-reference for angular coordinates, a generic point P on contour Γ, placed at position x with respect to phase u axis, will be identified by a coordinate x' such that (fig.7.3):

$$x = x' + x_r \tag{7.10}$$

In steady-state conditions, the rotor revolves at an angular speed of ω/p mechanical radians per second, where $p = 5N$ is the number of pole pairs. Hence, (7.10) becomes:

$$x = x' + \frac{\omega}{p}t \tag{7.11}$$

Actually, (7.11) implies that for $t = 0$ the rotor axis is aligned with phase u symmetry axis, but this is not restrictive since the rotor-attached axis position can be arbitrarily chosen.

At this point, if we substitute (7.11) into (7.7), we obtain:

$$\overline{A}(x',t) = \sum_{h,k} \left\{ \overline{C}\,_{h,k}^{+}\, e^{i\left[\omega t\left(h+\frac{k}{p}\right)+kx'\right]} + \overline{C}\,_{h,k}^{-}\, e^{i\left[\omega t\left(h-\frac{k}{p}\right)-kx'\right]} \right\} \tag{7.12}$$

Equation (7.12) represents the vector potential distribution along contour Γ expressed in the rotor reference frame, i.e. seen from an ideal observer moving synchronous to the rotor. Theoretically, (7.12) expands the vector potential into an infinite number of harmonics. In practice, the number of harmonics which need to be considered in the sum to obtain a good approximation is small. For example, fig.7.5 shows the amplitudes of coefficients $\overline{C}\,_{h,k}^{+}$ and $\overline{C}\,_{h,k}^{-}$ when space harmonics a_k are those shown in fig.7.4 and time harmonics I_h are those obtained from (7.5) with $T/T_c = 48$ (see fig.7.2). It can be seen that only few pairs of odd integers h, k exist for which one of the corresponding coefficients $\overline{C}\,_{h,k}^{+}$ or $\overline{C}\,_{h,k}^{-}$ take non-negligible value.

7.4.2 Reduced model for field computation in air-gap and permanent-magnet region

Equation (7.12) can be used as the basis for launching a sequence of TFFEA simulations, each corresponding to an harmonic, i.e. to a (h, k) pair. For this purpose it is convenient to define a reduced geometric model for field computation in the air-gap and permanent-magnet region. The reduced model is shown in fig.7.6b.
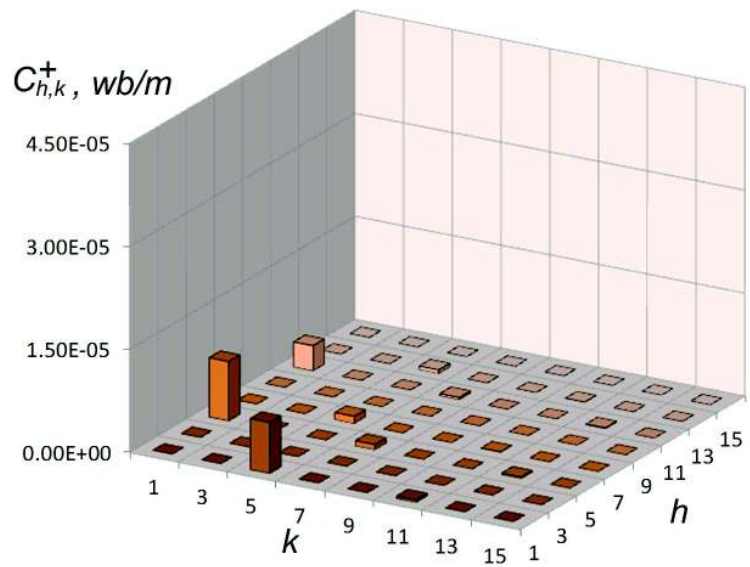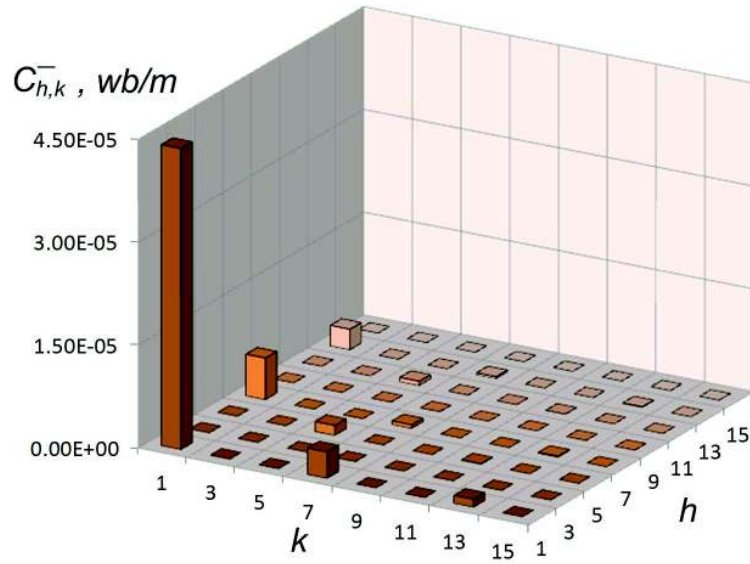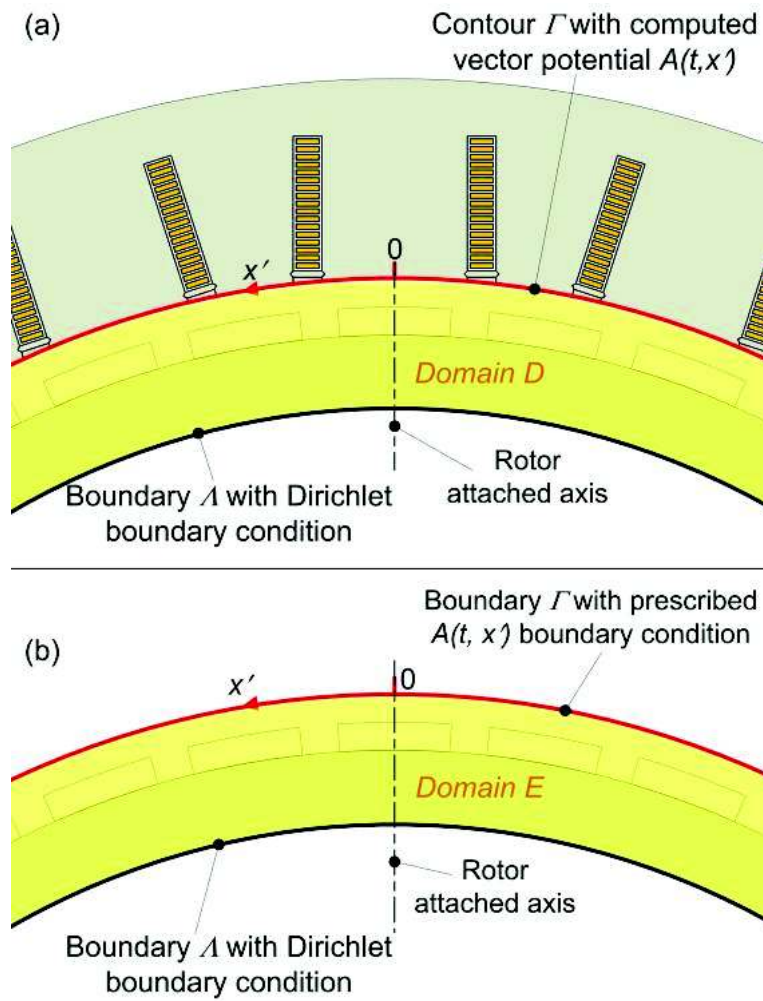
Figure 7.5: Amplitude of vector potential harmonics.

Figure 7.6: (a) Actual geometry with vector potential $A(t, x')$ computed on contour Γ and Dirichlet condition imposed on boundary Λ . (b) Reduced model with vector potential $A(t, x')$ imposed on boundary Γ and Dirichlet condition imposed on boundary Λ .

If we consider the complete machine cross-section (fig.7.6a), we can observe that the reduced model coincides with the domain D included between circular contours Γ and Λ (the latter being the inner rotor circumference). In the reduced model, the boundary condition on Γ is defined by imposing that the vector potential along it must be equal to (7.12), while the Dirichlet boundary condition is imposed on contour Λ . With these choices, we have that the domain D in the complete model (fig.7.6a) and the domain E in the reduced model (fig.7.6b) have the same internal structure (geometry, materials) and are characterized by the same boundary conditions. Hence, the same magnetic field solution is found in both domains. In other words, the reduced model is suitable for computing the field in the air-gap and permanent-magnet region of the machine. It is to be noticed that the above reasoning implies the assumption mentioned in 7.3.A. In fact, the expression (7.12) for the vector potential on Γ considers only the contribution of stator currents and disregards the effect of permanent-magnet eddy currents.
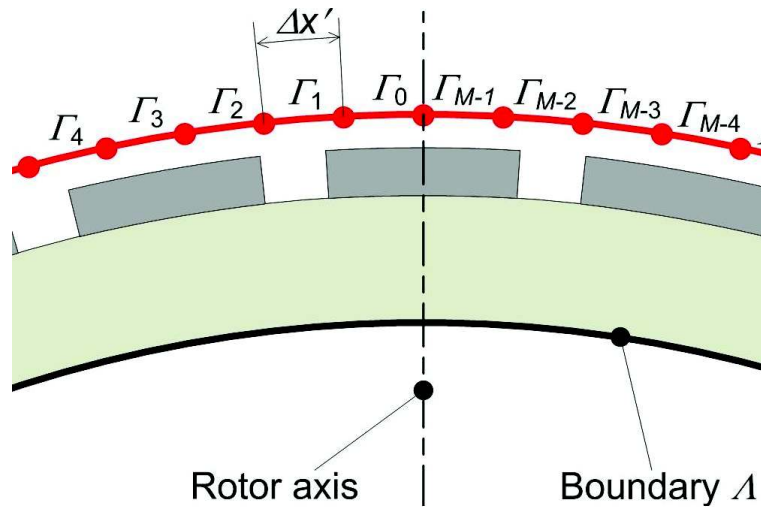
Figure 7.7: Reduced model with boundary Γ subdivided into equal small arcs of equal span $\Delta x'$.

7.4.3 Numerical implementation algorithm

Once the reduced model is defined, for practical implementation purposes it is convenient to subdivide the outer boundary Γ into M equal arcs Γ_1 , Γ_2 , ..., Γ_{M-1} , each spanning $\Delta x'$ mechanical radians (fig.7.7). The algorithm for permanent-magnet eddy-current loss computation is illustrated in fig.7.8. As illustrated in fig.7.8, all the pairs of odd integers (h,k) are sequentially explored, with $h = 1, 3, \ldots, h_{max}$ and $k = 1, 3, \ldots, k_{max}$ (h_{max} and k_{max} are respectively determined based on phase current and function $A_u(x)$ harmonic spectra, as per 7.4.1). For each pair, complex coefficients

$\overline{C}\,^{+}_{h,k}$ and $\overline{C}\,^{-}_{h,k}$ are computed through (7.8)-(7.9). If coefficient $\overline{C}\,^{+}_{h,k}$ takes a non-negligible value (see fig.7.5 5 for example), a harmonic simulation is run on the reduced model to obtain the loss contribution of the harmonic proportional to $\overline{C}\,^{+}_{h,k}$. For this purpose, boundary conditions (BC's) are to be assigned in the reduced model with subdivided boundary Γ (fig.7.7). To do this, the generic arc Γ_n [which is centered on $x' = (1/2 + n)\Delta x'$] is assigned a uniform vector potential phasor $\overline{A}\,^{+}_{n}$ whose value is obtained from (7.12) as:

$$\overline{A}\,^{+}_{n}= \overline{C}\,^{+}_{h,k}\, e^{ik\left(\frac{1}{2}+n\right)\Delta x'} \tag{7.13}$$

After assigning Dirichlet BC on boundary Λ (fig.7.7), a THFEA is run on the reduced model with a pulsation $\omega\,^{+}_{h,k}$ obtained from (7.12) as:

$$\omega\,^{+}_{h,k}= \omega \left(h + \frac{k}{p} \right) \tag{7.14}$$

As a simulation result, eddy-current losses are integrated over the permanent-magnet region to obtain the contribution $P\,^{+}_{h,k}$, due to the vector potential harmonic term proportional to $\overline{C}\,^{+}_{h,k}$ in the sum (7.12). The same procedure described so far for coefficients $\overline{C}\,^{+}_{h,k}$ conceptually applies to coefficients $\overline{C}\,^{-}_{h,k}$ having non-negligible values (see fig.7.5 for example). The difference is that, in this case, the reduced model BC on Γ is defined assigning the vector potential

$$\overline{A}\,^{-}_{n}= \overline{C}\,^{-}_{h,k}\, e^{ik\left(\frac{1}{2}+n\right)\Delta x'} \tag{7.15}$$

to the nth arc Γ_n and the TFFEA simulation is run at a pulsation

$$\omega\,^{-}_{h,k}= \omega \left(h - \frac{k}{p} \right) \tag{7.16}$$

As a simulation result, the permanent-magnet losses $P\,^{-}_{h,k}$ due to the vector potential term proportional to $\overline{C}\,^{-}_{h,k}$ in sum (12) are thus obtained. Once power loss contributions $P\,^{+}_{h,k}$, $P\,^{-}_{h,k}$ are obtained for all pairs (h,k) giving non-negligible coefficients in (7.12), the total eddy-current losses P_{pm} are computed by simply summing them:

$$P_{pm} = \sum_{h,k} P\,^{+}_{h,k} + P\,^{-}_{h,k}) \tag{7.17}$$

7.4.4   Numerical results and their validation against TSFEA

In order to assess the accuracy of the method described above, a comparison in made between the permanent-magnet eddy-current losses independently
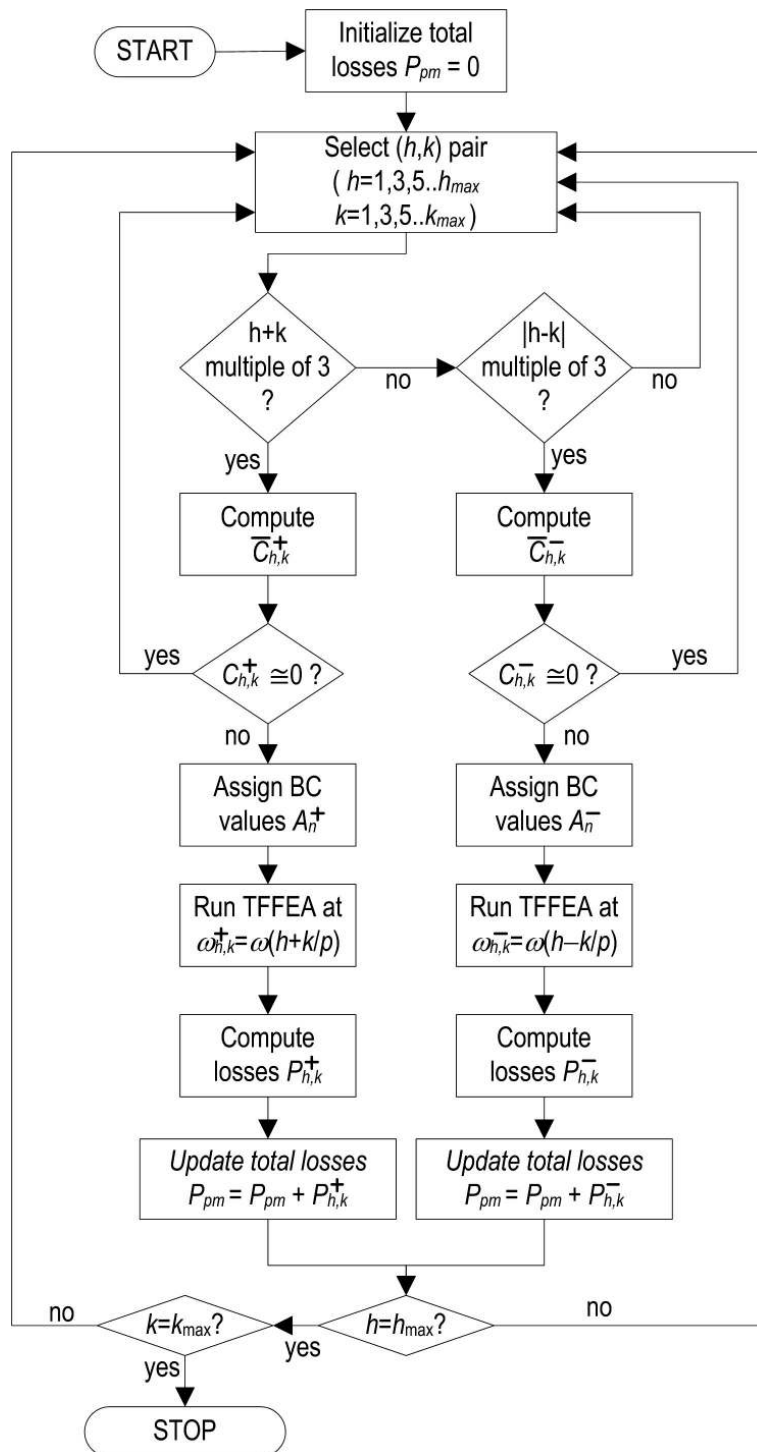
116

Figure 7.8: Flowchart for permanent-magnet loss computation through TF-FEA.

obtained from THFEA and TSFEA in sample machine configurations and operating conditions. Comparison results reported here refer to the machine design characterized by the sector configuration shown in fig.7.9 and by the data given in Table 7.2. As concerns the operating conditions, three working points are considered for comparison, i.e.:

A) no load operation;

B) working point at 3 rpm and 183.5 A per conductor;

C) working point at 1 rpm and 191.5 A per conductor.

SAMPLE MACHINE CHARACTERISTICS			
Number of sectors (N)	36	Number of stator slots	432
Sector spam (λ)	10°	Number of poles	360
Number of stator coils	216	Rated frequency [Hz]	9

Table 7.2: Sample machine characteristics
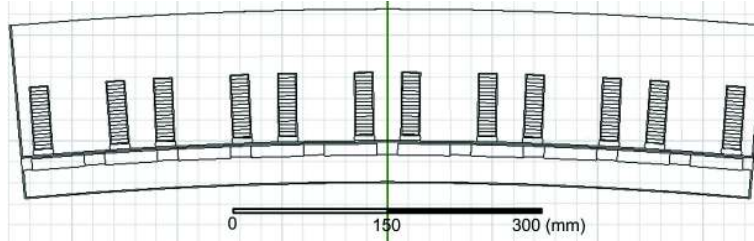
Figure 7.9: Sample machine section.

As an example, the eddy-current losses calculated by the proposed THFEA method are visually represented by the histograms in fig.7.10. It can be seen that the vast majority of the losses results from the interaction between the 5th space harmonic and the 1st time harmonic, i.e. from coefficients I_1 and a_5. Much smaller contributions are due to the h, k pairs $(1, 11)$ and $(1, 7)$. This feature characterizes not only the design configuration considered here for example (fig.7.9), but is found also in the other design solutions explored by the optimization process. In other terms, in the sum (7.17) the terms which have a non-negligible weight are very few and confined in a very small range of (h, k) pair combinations. This allows to remarkably limit the number of THFEA simulations to be launched at each optimization step to obtain an accurate loss estimation. In the particular application reported here, 10 THFEA simulations are launched at each optimization step, taking an overall computation time of about four minutes. Eddy-current computation is performed on the same machine and in the same working points listed

118

Figure 7.10: . Eddy-current loss harmonic contributions computed by THFEA for the working point at $3rpm$ and $183.5A$ per conductor.
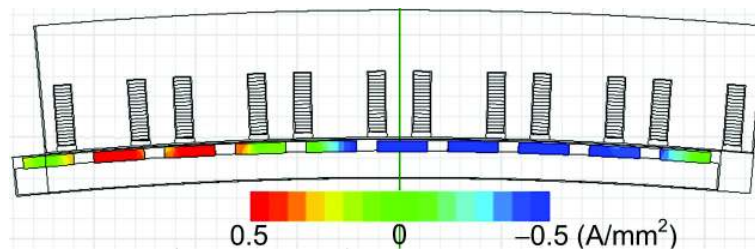
Figure 7.11: Snapshot from TSFEA of machine operation at $3rpm$ and $183.5A$ per conductor. Eddy currents in permanent magnets are represented.

119

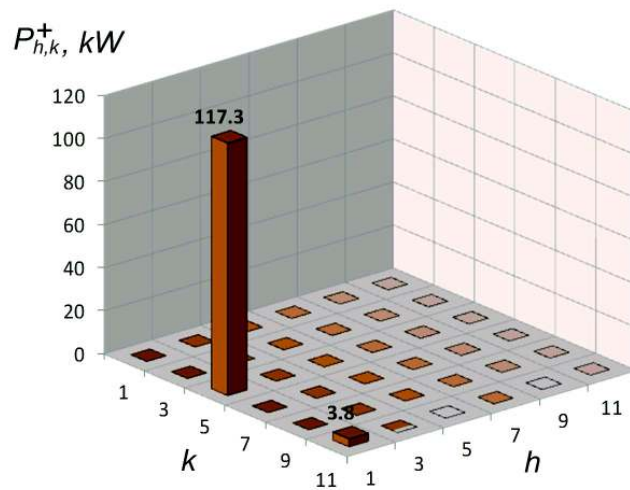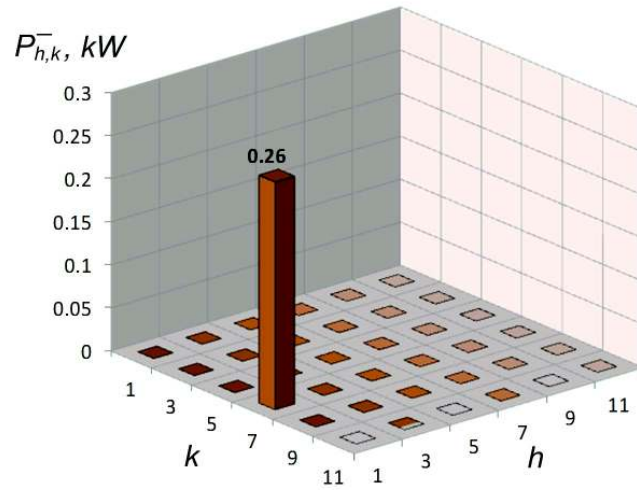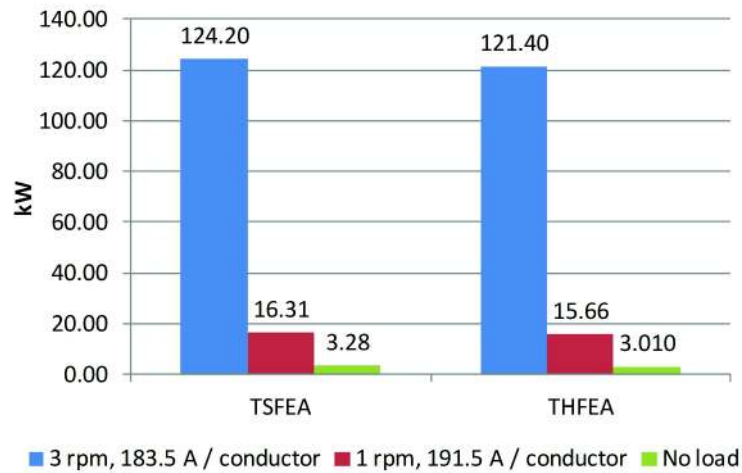Figure 7.12: Comparison between permanent-magnet eddy-current losses independently obtained by TSFEA and THFEA for three different operating conditions.

above by means of TSFEA, too (fig.7.11). A comparison between loss values obtained in the two ways is given in fig.7.12, which shows that a satisfactory accordance is achieved.

7.5   Conclusions

Rotor eddy-current losses are an important quantity to evaluate when designing a Surface Permanent Magnet machine as they can produce possible magnet overheating and demagnetization. The task becomes even more important in presence of a fractional-slot stator winding and of distorted phase currents due to the large air-gap flux-density harmonics which arise in this case. Due to the complex phenomena involved in eddy-current loss generation, their accurate computation normally requires Time-Stepping Finite Element Analysis (TSFEA). This approach, however, is computationally very heavy and require quite heuristic post-processing operations for result extraction. It is then little suitable when the machine designed is to be defined or refined through automatic optimization programs. In this chapter, an alternative approach has been presented, in which rotor eddy-current losses are computed through a set of Time Harmonic Finite-Element Analysis (THFEA) simulations. It has been shown how phase current distortion, stator slotting and rotor motion effects can be accurately accounted for through suitable analytical artifices. The proposed procedure can be easily implemented in a software algorithm which outputs eddy-current loss value in a fully automated and deterministic way. This makes the proce-

dure particularly suitable for integration into automatic design optimization loops. As an example, the procedure application has been presented to a SPM fractional-slot generator design optimization. In this application, running 10 THFEA simulations (with a time consumption of about 4 minutes) has been found sufficient to accurately computing eddy-current losses at each optimization step. The accuracy of the proposed procedure for rotor eddy-current losses has been validated by comparison with TSFEA results. Comparisons have been made for different machine design configurations and in different operating conditions, always showing a satisfactory agreement between the eddy current computed by TSFEA and with the proposed method.

7.6 References

[1] G. Traxler-Samek, T. Lugand, A. Schwery, "Additional Losses in the Damper Winding of Large Hydrogenerators at Open-Circuit and Load Conditions", *IEEE Trans. on Industrial Electronics*, vol. 57, No. 1, Jan. 2010.

[2] A. M. El-Rafaie, "Fractional-slot concentrated-windings synchronous permanent magnet machines: opportunities and challanges", *IEEE Trans. on Industrial Electronics*, vol. 57, no. 1, Jan. 2010, pp. 107-121.

[3] N. Bianchi, E. Fornasiero, "Impact of MMF space harmonic on rotor losses in fractional-slot permanent-magnet machines", *IEEE Trans. on Energy Conversion*, June 2009, vol. 24, issue 2, pp. 323-328.

[4] N. Bianchi, S. Bolognani, E. Fornasiero, "An overview of rotor losses determination in three-phase fractional-slot PM machines", *IEEE Transactions on Industry Applications*, vol. 46, no. 6, pp. 2338-2345, Nov.-Dec. 2010.

[5] Jiabin Wang; K. Atallah, R. Chin, W.M. Arshad, H. Lendenmann, "Rotor eddy-current loss in permanent-magnet brushless AC machines", *IEEE Transactions on Magnetics*, vol.46, no.7, pp.2701-2707, July 2010.

[6] Z. Q. Zhu, K. Ng, N. Schofield, D. Howe, "Improved analytical modelling of rotor eddy current loss in brushless machines equipped with surface-mounted permanent magnets", *IEE Proceedings, Electric Power Applications*, vol. 151, no. 6, 2004, pp. 641-650.

[7] Seok-Hee Han, T.M. Jahns, Z.Q. Zhu, "Analysis of rotor core eddy-current losses in interior permanent-magnet synchronous machines",

IEEE Transactions on Industry Applications, vol. 46, no. 1, pp. 196-205, Jan.-Feb. 2010.

[8] Jae-Do Park, C. Kalev, H.F. Hofmann, "Analysis and reduction of time harmonic rotor loss in solid-rotor synchronous reluctance drive", *IEEE Transactions on Power Electronics*, vol. 23, no. 2, pp. 985-992, March 2008.

[9] K. Yamazaki, Y. Kanou, "Rotor loss analysis of interior permanent magnet motors using combination of 2-D and 3-D finite element method", *IEEE Transactions on Magnetics*, vol.45, no. 3, pp.1772-1775, March 2009.

[10] M. Shah, S. Lee, "Rapid analytical optimization of eddy-current shield thickness for associated loss minimization in electrical machines", *IEEE Trans. Ind. Appl.*, vol. 42, no. 3, pp. 642-649, May/Jun. 2006.

[11] G.F. Uler, O.A. Mohammed; Koh Chang-Seop, "Design optimization of electrical machines using genetic algorithms", *IEEE Transactions on Magnetics*, vol. 31, no. 3, pp.2008-2011, May 1995.

[12] R. Sabzehgar; M. Moallem, "A review of ocean wave energy conversion systems", *2009 IEEE Electrical Power & Energy Conference (EPEC)*, 22-23 Oct. 2009.

Chapter 8

Analytical Calculation of Air-Gap Armature Reaction Field Including Slotting Effects in Fractional-Slot Concentrated-Coil SPM Multiphase Machines

8.1   Introduction

Fractional-slot concentrated-coil synchronous machines with Surface Permanent Magnet (SPM) rotor are often used in those applications where a high number of poles, closely approaching the number of stator slots, is required [1]. One major criticalities of these machines is the occurrence of large air-gap magnetic field harmonics, which arise due both to stator winding distribution and to slotting effects [2]. These field harmonics are important to be considered in the design stage as they may cause important eddy-current losses in rotor PMs. Air-gap field harmonic effects can be investigates through time-stepping Finite Element (FE) tools which are capable of including rotor motion and eddy-current phenomena in the analysis [3]. However, it is well known how these approaches are very time consuming, which makes analytical methods highly attractive alternative provided that they are capable of capturing the details of machine topology with adequate accuracy. For this purpose, some analytical formulations of air-gap magnetic field in SPM concentrated-winding synchronous machines are proposed and comparatively assessed. The methods presented hold for any number n of stator phases and differ among them by the way in which

stator slotting effects is taken into account [4]. The different formulations are assessed comparatively by evaluating their analytical outputs against FE analysis results on different machine configurations.

8.2   Assumptions and notations

Let us consider an n-phase machine with $2p$ poles and Z slots. The rotor is supposed to be cylindrical with Surface Permanent Magnets (SPM) and the stator winding constituted by single-layer concentrated coils each wound around a stator tooth, according to the sketch shown in fig.8.1. We shall assume the following simplifications:

1. Unsaturated stator and rotor cores;

2. Relative permeability of PMs equal to that of the air.

Thanks to the above assumptions, the only geometrical quantities which affect the air-gap magnetic field due to stator currents are (fig.8.1):

1. the tooth width at the air-gap (τ_t);

2. the slot opening at the air-gap (τ_s);

3. the air-gap width (δ);

4. the mean air-gap radius (R).

In particular, we notice that, in virtue of the assumption about PM permeability, the air-gap can regarded as the "*magnetic*" air-gap, i.e. neglecting the presence of PMs.
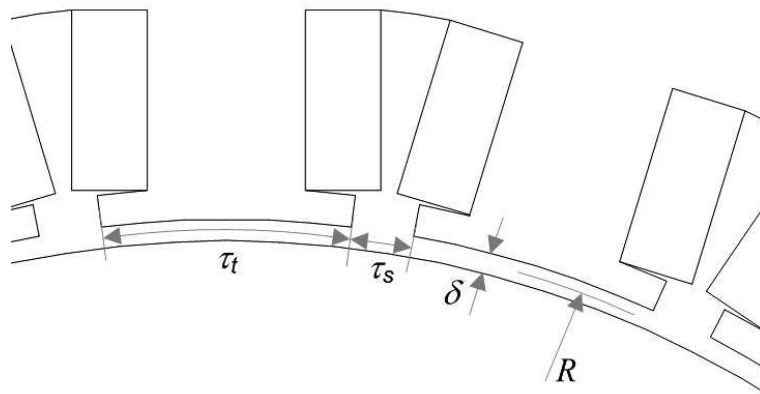

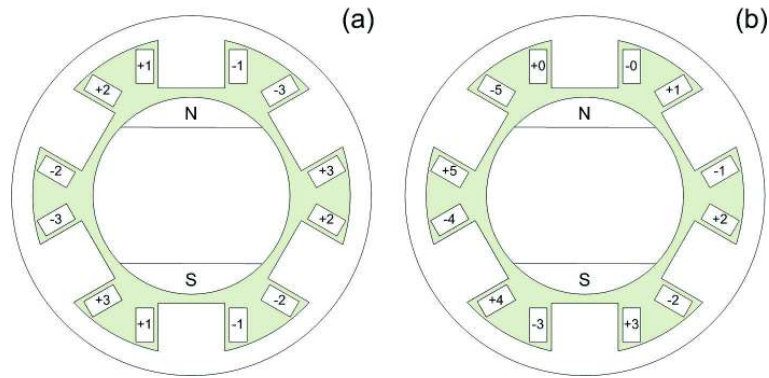Figure 8.1: Significant geometric quantities and their symbols.

124

Figure 8.2: Example of a two-pole three-phase machine (a) with usual phase names; (b) after renaming stator phases sequentially from 0 to 5.
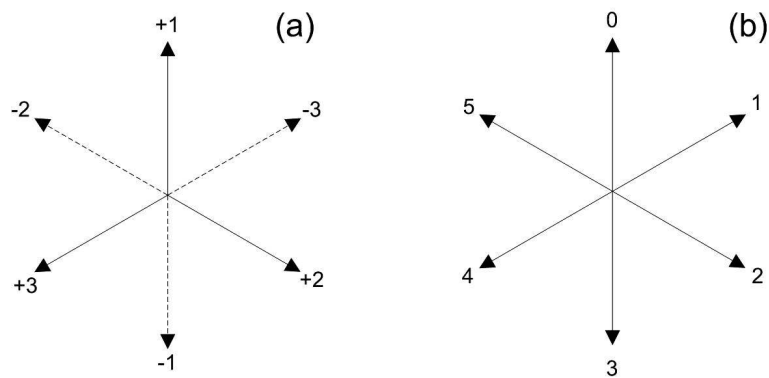

Figure 8.3: Example of a two-pole three-phase machine (a) with usual phase names; (b) after renaming stator phases sequentially from 0 to 5.

As concerns the stator circuit modeling, it is clear that in an n-phase machine each coil can belong to one of the n phases and, furthermore, it can be wound in two possible directions around its tooth (fig.8.3a exemplifies the concept in the simplest case of a two-pole three-phase machine). In other terms, each coil may carry a current represented by one of the six phasors in fig.8.2a.). In other terms, each coil may carry a current represented by one of the six phasors in fig.8.3a. For modeling reasons, it is convenient to rename such phasors in a sequential order, from 0 to $2n - 1$, as shown in fig.8.3b. This leads to an equivalent $2n$ machine, as exemplified in fig.8.2b, which represents the same machine as fig.8.2a after phase renaming.

The Z stator coils will be numbered sequentially from 0 to $Z - 1$ and the position along the mean air-gap circumference will be defined by an angular coordinate x whose origin corresponds to the axis of the coil number 0 (see fig.8.4). The arrangement of the stator phases is supposed to be determined in accordance with the "star of slots" criterion [5]. According to this criterion, the kth stator coil (with $k = 0 \ldots Z - 1$) is assigned to the phase P_k (with $P_k = 0 \ldots 2n - 1$) such that:

$$P_k = mod \left[round \left(k \frac{2n}{Z} p \right), 2n \right] \tag{8.1}$$

8.3 Expression of air-gap field through permeance and winding functions

An effective method to express the magnetic field due a certain current flowing through different stator circuits is to use permeance and winding functions. The winding function of a stator circuit represents the MMF distribution that originates in the air-gap when the circuit carries a unitary current.

In our case, the circuits are the Z stator coils. Calling $i_0(t)$, $i_1(t) \ldots i_{2n-1(t)}$ the currents flowing through the $2n$ stator phases (fig.8.2b, fig.8.3b) at a given instant t and applying the principle of superposition of effects, the MMF due to all the Z coils is:

$$MMF(x,t) = \sum_{k=0}^{Z-1} W_k(x) i_{P_k}(t) \tag{8.2}$$

where $W_k(x)$ is the winding function of the kth coil and $i_{P_k}(t)$ the current flowing through it, with P_k given by (8.1). The air-gap magnetic field due to the armature reaction is computed by multiplying the MMF by the permeance function: $P(x)$:

$$H(x,t) = P(x) MMF(x,t) = P(x) \sum_{k=0}^{Z-1} W_k(x) i_{P_k}(t) \tag{8.3}$$
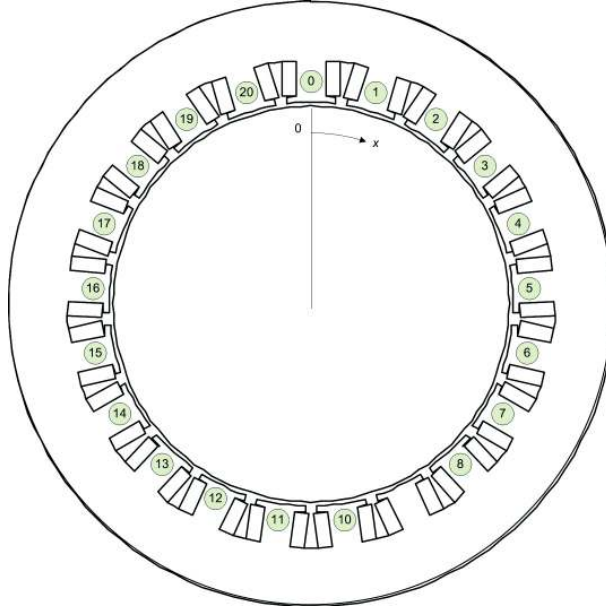
Figure 8.4: Sequential numbering of stator coils and origin of the angular coordinate x.

In steady-state sinusoidal balanced operation, the current flowing through phase P (with $P = 0 \ldots 2n - 1$) is given by (see fig.8.3b):

$$i_P(t) = I_0 \cos\left(\omega t - P\frac{\pi}{n}\right) \tag{8.4}$$

which, substituted into (8.3), gives:

$$H(x,t) = P(x)I_0 \sum_{k=0}^{Z-1} W_k(x) \cos\left(\omega t - P\frac{\pi}{n}\right) \tag{8.5}$$

The problem is now to derive analytical and easy-to-compute expressions for both the permeance function and the coil winding function.

8.4   Coil winding function

Defining the slot pitch α in mechanical radians as (fig.8.1):

$$\alpha = 2\pi\frac{R}{Z} \tag{8.6}$$

we have that, according to the conventions illustrated in fig.8.4, the kth coil has its symmetry placed at $x = k\alpha$.

127
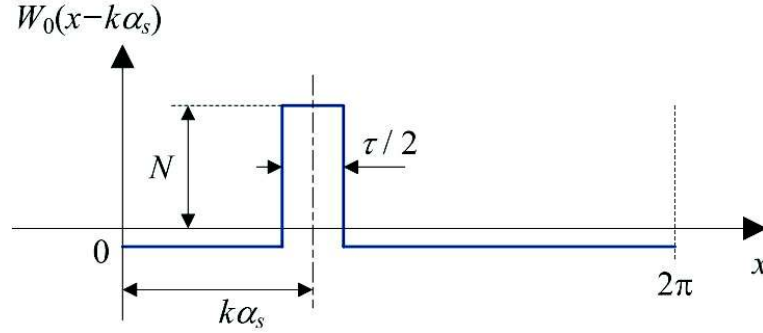
Figure 8.5: Winding function of a concentrated coil.

To a good approximation, the winding function of the kth stator coil can be represented as in the diagram shown in fig.8.5, where N is the number of turns per coil and $W_0(x)$, expressed in Fourier series, is:

$$W_0(x) = \frac{2N}{\pi} \sum_{n=1}^{\infty} \frac{\sin n\pi/Z}{n} \cos(nx) \qquad (8.7)$$

Therefore the expression of $W_k(x)$ to be used in (8.5) is:

$$W_k(x) = W_0(x - k\alpha) = \frac{2N}{\pi} \sum_{n=1}^{\infty} \frac{\sin n\pi/Z}{n} \cos\left[n(x - k\alpha)\right] \qquad (8.8)$$

8.5 Permeance function

In an electric machine with uniform air-gap the permeance function would be a constant equal to the inverse of the air-gap width. In general, it also accounts for the air-gap non-uniformity, which, in the machines under study, can be due to stator slot openings only. The permeance function can take different analytical forms depending on how the air-gap flux density dip, which occurs at any slot opening, is modeled mathematically [4]. In the following, three approaches are taken into account, i.e. the purely sinusoidal approximation, Weber's approximation and a "piecewise" approximation. For all cases it is useful to introduce the following coefficients:

$$u = \frac{\tau_s}{2\delta} + \sqrt{1 + \left(\frac{\tau_s}{2\delta}\right)^2} \qquad (8.9)$$

$$\beta = \frac{1 + u^2 - 2u}{2\left(1 + u^2\right)} \qquad (8.10)$$

such that the permeance function varies between P_{max} and P_{min} defined as follows:

$$P_{max} = \frac{1}{\delta}, P_{min} = \frac{1 - 2\beta}{\delta} \qquad (8.11)$$

128

8.5.1 Sinusoidal approximation
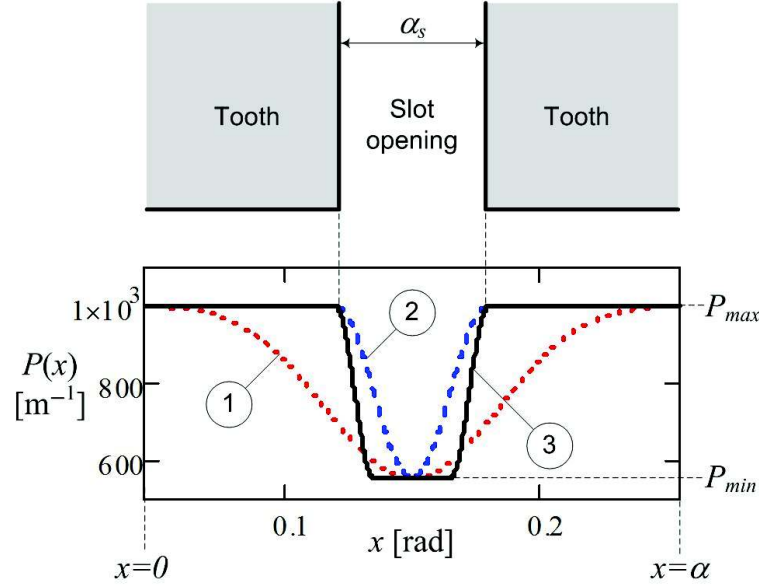
Figure 8.6: Permeance function shapes. 1-Weber approximation; 2-Sinusoidal approximation; 3-Piecewise approximation.

According to this approximation, the permeance function is assumed to be constant in front of the tooth and to have a sinusoidal profile in front of the slot opening (fig.8.6). If we define the mechanical angles corresponding to the tooth and slot opening widths:

$$\alpha_s = \frac{\tau_s}{R}, \alpha_t = \frac{\tau_t}{R} \tag{8.12}$$

the analytical expression of the permeance function over a slot pitch is then:

$$P'(x) = \begin{cases} P_{max} & if 0 \leq x < \alpha_t/2 \vee \alpha_s + \alpha_t/2 \leq x < \alpha \\ A + B \cos\left[\frac{2\pi}{\alpha_s}\left(x - \frac{\alpha_t}{2}\right)\right] & if \frac{\alpha_t}{2} \leq x < \frac{\alpha_t}{2} + \alpha_s \end{cases} \tag{8.13}$$

where $A = (P_{max} + P_{min})/2$ and $B = (P_{max} - P_{min})/2$; the permeance function over the entire air-gap circumference $(0 - 2\pi)$ is finally [function $mod(y, z)$ indicating the reminder of x/y division]:

$$P(x) = P'\left(\mid mode(x, \alpha) \mid\right) \tag{8.14}$$

8.5.2 Weber's approximation

According to this approximation, the permeance function over a slot pitch is assumed to have the following expression:

$$P'(x) = P_{max} \left[1 - \beta \sin^{2\gamma} \left(\frac{Zx}{2} \right) \right] \qquad (8.15)$$

where

$$\gamma = \frac{\tau_t}{\tau_s} \qquad (8.16)$$

the overall permeance function, extended to the entire air-gap circumference, is again given by (8.14).

8.5.3 Piecewise approximation
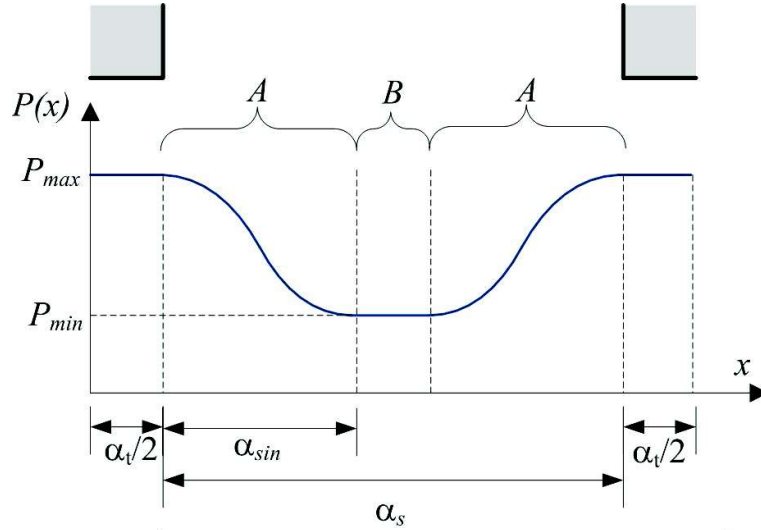
Figure 8.7: Piecewise approximation of the permeance function over a slot pitch.

   According to this approximation, the slot opening region is subdivided into three areas as depicted in fig.8.7. In areas **A**, which spans α_{sin} mechanical radians, the permeance function is assumed to have a sinusoidal profile; in area **B**, spanning $(\alpha_s - \alpha_{sin})/2$, the permeance function is assigned a constant value equal to P_{min}. Outside the slot opening region, it is assumed equal to P_{max} as in the sinusoidal approximation.

8.6 Analytical field expression

Substitution of (8.8) into (8.5) gives:

130

$$H(x,t) = P(x)\frac{2NI_0}{\pi} \sum_{n=1}^{\infty} \left\{ \frac{\sin(n\pi/Z)}{n} \times \sum_{k=0}^{Z-1} \cos\left[n(x-k\alpha)\right] \cos\left(\omega t - P_k \frac{\pi}{n}\right) \right\}$$

$$(8.17)$$

Through simple trigonometric manipulations and passing to exponential notation we can rewrite (8.17) as follows:

$$H(x,t) = P(x)\frac{NI_0}{\pi} \sum_{m=1}^{\infty} Re\left\{ M_m^- \exp\left[i\left(\omega t - mx\right)\right] + M_m^+ \exp\left[i\left(\omega t + mx\right)\right] \right\}$$

$$(8.18)$$

where

$$M_m^- = \frac{\sin(m\pi/Z)}{m} \sum_{k=0}^{Z-1} \exp\left[-2\pi\left(\frac{P_k}{2n} - \frac{mk}{Z}\right)\right] \tag{8.19}$$

$$M_m^+ = \frac{\sin(m\pi/Z)}{m} \sum_{k=0}^{Z-1} \exp\left[-2\pi\left(\frac{P_k}{2n} + \frac{mk}{Z}\right)\right] \tag{8.20}$$

In (8.18), the total magnetic field is expressed as the sum of its harmonic revolving fields which rotate in the same direction as the rotor (superscript "−") and in the opposite direction (superscript "+"). It is recalled that the permeance function $P(x)$ is expressed in one of the ways discussed in Section 8.5 and P_k is given by (8.1).

8.7 Finite element assessment
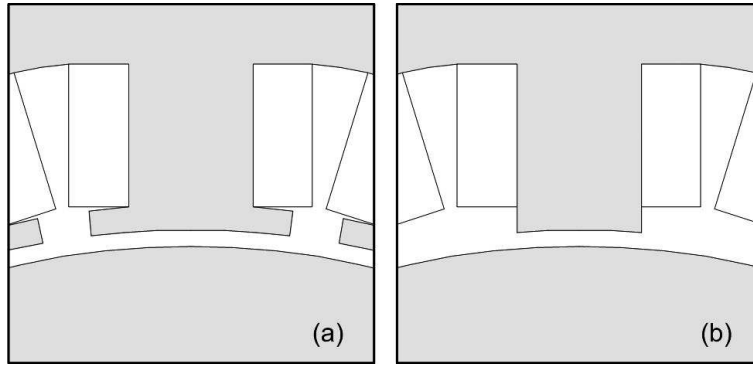
Figure 8.8: Tooth profiles taken into account: (a) with tips; (b) without tips.

In this Section the previously derived analytical model of the air-gap magnetic field, including slotting effects through the permeance function

$P(x)$, is assessed by comparing its results with Finite Element (FE) calculations on some sample machine topologies. Basically, the machine cross section shown in fig.8.4 is taken, characterized by $Z = 21$ stator slots, $2p = 16$ poles, $N = 10$ turns per coil, $I_0 = 10A$ per turn. The winding is assumed to be a three-phase one ($n = 3$). The $2n$ equivalent phases (see fig.8.2b,8.3b) are arranged according to Tab.8.1.

STATOR PHASE ARRANGEMENT										
k	0	1	2	3	4	5	6	7	8	9	10
P_k	0	2	5	1	3	5	2	4	0	3	5
k	11	12	13	14	15	16	17	18	19	20
P_k	1	3	0	2	4	1	3	5	1	4

Table 8.1: Stator phase arrangement

The two topologies considered differ by the tooth shape (tipped or straight, [6]), as depicted in fig.8.8.
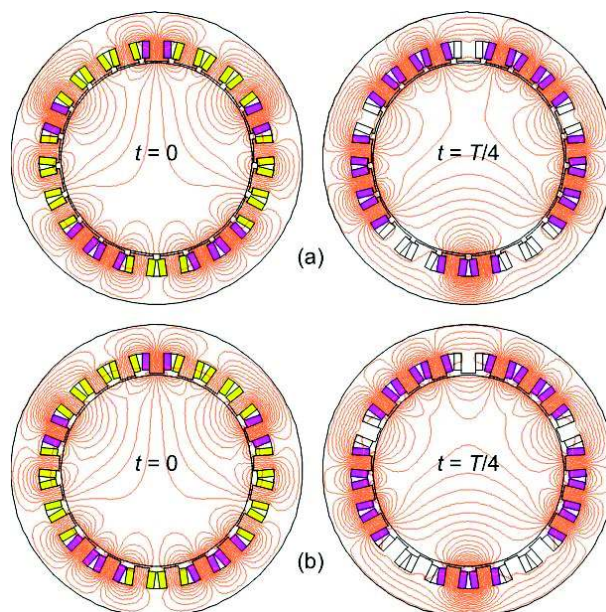
Figure 8.9: FE solutions of the model (a) with tooth tips and (b) without tooth tips, at different instants t ($t = 0$ and $t = T/4$).

The expression given in Section 8.6 for the air-gap magnetic field depends both on the time t and on the space coordinate x. In order to assess both dependencies, the FE simulations on the above described machine are repeated for two instants of time, i.e. for $t = 0$ and for $t = T/4$, where T indicates the period of stator currents (fig.8.9).

Figure 8.10: FE solutions of the model with tooth tips at different instants t ($t = 0$ and $t = T/4$), compared to analytical model outputs.

The FE simulation results, together with analytical computation outputs obtained from (8.18)-(8.20) for different choices of the permeance function $P(x)$, are reported in fig.8.10 and fig.8.11. The piecewise approximation, in particular, has been implemented assuming $\alpha_{sim} = \alpha_s/4$ (see fig.8.7).

Fig.8.10 refers to the machine topology with tipped teeth and fig.8.11 to the machine topology with straight teeth (the latter topology is especially significant for large machines where preformed coils made of flat turns are used instead of wire).

The plot of the magnetic field diagram over the entire air-gap circumference shows that the analytical approximation well matches FE calculations as concerns both the spatial distribution and the time dependency.
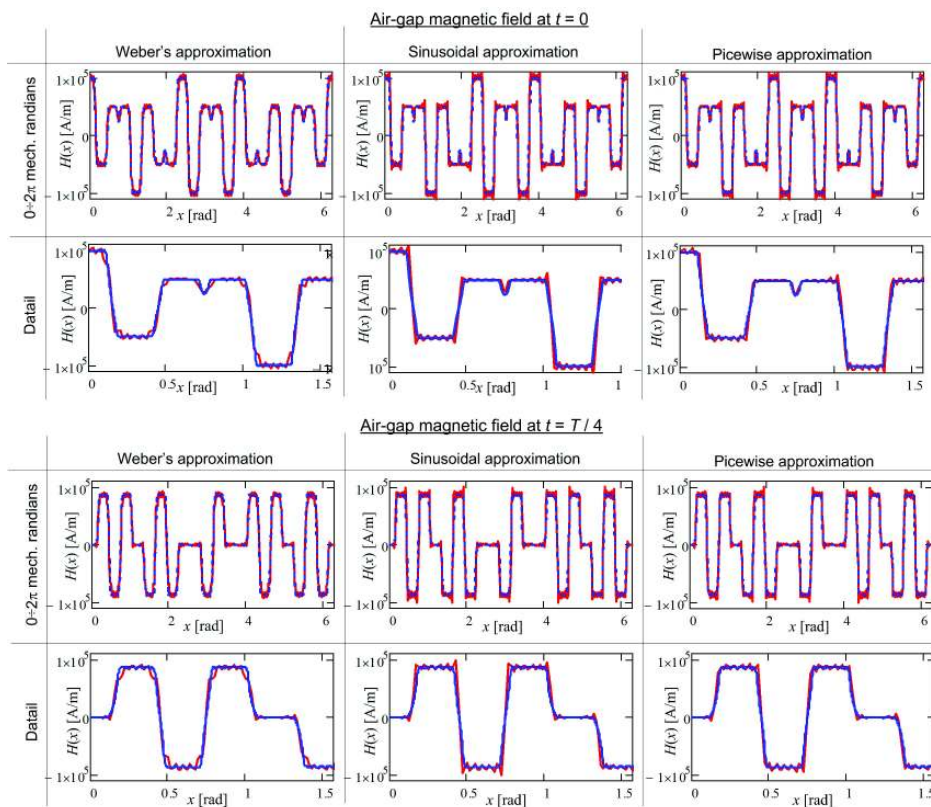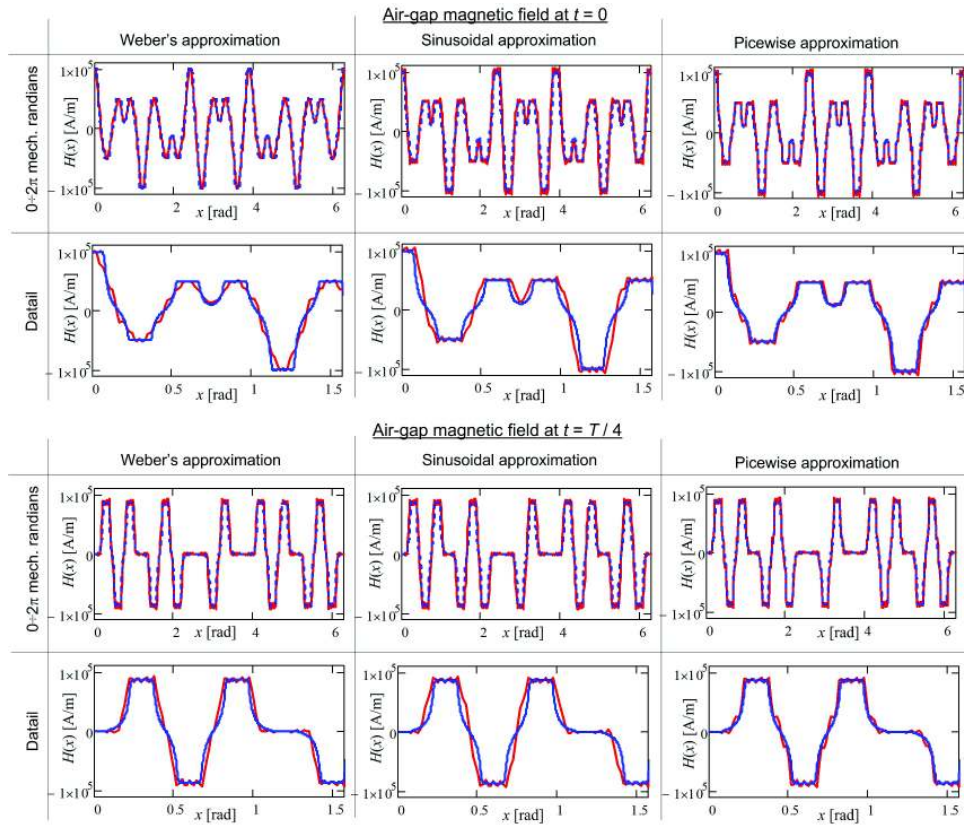

Figure 8.11: FE solutions of the model with straight teeth at different instants t (t=0 and t=T/4), compared to analytical model outputs.

Looking at the detailed field profile (which is done by zooming on the x-axis interval between 0 and $1.5 radians$), one can make the following observations:

1. In the topology with tipped teeth (fig.8.10), a satisfactory matching

is achieved with any approximation of the permeance function. In fact, the slot opening is in this case small compared to the air-gap and therefore the resulting field dips are small.

2. In the topology with straight teeth (fig.8.11), the piecewise approximation of the permeance function gives definitely better results compared to the sinusoidal and Weber's one. The difference between the various approximations takes more importance in this case due to the larger slot opening and to the consequent depth of the magnetic field dips.

8.8   Conclusions

In this chapter an analytical formulation of the armature reaction magnetic field in the air-gap of fractional-slot concentrated-coil electric machines has been discussed, including slotting effects. The analytical expression describes the air-gap field profile as a spatial distribution and as a function of time. It applies to a generic number of stator phases which are assumed to be distributed according to the "*star of slots*" criterion. Slotting effects are accounted for though different possible formulations of the permeance function, differing by how the air-gap flux density dips due to slot openings are modeled. The analytical expression proposed is applied to the case of an example 21-slot 16-pole machine in two different topologies, i.e. with straight and tipped stator teeth. The comparison between analytical and FE results for this machine has been presented. In case of tipped teeth a good accordance has been found regardless of the permeance function approximation. Conversely, a higher sensitivity to the permeance function has been found in the case of straight teeth, where a best permeance function formulation has been identified.

8.9   References

[1] A. M. El-Rafaie, "Fractional-slot concentrated-windings synchronous permanent magnet machines: opportunities and challanges", *IEEE Trans. on Industrial Electronics*, vol. 57, no. 1, Jan. 2010, pp. 107-121.

[2] N. Bianchi, E. Fornasiero, "Impact of MMF stace harmonic on rotor losses in fractional-slot permanent-magnet machines", I*EEE Trans. on Energy Conversion*, June 2009, vol. 24, issue 2, pp. 323-328.

[3] N. Sadovski, M. L. Mazenc, J. P. A. Bastos, M. V. Ferreira da Luz, P. Kuo-Peng, "Evaluation and analysis of iron losses in electrical machines using the rain-flow method", *IEEE Trans. on Magnetics*, vol. 36, no. 4, July 2000, pp. 1923-1926.

[4] M. B. B. Sharifian, M. R. Feyzi, M. Farrokhifar, K. Shaarbafi, R. Mahommadi, "Slot fringing effect on the magnetic characteristics of electrical machines", *Journal of Electrical Engineering*, vol. 60, no. 1, pp. 18-23.

[5] N. Bianchi, M. Dai Pre, "Use of the star of slots in designing fractional-slot single-layer synchronous motors", *IEE Proceedings on Electric Power Applications*, May 2006, vol. 153, issue 3, pp. 459-466.

[6] P. B. Reddy, T. M. Jahns, "Modeling of stator teeth-tip iron losses n fractional-slot concentrated-winding surface4 PM machines", *IEEE Energy Conversion Congress and Exposition*, 2009, 20-24Sept. 2009, San Jose, CA, pp. 1903-1910.

Chapter 9

Use of Time-Harmonic Finite-Element Analysis to Compute Stator Winding Eddy-Current Losses Due to Rotor Motion in Surface Permanent-Magnet Machines

9.1   Introduction

Surface permanent-magnet (SPM) electric machines having small power ratings are usually wound with thin round-section wire. Their electromagnetic design, in fact, generally features a large number of turns per phase, each carrying a small current. The use of thin wire brings two advantages. Firstly the conductor cross section can be kept very small, so that skin-effects and eddy current losses take negligible importance [1]. Secondly, the stator slot opening can be small as well (which helps reduce slotting effect [2]), typically just a little larger than wire diameter so that conductors can be placed into the slot during stator manufacturing. On the other side, the electromagnetic design of large SPM machines is generally characterized by few conductors per slot, each carrying a significant current [3], [4]. Stator coils then need to be composed of flat turns with rectangular cross-section and an open slot design needs to be adopted to allow for preformed coil insertion. A known issue connected with the open slot design lies in the occurrence of eddy-current losses due to the machine flux entering slot openings and crossing the conductors placed closest to the air-gap. This phenomenon has been deeply investigated in the literature [5], showing how it can cause a non-uniform

current distribution over the preformed coil cross section and consequent local temperature rise problems [5], [6]. The aforementioned problem needs to be taken into account during the design of a large SPM machine with open slots and rectangular cross-section conductors. An effective approach for the purpose is offered by Time-Stepping Finite-Element Analysis (TS-FEA), where rotor motion is included in the simulation and the additional copper losses under study can be naturally predicted [6]. Although effective, TSFEA approach is yet little efficient, in the sense that it requires long computation time and results need to be extracted through quite cumbersome post-processing operations. Therefore, TSFEA is a little suitable computation method when the machine design is to be defined through a genetic optimization program and the losses under study are to be automatically calculated at each optimization step [7]. The contribution of this chapter is to set forth a new computationally-efficient method for the computation of additional copper losses due to rotor motion in SPM machines with open slots. The method requires solving a set of Time-Frequency Finite-Element Analysis (TFFEA) simulations [8] on a suitably modified machine model where permanent magnets are replaced by a grid of fictitious conductors carrying sinusoidal currents. Such TFFEA simulations are shown capable of accurately reproducing rotor motion effects, although in each simulation the rotor is at stand-still. The advantage of the method proposed is that it takes much shorter time than TSFEA and can be implemented in the form of a fully automated computation procedure, which is suitable for being integrated into a genetic design optimization program [7]. In fact, an application of the method is reported in this chapter to the design optimization of a fractional-slot SPM prototype alternator conceived for generating electric power from sea wave energy conversion [9]. The accuracy of the method proposed is assessed by comparison with the results independently obtained from it and by TSFEA. The comparison is made on different generator designs explored in the optimization process and considering different operating conditions. A good accordance is found in all the cases taken into account.

9.2 Study of stator additional copper losses through TSFEA

In order to illustrate the nature of the copper losses under examination and the difficulty of their evaluation, reference is made to an example high-power SPM alternator conceived for clean electric power generation exploiting sea wave energy [9]. A brief generator overview is provided next.

9.2.1 Generator overview

Generator ratings, which are assumed as design constraints, are given in Table 9.1. The output voltage and frequency are treated as a design variable since the machine is connected to the grid by means of a power converter.

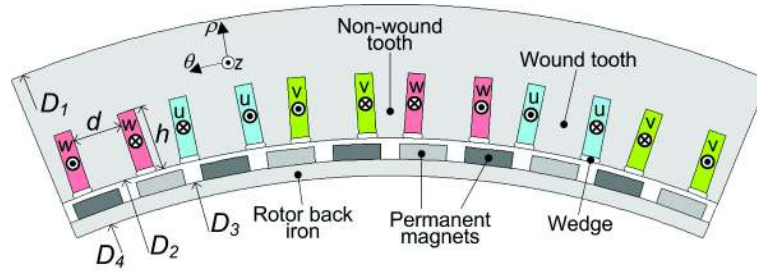| MACHINE RATINGS	
Rated torque	1500 Nm
Maximum voltage	690 V
Rated speed	3 rpm
Maximum speed	5 rpm

Table 9.1: Machine ratings

Figure 9.1: Cross-sectional model of one single machine sector.

The machine is composed of S sectors, each having the basic structure shown in fig.9.1. The sector embraces 6 wound teeth and 10 rotor poles. Concentrated coils are depicted in fig.9.1 with different colors depending on the phase (u,v,w) to which they belong and the conventional current direction is indicated on each coil side. Assignment of the phases to coil sides is performed according to the "*star of slot*" rule applied to the case of 12 slots and 10 poles [10]. The design solution schematically illustrated in fig.9.1 differs from ordinary concentrated coil design [11], shown in fig.9.2b, because the space between adjacent coil sides is not constituted by air but filled with laminations. The chosen design gives some advantages, in particular: it allows for preformed coil assembly and firmer mechanical retention with no need for removable tooth heads; it improves heat withdrawal from stator coils thanks to the high coil-to-core thermal conductivity coefficient [12]; it can lead to torque ripple and cogging torque enhancement by suitable selection of the wound tooth and non-wound tooth width ratio [13]. On the other side, design drawbacks lie in a reduced room for stator coils and
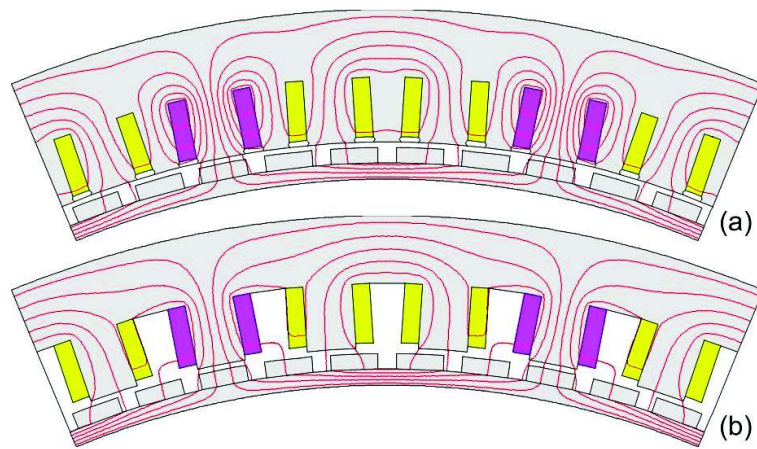
Figure 9.2: (a) Concentrated winding with alternate wound and non-wound teeth; (b) Concentrated winding with all teeth wound.

in a higher slot leakage inductance (as flux lines in fig.9.2 clearly show). The high leakage inductance, however, is beneficial for the machine under study in that it helps reduce the short circuit current to such an extent that operation continuity can be guaranteed even with one shorted coil. Each coil is composed of several series-connected flat turns and its sides are accommodated in a pair of parallel rectangular-section open slots.

Figure 9.3: Example designs of machine sectors explored in the optimization process, drawn in the same scale.

The electromagnetic design of the generator is to be defined by means of a multi-objective constrained optimization program based on genetic al-

gorithms so as to maximize performance and minimize production costs [7]. The number of sectors S and the characteristic design of a single sector (including its span and dimensions D_1, D_2, D_3, D_4, d, h indicated in fig.9.1) are to be selected as a result of the op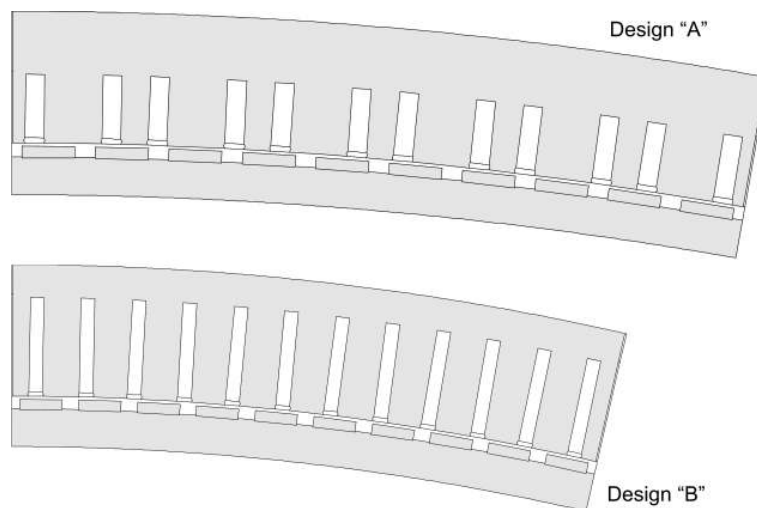timization. For example, fig.9.3 shows two designs explored throughout the optimization and Tables 9.2 and 9.3 give their detailed dimensions and performance data. The two designs will be later used for method assessment (Section 9.5).

9.2.2 No-load additional copper losses and their computation through TSFEA
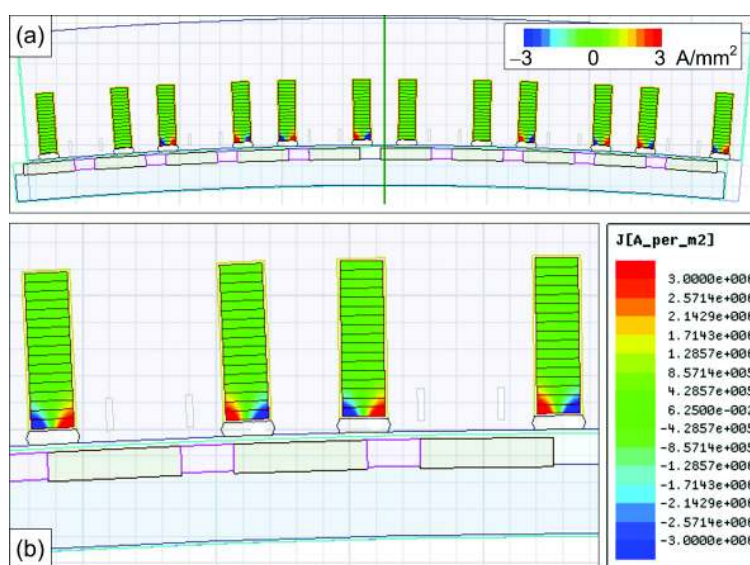
Figure 9.4: TSFEA simulation of the machine at no load, showing eddy currents induced by rotor motion: (a) sector view; (b) detailed view.

An issue of the machine under study is due to the combined presence of open slots, flat turns and a permanent-magnet rotor. The problem is quite well known from the literature [5], [6], and, for the SPM generator under study, can be effectively studied by TSFEA simulations. Taking design **A** as an example (fig.9.3), the results obtained from its simulation at no load are shown in fig.9.4. From the TSFEA snapshot shown in fig.9.4 it can be seen how some current density appears in the flat turns placed on the air-gap side of the slot. In fact, these conductors are swept by permanent-magnet flux lines which enter the stator core not through the teeth but through slot sides (fig.9.5) as a consequence of the open-slot stator design.

Because these flux lines continuously vary their space configuration as the rotor moves, flux pulsations and consequent eddy currents are inducted in the conductors placed near the air-gap.

Figure 9.5: Black circles show the positions where permanent-magnet flux lines enter the core through open slot sides, thus crossing conductors placed near the air-gap.

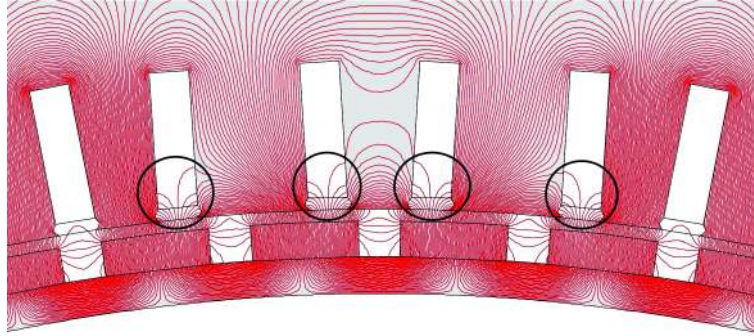| CHARACTERISTIC DATA OF DESIGNS A AND B		
	Design A	Design B
Number of poles	360	280
Number of slots	432	336
Sector angular span [de])	10.00	12.86
Stator outer diameter, D_1 [mm](a)	8250	5250
Stator bore diameter, D_2 [mm](a)	8000	5000
Rotor outer diameter, D_3 [mm](a)	7974	4976
Rotor inner diameter, D_4 [mm](a)	7900	4900
Generator axial core length [mm]	415	830
Air gap width [mm]	3	3
Permanent magnet height [mm]	11	10
Permanent magnet span (% of pole span)	72	72
Permanent magnet coercitivity [kA/m]	950	950
Permanent magnet residual flux density [T]	1.25	1.25
Stator slot height, h [mm](a)	60	90
Stator slot width [mm]	18	13
Stator wedge height [mm]	5	4
Wound tooth width, d [mm](a)	55	35
Number of turns per coil	17	15
Number of parallel ways per phase	6	8
Individual conductor height [mm](b)	2.85	5.3
Individual conductor width [mm](b)	15.5	10.5

Table 9.2: Characteristic data of designs A and B (a) Symbols given in fig.9.1. (b) Copper section (excluding insulation)

142

COMPUTED PERFORMANCE DATA OF DESIGNS A AND B		
	Design A	Design B
Frequency [Hz]	9	7
Phase current [A]	1100	885
Line voltage [V]	517	383
Power factor	0.41	0.69
Copper losses due to fundamental current [kW]	64.2	48.1
Computed efficiency	0.81	0.86
Computed total losses [kW]	94	65

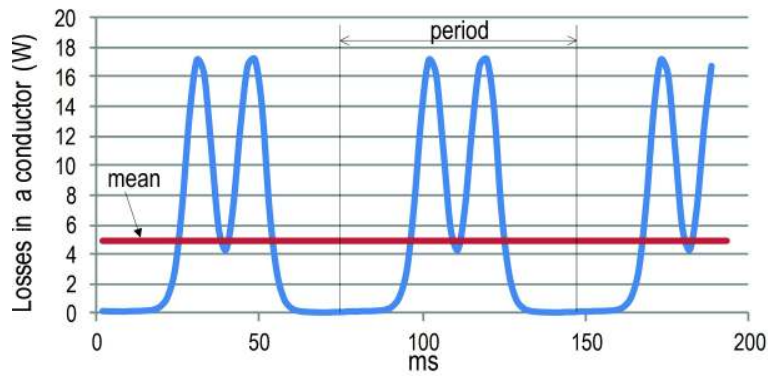Table 9.3: Computed performance data of designs A and B

Figure 9.6: Eddy-current losses in a conductor resulting from TSFEA.

143

As a result of TSFEA simulations, one can obtain diagrams like that shown in fig.9.6 for the steady-state eddy-current losses in a conductor. The output of a TSFEA simulation is a diagram of power losses versus time. What makes sense for power loss evaluation, yet, is not their instantaneous value but their mean value. This is to be computed over a sufficiently long period of time (comprising several periods) characterized by steady-state conditions (i.e. after transients have extinguished). The computation of loss mean value according to these rules is a task that could be hardly implemented into an automatic algorithm. Both the long computation times and the difficulty of automatic result extraction make TSFEA little suitable when the computation is to be performed as a part of a design optimization process, as in the case of the generator under study. In fact, the optimization needs the computation to be repeated at each optimization step (i.e. hundreds or thousands of times) in a fully automated way.

9.3 Approach to additional copper loss computation through THFEA

In this Section an alternative to TSFEA is presented for computing additional copper losses due to rotor motion in SPM machines with open slots and flat-turn coils. The proposed method is based on solving a set of THFEA simulations. Unlike TSFEA, this kind of FEA does not involve any rotor motion in the simulation and assumes that all variable quantities in the model (flux and current densities) have a sinusoidal waveform with a fixed frequency if plotted versus time. However, rotor motion effects can be incorporated into the method being presented by means of some analytical artifices (mainly based on Fourier series theory) as explained below.

9.3.1 Modeling permanent-magnet rotor motion as a sum of continuous magnetization waves

As a first step, let us introduce the cylindrical coordinate system (ρ, θ, z) shown in fig.9.1 ($\hat{\mathbf{u}}_\rho, \hat{\mathbf{u}}_\theta, \hat{\mathbf{u}}_z$ are the relevant unit vectors) and consider a simplified machine model where slot openings are neglected (fig.9.7a). This simplified model is used only for the purpose of determining rotor magnetization, while stator slotting effects are fully accounted for in the final model used for loss computation. In fig.9.7a, γ denotes permanent-magnet span, τ the pole pitch, h permanent-magnet thickness, δ the mechanical air-gap width. Assuming that permanent magnets are uniformly magnetized [14], we have that the magnetization vector $\mathbf{M}$ inside permanent magnets is alternatively equal to $M\hat{\mathbf{u}}_\rho$ and $-M\hat{\mathbf{u}}_\rho$ as we move along rotor periphery. The radial component M_ρ of $\mathbf{M}$, shown in fig.9.7b when the rotor is at position $\theta = 0$, has a Fourier series expansion given by:
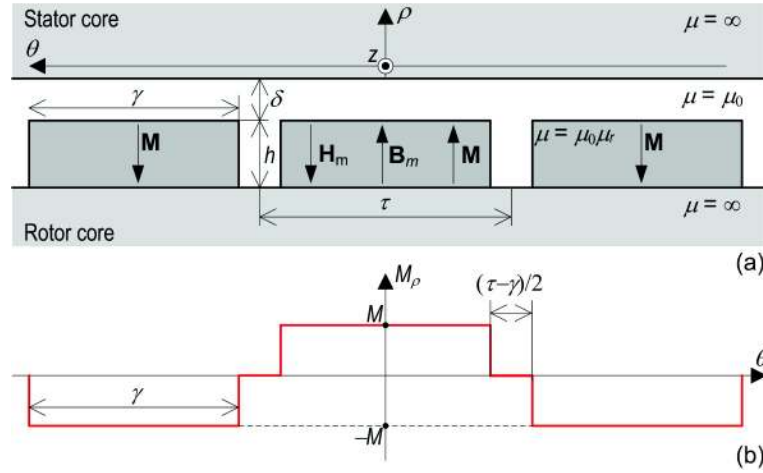
Figure 9.7: (a) Simplified slotless model of SPM machine where air-gap circumference is unrolled along a straight line. (b) Diagram of radial magnetization component.

$$M_\rho(\theta) = \sum_{k=1,3,5,\ldots} \frac{2M}{\pi k} \sin\left(\frac{pk\gamma}{2}\right) \cos\left(pk\theta\right) \tag{9.1}$$

where $p = \pi/\tau$ is the number of pole pairs. In synchronous steady-state conditions, the rotor revolves at ω/p radians per second, where ω is the stator electrical pulsation. At instant t we shall then have the same diagram of M_ρ but shifted by $(\omega/p)t$ radians. Then, (9.1) can be written as a function of both time and space as follows:

$$M_\rho(t,\theta) = \sum_{k=1,3,5,\ldots} \frac{2M}{\pi k} \sin\left(\frac{pk\gamma}{2}\right) \cos\left[pk\left(\theta - \frac{\omega}{p}t\right)\right] \tag{9.2}$$

or equivalently, using phasor notation (see Section 9.7):

$$\overline{M}_\rho(t,\theta) = \sum_{k=1,3,5,\ldots} \frac{2M}{\pi k} \sin\left(\frac{pk\gamma}{2}\right) e^{ipk\theta} e^{-ik\omega t} = \sum_{k=1,3,5,\ldots} \overline{\mu}_k(\theta) e^{-ik\omega t} \tag{9.3}$$

where overlined symbols indicate complex variables and

$$\overline{\mu}_k(\theta) = \sum_{k=1,3,5,\ldots} \frac{2M}{\pi k} \sin\left(\frac{pk\gamma}{2}\right) e^{ipk\theta} \tag{9.4}$$

The value of magnetization M can be found by solving the following system of equations, that link the magnitudes of the vectors represented in fig.9.8.

$$M = B_m/\mu_0 + H_m \qquad (9.5)$$

$$B_m = B_a = \mu_0 H_a \qquad (9.6)$$

$$H_a \delta - H_m h = 0 \qquad (9.7)$$

$$B_m = \mu_0 \mu_r (H_c - H_m) \qquad (9.8)$$

Equation (9.5) descends from the well-known relationship $\mathbf{B} = \mu_0(\mathbf{H} + \mathbf{M})$ projected along ρ axis [15]; equation (9.6) expresses the continuity of the orthogonal flux density component through the interface between the air-gap and the permanent magnet; equation (9.7) descends from Ampere's law under the assumption that stator and rotor cores are infinitely permeable; equation (9.8) expresses the permanent magnet linear characteristic, being μ_r its relative recoil permeability and H_c its coercivity. Equations (9.5)-(9.8) are five independent relationships linking the five unknowns M, H_m, B_m, H_a. Solving for M yields:

$$M = \mu_r H_c \frac{h + \delta}{h + \mu_r \delta} \qquad (9.9)$$

Since relative recoil permeability μ_r of permanent magnets is usually close to unity, (9.9) shows that M does not practically depend on the air-gap width δ.
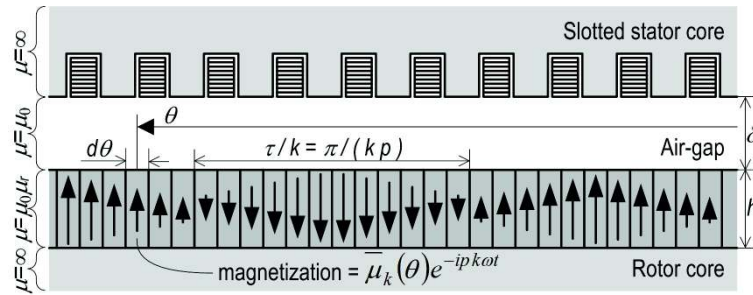

Figure 9.8: Representation of the kth order magnetization harmonic traveling synchronously to the rotor along permanent-magnet region of height h.

Equation (9.3) suggests that the permanent-magnet rotor motion can be simulated by a sum of continuous magnetization waves travelling along a circular layer having the same height h and permeability $\mu_0 \mu_r$ as permanent

magnets and placed around the rotor core (fig.9.8). In particular, fig.9.8 schematically represents the kth order magnetization wave. This has kp pole pairs, i.e. a wavelength of $2\tau/k = 2\pi/(kp)$ mechanical radians (τ being the pole pitch) and travels at the same speed as the rotor (ω/p radians per second).

9.3.2 Finite-element model definition

In principle, the effect of the kth order magnetization wave in terms of induced eddy-current losses could be studied by THFEA based on such a geometrical model as that shown in fig.9.8. In fact, the layer which occupies permanent magnet region is subdivided into infinitesimal radial elements, each spanning $d\theta$ In accordance with (9.3), the element placed at coordinate θ should be assigned a time-variant magnetization, which varies sinusoidally over time with a pulsation equal to $k\omega$ and is represented by phasor $\overline{\mu}_k(\theta)$ given by (9.4). Running a THFEA simulation at pulsation $k\omega$ one could determined the losses produced by the kth order magnetization harmonic in the stator winding. By repeating the calculation for all harmonic orders k appearing in sum (9.3) and summing the results one could finally determine the overall copper losses caused by permanent-magnet rotor motion. Summing the power loss contributions of different harmonics to find the total power loss would be correct because harmonics have unlike frequencies [16]. The problem of the aforementioned approach is that, most of the commercially-available software tools for THFEA do not allow the user to define a time-variant magnetization. In other words, the magnetization which can be assigned to a given material or model region must be represented by a constant vector. The problem can be overcome by considering that the magnetic field due to a body having a uniform magnetization $\mathbf{M}$ in all its points is the same as the field produced by a linear current density $\mathbf{j}_s$ on the body surface such that:

$$\mathbf{j}_s = \mathbf{M} \times \hat{\mathbf{n}} \tag{9.10}$$

where $\hat{\mathbf{n}}$ is the outward-pointing unit vector orthogonal to the body surface [17]. If we apply this equivalence to one of the magnetized element in fig.9.8, we can replace it by an equivalent set of N straight conductors, oriented parallel to z, as shown in fig.9.9. According to (9.10), for the magnetic field distribution to be the same as that produced by the permanent magnet segment, each conductor needs to be assigned a current i_m defined as follows:

$$Ni_m = j_s H = Mh \Rightarrow i_m = Mh/N \tag{9.11}$$

with M given by (9.9). Let us now consider two adjacent magnetized segments (fig.9.8), respectively placed at θ and $\theta + d\theta$. Using notation (9.3),
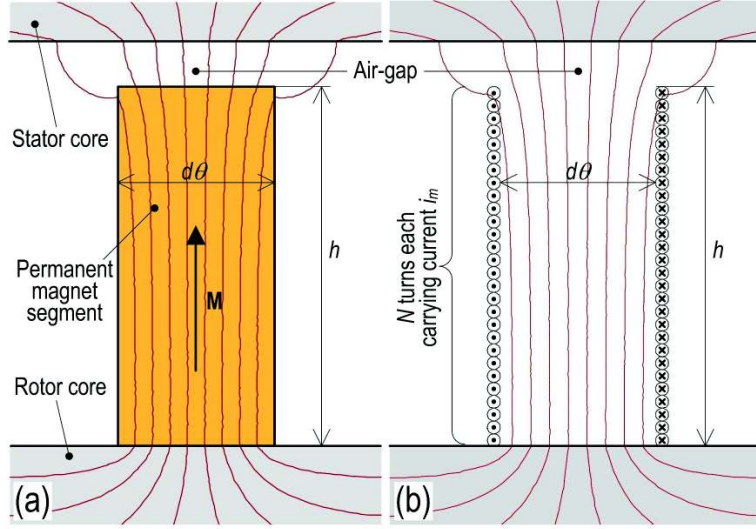
Figure 9.9: Magnetic flux lines produced by: (a) a permanent magnet segment with uniform magnetization M; (b) a set of conductors carrying current $i_m = Mh/N$.

their magnetization radial components will be respectively

$$\overline{M}_\rho(t, \theta) \tag{9.12}$$

$$\overline{M}_\rho(t, \theta + d\theta) = \overline{M}_\rho(t, \theta) + \frac{\partial \overline{M}_\rho(t, \theta)}{\partial \theta} d\theta \tag{9.13}$$

If both segments are replaced by their equivalent set of conductors, on the interface between the two segments we shall have N conductors each carrying a current:

$$\overline{di}_m(t, \theta) = \frac{\partial \overline{M}_\rho(t, \theta)}{\partial \theta} \frac{h}{N} d\theta \tag{9.14}$$

in accordance with (9.11). Using (9.3), (9.4) we can rewrite (9.14) as:

$$\overline{di}_m(t, \theta) = \sum_{k=1,3,5,\ldots} \overline{\lambda}_k(\theta) e^{-ik\omega t} \tag{9.15}$$

where

$$\overline{lambda}_k(\theta) = \frac{\partial \overline{\mu}_k(\theta)}{\partial \theta} = ip\frac{2M}{\pi} \sin\left(\frac{pk\gamma}{2}\right) e^{ipk\theta} \tag{9.16}$$

Finally, if all magnetized segments in fig.9.8 are replaced by their equivalent set of conductors, the model shown in fig.9.10b is obtained. This model is suitable for THFEA provided that one harmonic order is considered at a
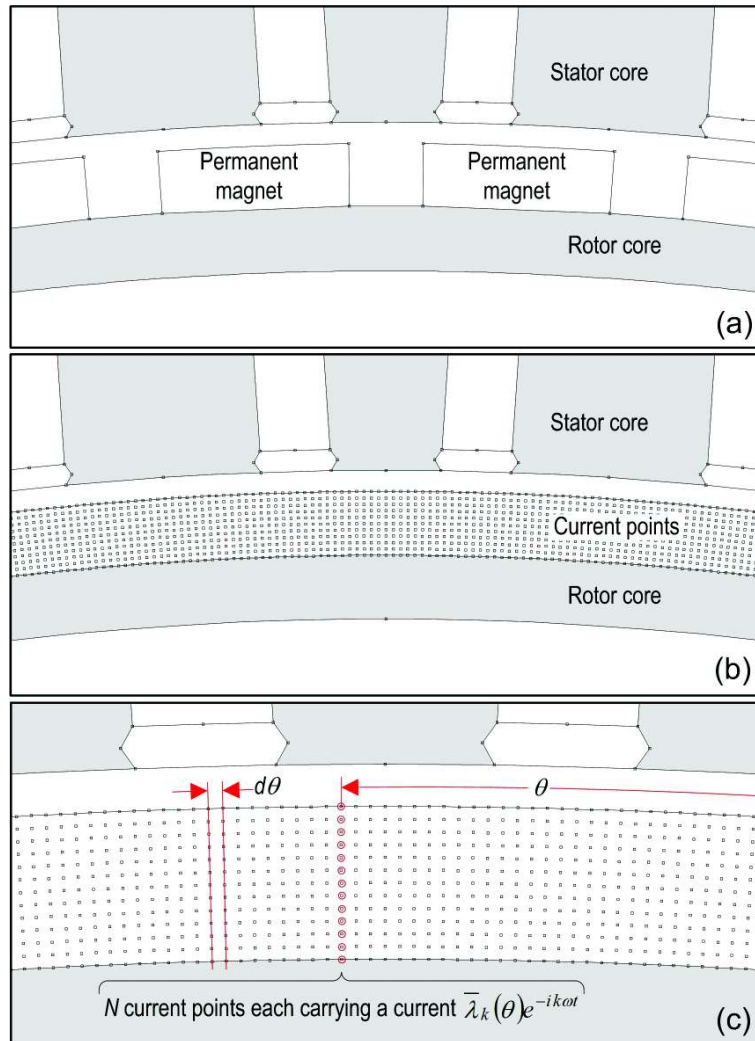
Figure 9.10: (a) Original model; (b) model with current points replacing permanent magnets; (c) zoomed view of the current point region for the simulation of the kth order magnetization harmonic.

time. For instance, fig.9.10c refers to the simulation of the kth order harmonic. To simulate the effect of the kth order harmonic, the N conductors at position θ (aligned in radial direction) must carry the current $\overline{\lambda}_k(\theta)e^{-ik\omega t}$ based on (9.15). This is obtained by assigning such N conductors the complex phasor $\overline{\lambda}_k$ and solving the model through a THFEA simulation at the fixed pulsation $k\omega$. As a result of the simulation, the eddy-current losses $P_{Cu,k}$ induced in stator conductors by the kth order harmonic at steady-state can be immediately computed. Of course, the procedure is to be repeated for all significant odd harmonics orders k. Finally, the total copper losses P_{Cu} produced in the stator winding by the permanent-magnet rotor motion are determined by summing the single harmonic contributions:

$$P_{Cu} = \sum_k P_{Cu,k} \qquad (9.17)$$

Applying the superposition principle to power losses is correct because all the harmonics have unlike frequencies [16].

9.4 Numerical implementation and results

The approach described in Section 9.3 is implemented and applied to the generator described in Section 9.2, taking design **A** as an example (fig.9.3, Tables 9.2, 9.3). For this purpose, the modified model shown in fig.9.10b-c is built by means of a script program which is executed in batch mode by the THFEA program. Each conductor in the permanent-magnet region is represented by a "*current point*" to which the script assigns the appropriate current in the complex phasor form (9.16) for any given harmonic order k. The number N of radially-aligned current points as well as the displacement angle $d\theta$ (fig.9.10c) can be defined in the script as a parameters. In this instance, the following values are selected: $N = 13$, $d\theta = 0.25$ mechanical degrees.

9.4.1 Preliminary check on modified model accuracy

The modified model, characterized by a grid of current points (fig.9.10b), has been defined so that it produces the same air-gap flux density as the original model (fig.9.10a) at any instant of time. This is preliminary checked by making a comparison between the flux density $B_{pm}(\theta)$ produced, on the air-gap mean circumference, by permanent magnets and the flux density $B_{cp(\theta)}$ generated by current points at time $t = 0$. $B_{pm}(\theta)$ is computed by a magnetostatic simulation on the model shown in fig. 10a. The flux density produced by current points is obtained by running 11 magnetostatic simulations (for $k = 1, 3, 5, \ldots, 21$) on the modified model shown in fig.9.10b-c. In the kth simulation, the N current points placed at position θ (fig.9.10b) are assigned a current equal to:

$$Re\left\{\overline{\lambda}_k(\theta)\right\} = -p\frac{2M}{p}\sin\left(\frac{pk\gamma}{2}\right)\sin\left(pk\gamma\right) \qquad (9.18)$$

Calling $B_{cp,k}(\theta)$ the flux density obtained on the mean air-gap circumference from the kth magnetostatic simulation, the overall flux density $B_{cp}(\theta)$ produced by current points is obtained as the sum of all harmonic contributions:

$$B_{cp}(\theta) = \sum_{k=1,3,\dots,21} B_{cp,k}(\theta) \qquad (9.19)$$

The result of the comparison is shown in fig.9.11, where $B_{pm}(\theta)$ and $B_{cp}(\theta)$
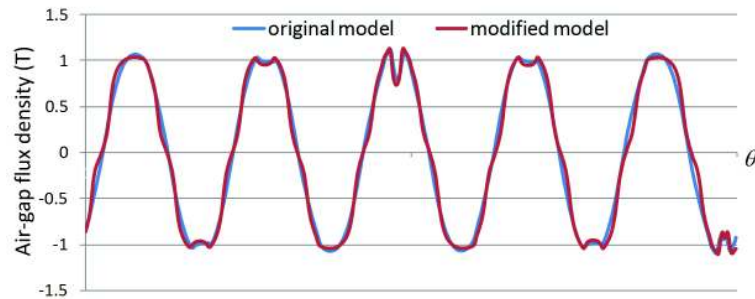

Figure 9.11: Air-gap flux density computed by magnetostatic FEA on the original model with permanent magnet (fig. 10a) and on the modified model with current points (fig. 10b) at instant $t = 0$.

are plotted on a range of θ embracing 10 poles (one machine sector). It can be seen that a good matching is found between the two flux density diagrams.

9.4.2 Detailed results of THFEA simulations

After the magnetostatic check described above, THFEA simulations are used to determine copper losses in the stator winding according to the method presented in Section 9.3 based on the modified model shown in fig.9.10b-c. A range of space harmonic orders k from 1 to 21 is considered and the 17 conductors inside a slot are numbered as shown in fig.9.12.

For any $k = 1, 3, \dots, 21$, a THFEA is run on the modified model at pulsation $k\omega$. As a result of the kth simulation, the copper losses are computed which originate in each of the 17 conductors contained in a slot. The result is given in fig. 13. It is apparent from fig.9.13 that only the fundamental $(k = 1)$ significantly contribute to the power losses, while the effect of higher order harmonics is definitely negligible. Moreover, it is evident how the loss
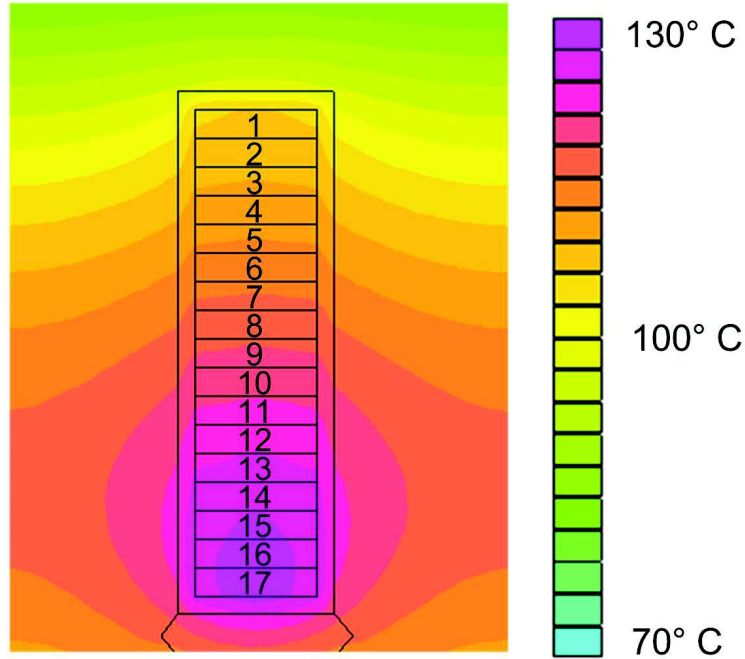
Figure 9.12: Numbering of conductors inside a stator slot and temperature field in the slot region.

distribution in the slot is strongly non-uniform: the conductors placed near the air-gap are the most loaded, while eddy-current entity decays as we move from the air-gap to the bottom of the slot. This phenomenon has been qualitatively discussed in Section 9.2 and is consistent with what is reported in [5], [6], [8]. The losses P_k due to the kth order harmonics are obtained by summing the losses of the conductors in a slot and multiplying the sum by the number of slots (equal to $12 \times S$ being S the number of segments in the design under analysis). The property that losses P_k are negligible for $k > 1$ is reasonably supposed to hold for all design configurations of the machine being optimized (this is actually checked on 15 different sample design configurations). As a consequence, (9.17) simplifies into:

$$P_{Cu} \cong P_{Cu1} \tag{9.20}$$

From a computational viewpoint, this constitutes a noticeable benefit as it says that one single THFEA simulation, run for $k = 1$ i.e. at stator pulsation ω , should be sufficient to determine stator copper losses due to rotor motion. Actually, also harmonic orders $k = 3$ and $k = 5$ are considered in the optimization algorithm implemented. Because the loss computation under discussion needs to be repeated at each design optimization loop (see Section 9.2), using the THFEA-based method leads to significantly shorten
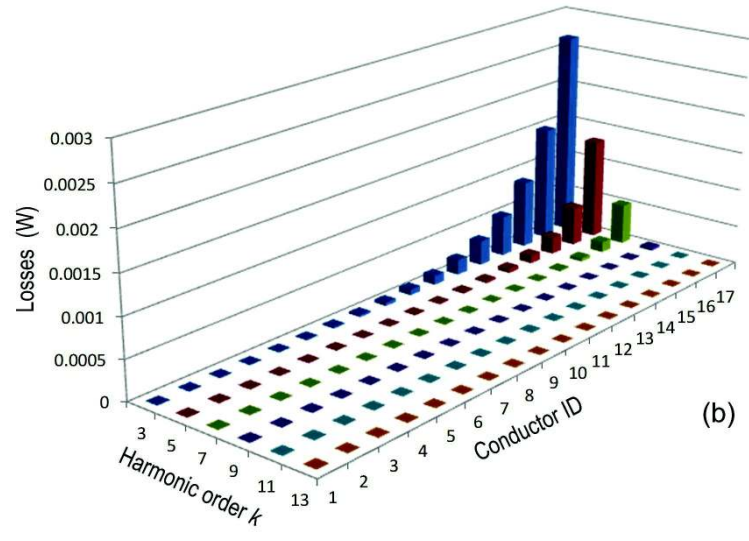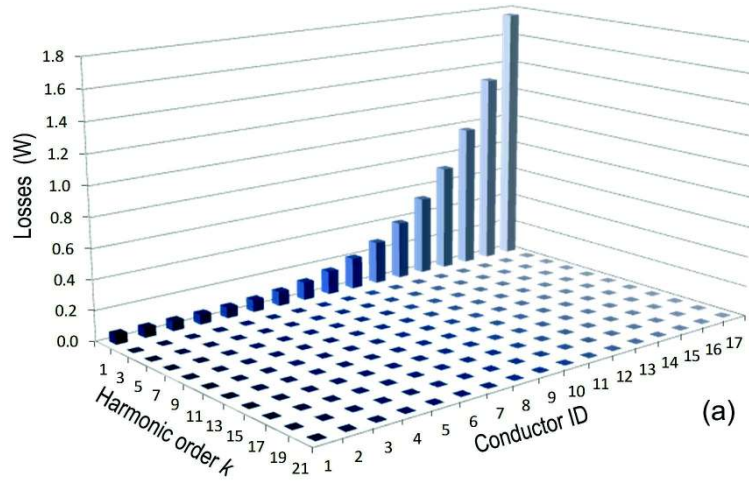
152

Figure 9.13: Summary of THFEA simulation results: (a) losses produced in each conductor for harmonic orders k from 1 to 21; (b) the same for harmonic orders k between 3 and 13.

the overall time taken by the entire optimization process. In quantitative terms, Table IV provides some useful data for comparing the computational performance of THFEA and TSFEA approaches.

COMPUTATIONAL PERFORMANCE COMPARISON (TSFEA VS. THFEA)		
	TSFEA	THFEA
Number of simulations per optimization loop	1	3
Space harmonic orders (k) considered	-	1, 3, 5
Number of current points in the model	-	200 x 10
Time taken by each simulation [s]	2700	43
Total simulation time per optimization loop [s]	2700	129

Table 9.4: Computational performance comparison (TSFEA vs. THFEA)

9.4.3 Use of THFEA simulation results

The copper eddy-current losses estimated as described above are used to compute machine efficiency and to predict the stator thermal behavior. In many cases, their importance from an efficiency viewpoint is small because they constitute a small percentage of the total generator losses (as in the cases illustrated in Section 9.5). Their impact is usually stronger on determining the winding temperature rise in the various regions of the slot as clearly explained in [5]. In fact, eddy current losses, even if small, concentrate in the turns closest to the air-gap, whose temperature rise may thereby grow above insulation thermal class limits. For this reason, the results of eddy-current loss computation at each optimization step are used as the inputs for a thermal calculation intended to predict the temperature field in the stator slot region (fig.9.12).

9.5 Method assessment by comparison with TSFEA

As discussed in Section 9.2, the presented method is set forth as a numerically efficient alternative to TSFEA for the particular purpose of computing SPM rotor motion effects in terms of stator copper eddy-current losses at steady-state. The question however arises as to how reliable and accurate the results it gives are. To assess the accuracy of method, a comparison will be made with the results independently obtained by TSFEA. About the correctness of assuming TSFEA as a reference, it can be observed that many authors give the reliability of this method as granted in eddy current computation, although in absence of experimental evidences [5], [6], [18]. This is partly due to the intrinsic difficulty of measuring eddy currents and

their relevant power losses. However, testing activities have been also reported proving the reliability of TSFEA in predicting copper eddy current in the various parts of electric machines [19].

9.5.1   Calculations at no load on designs A and B

To assess the proposed method, THFEA and TSHEA simulations are run on the couple of generator designs referred to as **A** and **B**"in Section 9.2 (fig.9.3, Tables 9.2-9.3) and the results are compared. The two designs selected are non-optimal configurations which exhibit significant differences with respect to their geometry and rated frequency. Calculations are made supposing that the generator is spinning at different speeds (1, 3 and $5rpm$) in no-load conditions, so that only the eddy current losses being estimated occur in the stator winding. The stator copper losses found with the two
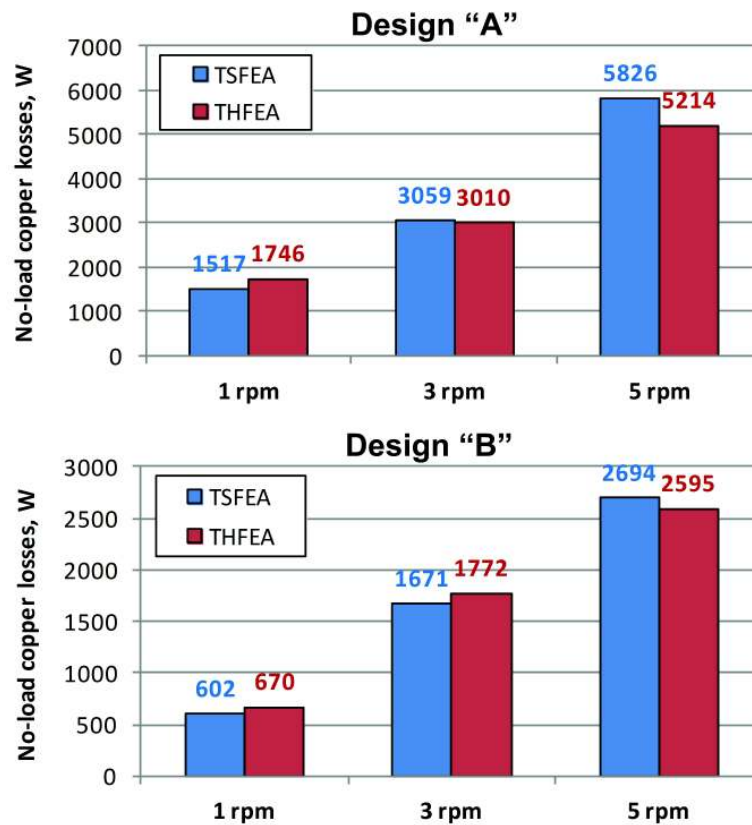

Figure 9.14: No-load ,copper losses computed by TSFEA and THFEA for generator designs A and B at different rotor speeds.

approaches are shown in fig.9.14, which highlights a satisfactory accordance. Furthermore, fig.9.14 together with Table 9.3 indicates that the computed

155

eddy-current losses at rated speed ($3rpm$) are small (less than 5%) compared to the joule losses caused by the fundamental current.

9.5.2 Calculation at no load on other design configurations

In addition to designs **A** and **B**, other machine configurations generated in the optimization process are considered for comparing no-load copper loss values independently computed by TSFEA and THFEA.
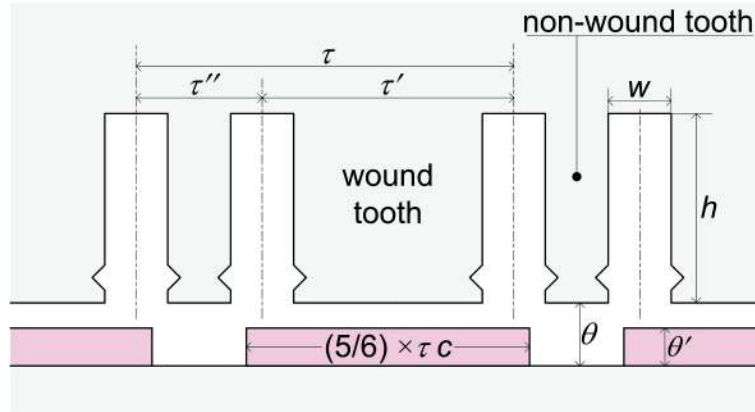

Figure 9.15: . Dimensions used to characterize different generator designs.

To identify the designs explored, the dimensions shown in fig.9.15 are defined, where c indicates permanent magnet coverage [permanent magnet span is easily found to equal $(5/6)\tau c$ because of the 10-pole 12-slot sector design]. In all the explored configurations, c is kept equal to 0.72, while the other dimensions change. Among the possible non-dimensional quantities capable of characterizing machine geometry, the four ratios h/w, τ/τ', θ/θ', w/θ are selected as the most significant. In the diagram of fig.9.16, each bubble defines a design in terms of the selected non-dimensional ratios. The bubble size is proportional to the error of eddy-current losses computed by THFEA with respect to the same losses computed by TSFEA. In all cases, the generator is supposed to be operating at no load at rated speed ($3rpm$). The bubble diagram representation used in fig.9.16 is effective as it can indicate possible correlations between the calculation error and some particular geometrical features of the design. Because the error magnitudes appear to be quite randomly distributed along coordinates h/w, τ/τ', θ/θ', w/θ there does not seem to exist a relationship between the design geometry and the accuracy of the THFEA method proposed. Moreover, fig.9.16 highlights that for all the seven designs taken into account an error less than 6% is found between THFEA and TSFEA computation results.
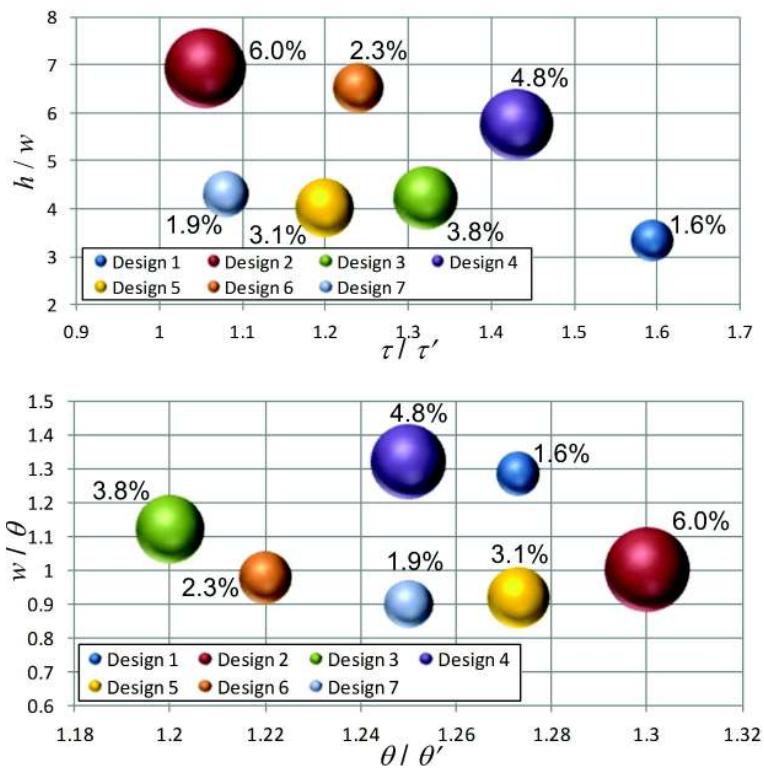
Figure 9.16: Percent error of eddy current losses computed by THFEA compared to TSFEA for different seven generator designs.

9.5.3 Effect of the load

When the machine is loaded, the copper eddy current losses due to the rotor motion cumulate with the conventional joule losses caused by the stator current. Under the hypothesis of unsaturated core, the superposition principle holds [15] assuring that in each stator conductor point the total current density $\mathbf{j}_{tot}$ equals the sum of the current density $\mathbf{j}_{load}$ due to the load and of the current density $\mathbf{j}_{eddy}$ due to rotor motion effects at no load:

$$\mathbf{j}_{tot} = \mathbf{j}_{load} + \mathbf{j}_{eddy} \tag{9.21}$$

Conversely, the superposition principle for power losses cannot be applied. In fact, $\mathbf{j}_{eddy}$ is caused by the sum of equivalent magnetization waves given by (9.2), where it has been demonstrated (Section 9.4) that the term with $k = 1$ is strongly predominant. For $k = 1$, the magnetization wave (2) has the same number of poles and revolves at the same angular speed as the rotor, so the eddy current density $\mathbf{j}_{eddy}$ has a predominant harmonic with the same stator pulsation ω as the load current density $\mathbf{j}_{load}$ (this fact is confirmed by TSFEA simulations). Because $\mathbf{j}_{eddy}$ and $\mathbf{j}_{load}$ have equal frequencies (as far as the main harmonics are concerned), the following inequality holds:

$$\rho|\mathbf{j}_{tot}|^2 = \rho|\mathbf{j}_{load}|^2 + \rho|\mathbf{j}_{eddy}|^2 \tag{9.22}$$

where ρ is the stator copper resistivity and the equal sign applies only on condition that $\mathbf{j}_{eddy}$ and $\mathbf{j}_{load}$ are in phase.
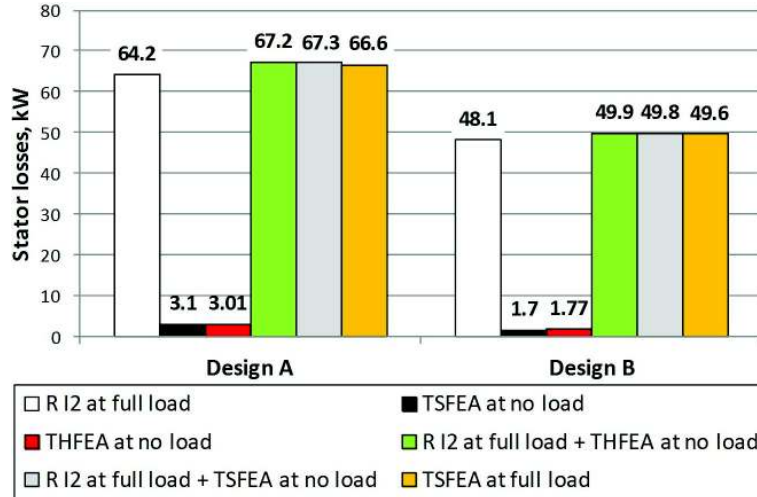

Figure 9.17: Conventional joule (RI2) losses and eddy current losses computed for generator designs A and B at no load and full load conditions.

According to (9.22), the copper losses due to both load and eddy currents acting together is less than the two current fields acting separately. In other words, if we compute total copper losses in load conditions by summing conventional RI^2 losses and the eddy-current losses caused by rotor motion at no load, we obtain a conservative result (i.e. a power loss underestimation). To check the aforementioned statement, a TSFEA simulation of the machine operating at rated speed and rated load is run and the total losses in such conditions are computed. The result is then compared to the sum of the RI^2 conventional losses and the eddy current losses at no load. The comparison is shown in fig.9.17. This indicates that the full load losses computed by TSFEA is actually slightly lower than the sum of joule losses plus no-load eddy-current losses. The latter sum, however, appears to be a good (and in any case a conservative) approximation in those cases where the TSFEA computation is not available or inconvenient to apply.

9.6   Conclusions

One of the issues to be considered in the design of high-power SPM machines featuring rectangular cross-section conductors in open stator slots is the computation of the eddy-current losses which originate in the armature winding as an effect of rotor motion. The use of TSFEA to study such losses suffers from some drawbacks, like the long computation times and the quite complicated post-processing tasks needed for result extraction. These limitations are particularly critical when the aforementioned losses are to be automatically computed at any step of a machine design optimization process. The chapter has presented an alternative approach to face the problem. The approach consists of running some THFEA simulations on a suitably modified machine model where permanent magnets are replaced by a grid of fictitious conductors carrying sinusoidal currents. The set of simulations to be run are defined so that, through the superposition principle, they can accurately reconstruct SPM rotor motion effects. As an application example, the proposed method is used in the genetic design optimization of a fractional-slot SPM generator. In this case it has been shown how few THFEA simulations are sufficient to compute rotor-induced copper losses, with considerable benefits in terms of computational burden. The accuracy of the proposed approach has been assessed by comparison against TSFEA simulations on different generator design configurations and for different operating conditions. The matching between the results obtained in the two ways has proved satisfactory in all cases.

9.7 Appendix

In this Appendix the notation used in (9.3) is clarified. In general terms, let us consider a quantity $a(t)$ varying as a sinusoidal function of time with pulsation ω:

$$a(t) = A\cos(\omega t + \phi) \tag{9.23}$$

Using complex numbers, (9.23) can be written as:

$$a(t) = Re\left\{Ae^{i(\omega t + \phi)}\right\} = Re\left\{Ae^{i(\omega t)}e^{i\phi}\right\} \tag{9.24}$$

where i is the imaginary unit and e is Neper's number. The quantity is naturally associated to a rotating vector of constant amplitude A and revolving at $\omega\ rad/s$, which can be represented by the complex function:

$$\overline{a}(t) = \left(Ae^{i\phi}\right)e^{i\omega t} = \overline{A}e^{i\omega t} \tag{9.25}$$

where $\overline{A} = Ae^{i\phi}$ is defined as the complex phasor associated with the sinusoidal function (9.23).

9.8 References

[1] Y.D. Fan, X.S. Wen, H.M. Wang, J.H. Seo, "Research on stator temperature field of a hydro-generator with skin effect", *IET Electric Power Applications*, vol. 5, no. 4, pp. 371-376, April 2011.

[2] G. Dajaku; D. Gerling, "Stator slotting effect on the magnetic field distribution of salient pole synchronous permanent-magnet machines", *IEEE Transactions on Magnetics*, vol. 46, no. 9, pp.3676-3683, Sept. 2010.

[3] G. Sulligoi, A. Tessarolo, V. Benucci, A. Millerani, M. Baret, F. Luise, "Design, Implementation and testing of a ship-board medium-voltage DC generation system based on a ultra-high speed 12-phase alternator", *IEEE Industry Applications Magazine*, accepted paper.

[4] A. Tessarolo, "Number of stator phases and winding construction technology in high-power AC electric machinery", *IEEE Industry Applications Magazine*, accepted paper.

[5] J. Islam, H.V. H. V. Khang, A.K. Repo, A. Arkkio, "Eddy-current loss and temperature rise in the form-wound stator winding of an inverter-fed cage induction motor", *IEEE Transactions on Magnetics*, vol. 46, no. 8, pp. 3413-3416, 2010.

[6] M.J. Islam, A. Arkkio, "Time-stepping finite-element analysis of eddy currents in the form-wound stator winding of a cage induction motor supplied from a sinusoidal voltage source", I*ET Electric Power Applications*, vol. 2, no. 4, pp. 256-265, July 2008.

[7] G.F. Uler, O.A. Mohammed; Koh Chang-Seop, "Design optimization of electrical machines using genetic algorithms", *IEEE Transactions on Magnetics*, vol. 31, no. 3, pp.2008-2011, May 1995.

[8] M.J. Islam; J. Pippuri; J. Perho; A. Arkkio; , "Time-harmonic finite-element analysis of eddy currents in the form-wound stator winding of a cage induction motor," *Electric Power Applications, IET* , vol.1, no.5, pp.839-846, Sept. 2007.

[9] R. Sabzehgar; M. Moallem, "A review of ocean wave energy conversion systems", *2009 IEEE Electrical Power & Energy Conference (EPEC)*, 22-23 Oct. 2009.

[10] N. Bianchi, M. Dai Pre, "Use of the star of slots in designing fractional-slot single-layer synchronous motors", *IEE Proceedings - Electric Power Applications*, vol. 153, no. 3, pp. 459- 466, May 2006.

[11] A.M. EL-Refaie, "Fractional-slot concentrated-windings synchronous permanent magnet machines: opportunities and challenges", *IEEE Transactions on Industrial Electronics*, vol. 57, no. 1, pp. 107-121, Jan. 2010.